PLASMONIC SILVER NANOPARTICLES FOR AN IMPROVED VOPcPhO:P3HT ORGANIC SOLAR CELLS

KHAIRUS SYIFA BINTI HAMDAN

**FACULTY OF SCIENCE
UNIVERSITY OF MALAYA
KUALA LUMPUR**

2017

PLASMONIC SILVER NANOPARTICLES FOR AN IMPROVED VOPcPhO:P3HT ORGANIC SOLAR CELLS

KHAIRUS SYIFA BINTI HAMDAN

THESIS SUBMITTED IN FULFILMENT OF THE REQUIREMENTS FOR THE DEGREE OF DOCTOR OF PHILOSOPHY

FACULTY OF SCIENCE
UNIVERSITY OF MALAYA
KUALA LUMPUR

2017

UNIVERSITY OF MALAYA
ORIGINAL LITERARY WORK DECLARATION

Name of Candidate: KHAIRUS SYIFA BINTI HAMDAN

Matric No: SHC 130060

Name of Degree: Doctor of Philosophy

Title of Thesis ("this Work"):

PLASMONIC SILVER NANOPARTICLES FOR AN IMPROVED VOPcPhO:P3HT

ORGANIC SOLAR CELLS

Field of Study: Experimental Physics

I do solemnly and sincerely declare that:

(1) I am the sole author/writer of this Work;
(2) This Work is original;
(3) Any use of any work in which copyright exists was done by way of fair dealing and for permitted purposes and any excerpt or extract from, or reference to or reproduction of any copyright work has been disclosed expressly and sufficiently and the title of the Work and its authorship have been acknowledged in this Work;
(4) I do not have any actual knowledge nor do I ought reasonably to know that the making of this work constitutes an infringement of any copyright work;
(5) I hereby assign all and every rights in the copyright to this Work to the University of Malaya ("UM"), who henceforth shall be owner of the copyright in this Work and that any reproduction or use in any form or by any means whatsoever is prohibited without the written consent of UM having been first had and obtained;
(6) I am fully aware that if in the course of making this Work I have infringed any copyright whether intentionally or otherwise, I may be subject to legal action or any other action as may be determined by UM.

Candidate's Signature   Date:

Subscribed and solemnly declared before,

Witness's Signature   Date:

Name:

Designation:

ABSTRACT

The use of plasmon-embedded metal nanostructures enables light concentration and trapping in organic solar cells. In this work, the study was focused on the effects of surface plasmon, which incorporate organic solar cells device based on VOPcPhO:P3HT material. Several plasmonic structures have been constructed experimentally to understand the effect of optical behaviour on spherical silver particles and silver nanowires, which has been explored using finite-difference time-domain (FDTD) software. Integrating those shapes in bare silicon substrate shows enhancement in the light absorption of solar cells. The shape of metal nanostructure has been constructed experimentally like dendritic and flower-like silver structures. Three methods of fabrications have been applied to ameliorate the homogeneously silver particles in the thin film of solar cells, including electrophoretic deposition (EPD), spin coating technique, and electron beam (e-beam) evaporation technique. Field emission scanning electron microscopy (FESEM) characterization has clearly shown the specific technique that gave the best morphology. The annealing condition also has been varied for the well-formed silver nanoparticles, which was prepared by e-beam evaporation technique. The ultra-violet/visible/near-infrared (UV/VIS/NIR) spectroscopy showed that silver nanoparticles prepared by e-beam evaporation technique annealed at 250 °C has the most intense and prominent surface plasmon behaviour. Hence, the silver particles prepared at this optimum condition has been chosen to be integrated in organic solar cells device of VOPcPhO:P3HT blend system. The integrated device shows a very significant increase in efficiency and stability. The calculated efficiency from the current-voltage (I-V) measurement showed an increment from 1.09% of pristine device to 1.89% of the device with silver nanoparticles, which is the best increment of efficiency of VOPcPhO:P3HT blend organic solar cells device reported to date.

ABSTRAK

Kegunaan struktur logam nano berplasmon adalah untuk membolehkan cahaya ditumpu dan diperangkap dalam sebuah peranti sel solar organik. Dalam kerja ini, tumpuan diberi kepada struktur plasmon permukaan yang digunakan dalam peranti sel solar organik yang berasakan bahan VOPcPhO:P3HT. Bagi mengkaji kesan struktur ini terhadap peranti organik tersebut, beberapa struktur plasmonik telah dihasilkan secara ekperimentasi untuk memahami kesan ciri-ciri optik terhadap struktur sfera argentum dengan menggunakan struktur wayar nano argentum perisian FDTD. Pengintegrasian bentuk-bentuk tersebut dalam substrat silikon telah menunjukkan peningkatan kadar penyerapan cahaya dalam peranti sel solar silikon. Bentuk logam struktur nano yang lain juga telah dihasilkan secara ekperimentasi seperti struktur dendrit argentum dan struktur seperti bunga. Tiga kaedah penghasilan telah digunakan untuk membaiki kesamarataan taburan zarah argentum dalam sel solar nipis, termasuk pengenapan electrophoretic (EPD), teknik salutan putaran, teknik penyejatan hentaman elektron (e-beam). Pencirian mikroskop perlepasan elektron kawasan (FESEM) telah jelas menunjukkan teknik yang telah dapat menghasilkan morfologi terbaik. Keadaan penyepuhlindapan juga telah diubah bagi struktur nano argentum yang telah dihasilkan dengan baik. Ultra-ungu/tampak/hampir inframerah (UV/Vis/NIR) spektroskopi menunjukkan bahawa zarah nano argentum disediakan oleh teknik penyejatan e-beam dan dipanaskan pada suhu 250 ° C mempunyai sifat plasmon permukaan yang paling ketara. Keadaan zarah argentum telah pilih dalam mengintegrasikan dalam peranti sel solar organik VOPcPhO:P3HT. Peranti bersepadu menunjukkan peningkatan yang sangat ketara dalam kecekapan dan kestabilan. Kecekapan dikira dari pengukuran arus-voltan (I-V) menunjukkan kenaikan daripada 1.09% oleh peranti asal kepada 1.89% daripada peranti dengan zarah nano argentum yang merupakan kenaikan yang terbaik bagi kecekapan peranti sel VOPcPhO: P3HT yang dilaporkan setakat ini.

TABLE OF CONTENTS

LIST OF FIGURES

LIST OF TABLES

LIST OF SYMBOLS AND ABBREVIATIONS

Ag   : Silver

AgNPs   : Silver Nanoparticles

AgNDs   : Silver Nano-dendrites

Al   : Aluminium

AAO   : Anodisc Aluminium Oxide

OSCs   : Organic Solar Cells

ITO   : Indium-Tin-Oxide

HOMO   : Higher occupied molecular orbitals

LUMO   : Lower unoccupied molecular orbitals

SMU   : Source measure unit

I   : Current

I_{sc} : Short circuit current

J_{sc} : Short circuit current density

V_{oc} : Open circuit voltage

FF   : Fill Factor

V   : Voltage

I-V   : Current-Voltage

J-V   : Current density-voltage

FESEM   : Field emission electron scanning microscopy

UV/VIS   : Ultraviolet/Visible

NIR   : Near Infrared

PL   : Photoluminescence

PCE   : Power conversion efficiency

SCLC	:	Space Charge Limited Current
FDTD	:	Finite Domain Time Difference
PML	:	Perfectly matched layer
DUVL	:	Deep Ultra Violet Lithography
NIL	:	Nano Imprint Lithography
SCIL	:	Substrate Conformal Imprint Lithography
LIL	:	Laser Interference Lithography
EM	:	Electromagnetic
OLED	:	Organic Light Emitting Diode
P_{max}	:	Maximum Power
Ω	:	Ohm
E	:	Dielectric constant
λ	:	Wavelength
N	:	Frequency
h	:	Planck's constant
H	:	Power conversion efficiency
μ	:	Charge carrier mobility
V	:	Volume
r	:	Radius
J	:	Mobility
d	:	Thickness
SP	:	Surface Plasmons
EDX	:	Energy dispersive X-ray
NaOH	:	Sodium Hydroxide
$Ag(NH_3)$	:	Silver Nitrate

CHAPTER 1: INTRODUCTION

1.1   Introduction to Plasmonics

Plasmonics is currently a growing research field. It focuses on the control and manipulation of light waves at the subwavelength scale using metallic structures. Plasmonics allows optical signals to be confined into deep subwavelength scale, which helps to bridge length scale mismatch between typical optical systems and on-chips electronics. At optical frequencies, the free electrons in noble metals can sustain volume and surface charge density oscillations, called plasmons. Plasmons can take different forms, ranging from surface plasmon polaritons propagating along the metal dielectric boundaries to localised plasmons with electrons oscillating inside metal nanoparticles, depending on the geometry of metal structures and their surrounding environment (Freise, 2012).

As the plasmonics properties vary, depending on the geometry of metallic structure (Kalfagiannis et al., 2012), many promising results in plasmonic research have revealed its great potential for various applications such as subwavelength microscopy, light emission and detection, photovoltaic harvesting, biochemical sensing, optical signal processing, and many more (Kim et al., 2015). Therefore, synthesis of metal nanoparticles is an important area in nanoscience and nanotechnology due to its variety and wide ranges of potential applications from electronic to biologic fields. The numerous preparation routes of NPs can be grouped into two main different strategies. First is the "top-down" method (Physical methods); from large to small dimensions, and secondly is the "bottom-up" method (wet chemical methods); from molecular scale to nanoscale (Figure 1.1).
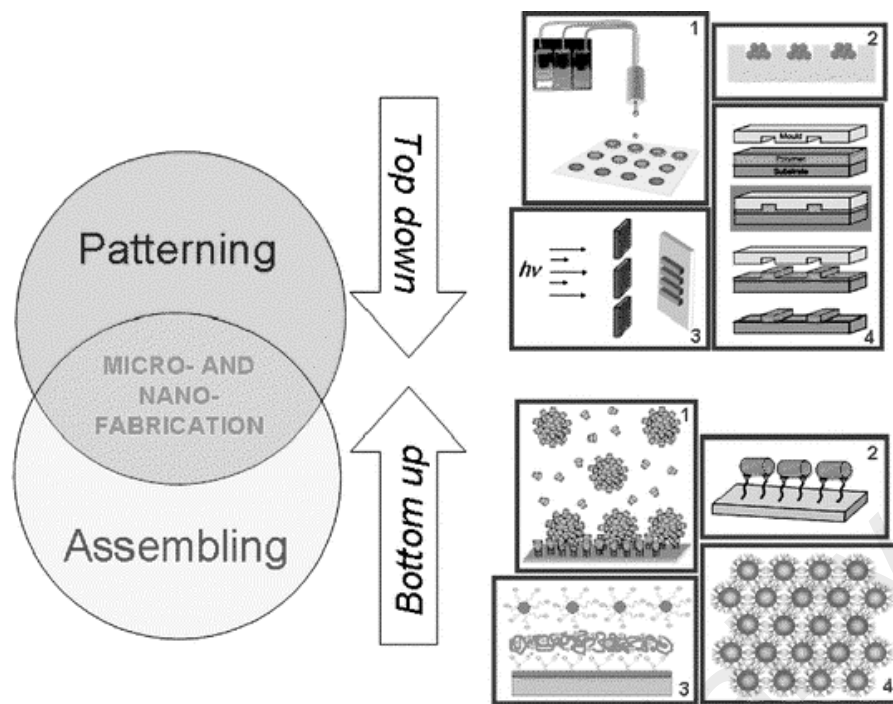
Figure 1.1 Top-down and bottom-up approach of micro and nano fabrication

In an example of "bottom-up" method, as reported by Ashok Kumar Das et al., they had grown the flower-like nanocrystals using the seed-mediated approach by using electrochemically deposited Au nanoseeds for electroanalytical applications (Das & Raj, 2010). The "top-down" approach of preparing a core shell and half shell nanowire by using electron beam lithography has been theoretically proposed by Shahriar et al.(Sabuktagin et al., 2014)

1.2 Introduction to Organic Photovoltaic

Organic photovoltaic has received an increased research interest especially among the industrial sectors. The technology, which produces electricity from sunlight source by employing organic thin films semiconductor, is a promising technology for the future. Among the advantages of this organic photovoltaic is that the device can be easily processed at low temperature and can be fabricated on various types of substrate. Thus, it has the potential to spawn solar-powered products, flexible form factors, and a

new generation of low-cost organic photovoltaic to the silicon technology (Kalowekamo & Baker, 2009; Kippelen & Bredas, 2009). However, the main disadvantage such as short life time is due to instability when in contact with oxygen (Dalal et al., 2012; Jørgensen et al., 2008) or exposed to high humidity, which highly affects their efficiency. Thus, it is crucial to find a solution to improve their efficiency (Notarianni et al., 2014).

Lots of efforts in achieving higher efficiencies are focusing on optimizing the morphology of the active photovoltaic layer and charge transport properties of the absorber. This was done via thermal annealing treatment, use of various solvent, the use of additives, and the process conditions. The power conversion efficiency (PCE) in inorganic solar cells is controlled by the absorption of light and the collection of charges at the electrodes. Increasing the light absorption is crucial to increase the PCE of these devices. Due to the low carrier mobility of the conducting polymer and short lifetime of the excitons, the optimum thickness of the active layer is often limited to about 100nm or less (Kippelen & Bredas, 2009). For larger thickness, the recombination of free charge carriers becomes predominant with a consequent decrease of PCE. Lowering the layer's thickness limits the absorption of all the photons with a consequent of low photocurrent. For all these reasons, increasing the light optical path length in the device becomes very crucial to increase the PCE. In fact, increasing the light by guiding the light multiple times in the active layer of the organic solar cells can increase the absorption probability in the device (Mokkapati & Catchpole, 2012). The light trapping can be achieved with structures that are similar or smaller in size to the wavelength of the light of interest and with specific materials that interact strongly with the light such as semiconductors or metals (Catchpole & Polman, 2008; Kalfagiannis et al., 2012).

Recently, the usage of the metallic nanoparticles in organic photovoltaics has been widely exploited as they can be easily incorporated without compromising the original structure of the device. Generally, a collective oscillation of electrons in metallic nanoparticles are generated by the light at a specific frequency leading to a strong absorption or scattering of the light as function of particle size (Catchpole et al., 2011). The inclusion of metallic nanoparticles can enhance the photo absorption and consequently increase the forward scattering cross section and the near field enhancement without increasing the thickness of the active organic photovoltaic layer (Notarianni et al., 2014). Metallic nanoparticles have already been used to enhance the photocurrent by 33% of thin film silicon solar cells (Pillai et al., 2007).

1.3 Motivation

As mentioned in the previous section, the line shape SPR can be widely tailored as it strongly depends on size, distribution, and shape of nanoparticles, dielectric of materials nanoparticles, as well as the dielectric of surrounding environment (Murray & Barnes, 2007). This sensitivity has led to numerous applications and can be tuned following the individual's need. Thus, raise the urge to study the tunability of plasmonic nanoparticles and motivations to apply this interesting field in organic photovoltaic layer, which have encouraging advantages.

Scoping the scientific research for the purpose of sustaining the future, the technology towards harvesting solar energy must be low cost, and scalable productions must have a low environmental impact. Thus, organic solar cells have the potential to become that promising technology of harvesting light (Hoppe & Sariciftci, 2004; Rand & Richter, 2014). However, this device have disadvantages of low efficiency and instability when exposed to light (Dalal et al., 2012; Jørgensen et al., 2008). Researchers in this field put efforts to achieve higher efficiency and stability of organic solar cells to

compete with the technologies present in the market. It is persuasive to implement the admiring research field such as plasmonic to the ongoing research of improving organic photovoltaic efficiency.

Apart from optimizing the morphology of the photovoltaic active layer and the charge transport properties of the absorber through thermal annealing treatment, use of various solvent, the use of additives, and the process conditions; introduction of metallic nanoparticles inside the cells to trap and confine light could be a great alternative to increase the performance of the device.

1.4   Research Objectives

In conjunction with the motivation mentioned previously, the objectives of this research are as follows;

i.   To fabricate and study the structure and optical response of silver nanoparticles with different shape, size, and particle distribution and study their optical responses.

ii.   To study the enhancement of light absorption in organic active layer film with the introduction of metallic nanoparticles.

iii.   To fabricate the organic solar cells device of the blend system (VOPcPhO:P3HT) and study its efficiency enhancement when integrated with suitable structure of nanoparticles.

1.5   Thesis Framework

This thesis covers seven chapters starting with Chapter 1 that briefly introduces the general background of the research study, motivation, and objectives.

Chapter 2 provides the theory and literature review to provide an overview of the recent developments in the field of plasmonics, as well as a brief introduction of organics solar cells and the measurement.

Chapter 3 presents the techniques of fabricating metal nanoparticles characterization to study the deposited samples. The chapter also introduces photoactive materials and outlines the experimental fabrication techniques and the optical and electrical characterization procedures, utilized in the present research work.

Chapter 4 reports on the FDTD simulation used to construct a half shell and core shell silver nanowires incorporated in silicon cell and their optical response. This chapter also presents the overview introduction of optical response of spherical silver nanoparticles with different sizes.

Chapter 5 discusses the diverse plasmonics structure. All fabricated structures were compared then chosen for integrating in organic solar cells.

Chapter 6 demonstrates the electrical characterization VOPcPhO: P3HT blend organic solar cells fabricated in optimized condition. The organic solar cells device was compared with the one that has been integrated with Ag NPs in terms of their efficiency and stability.

Finally, the research work reported in this dissertation is summarized in Chapter 7. An outlook on future research directions in this field was also suggested in the second section of this chapter.

CHAPTER 2: THEORY AND LITERATURE

This chapter enlightens the theory and literature review related to the plasmonic field and the application of organic solar cells. The chapter presents the route history of the plasmonics field in terms of theoretical consideration that arose in the past along with a brief review of the physics underlying the plasmonic works in a solar cells system. A brief overview of basic modes/principles for organic solar cells is explained.

2.1   Plasmonics as a Discipline

Plasmonics is the most intense topic in the exciting field of nanophotonics. It studies how electromagnetic fields can be confined over dimensions on the order of or smaller than the light wavelength (Atwater & Polman, 2010; Maier, 2007). The basic study of plasmonics is on the interaction process of the electromagnetic radiation with the conduction electrons in the metallic boundaries that range from corrugated surfaces to structures in nanometre. Consequently, the plasmons confined in nanoparticles lead to an enhanced optical near-field of sub-wavelength dimensions. Therefore, scientists are urged in trying to utilize this resonant interaction to control light on a sub-wavelength scale to manipulate interactions between light and matter. The concept of plasmonics is a description of the science and technology of metal-based optics.

Plasmonics as a field of science and technology is not older than a decade. Yet, the history has revealed that the two main ingredients of this field, which are *surface plasmon polaritons* and *localized surface plasmons*, have been clearly described in 1900 (Maier, 2007). Despite that, it is important to appreciate the interlinked nature of numerous involved phenomena and applications of this field. Sommerfeld has theoretically studied the electromagnetic surface modes on metal wires and calculated the solution of Maxwell's equations for wave propagation along a cylindrical metal surface (Sommerfeld, 1952). These surface modes are electromagnetically equivalent to

surface plasmons polaritons in the visible domain. In 1908, Gustav Mie established a clear mathematical basis on light scattering on small spherical particles. This formalism was later applied by successors as fundamentals for description of localized surface plasmon resonances in metallic nanoparticles.

Localization of light at nanometre scale can also be achieved by exploiting surface phonon resonances in polar dielectrics, which is considered as the infrared counterpart of surface plasmon resonance. Coupling between phonon and plasmon resonances causing enhanced infrared absorption is said to be useful in near-field microscopy, imaging, and sensing (Mandal & Chaudhuri, 2013).

2.2   Theoretical Considerations on Plasmonics

This section introduces the surface plasmons and their dispersion relation. In the beginning of the explanation, an introduction on the theoretical models such as Mie, Gans, and Drude will be described briefly because of their importance to the field of plasmonics.

2.2.1   Mie Theory

The classical Mie theory suggested by Gustav Mie in 1908 is relatively simple and versatile. The theory describes the mechanism of light absorption by small metal particles is by solving Maxwell's equations. The theory is based on the assumptions that a charge separation is successively induced on the particle's surface when the electromagnetic field interacts with that particle. This charge separation will lead to an occurring restoring force. It has been shown that such absorption of light in the ultraviolet-visible region by metallic particles differs with a variety of geometrical as well as environmental factors.

Solving Maxwell's equations result in a relationship for the extinction cross-section

for metallic nanoparticles

$$\sigma_{ext} = \sigma_{sca} + \sigma_{abs} \tag{2.1}$$

Where σ_{ext}, σ_{sca} and σ_{abs} are the extinction, scattering, and absorption cross-section, respectively.

Generally, both absorption and scattering process occur simultaneously, however, there are situations where either one of the two occurrence dominates. Taking into account small particles in comparison to the wavelengths of the light (particle radius a $\ll \lambda$) only absorption is significant. Using a complex expression for the dielectric constant:

$$\varepsilon(\omega) = \varepsilon'(\omega) + i\varepsilon''(\omega) \tag{2.2}$$

where ε' and ε'' are the real and imaginary part of the dielectric function of the metallic nanoparticles, respectively, while ω is the angular frequency of the exciting radiation according to the Drude model (Jones, 1957). Based on the assumptions that the particles are spherical, small, and embedded in an isotropic and non-absorbing medium with a dielectric constant $\varepsilon_m = n_m{}^2$, Mie solved the extinction cross section of such solution where its real part is given by eq. (2.3):

$$\varepsilon(\omega) = 9\frac{\omega}{c}\varepsilon_m{}^{\frac{3}{2}}V_o \frac{\varepsilon''(\omega)}{[\varepsilon'(m)+2\varepsilon_m]^2 + \varepsilon''(m)^2} \tag{2.3}$$

where $V_o = (4/3)a^3$ is the volume for spherical nanoparticle, c is the vacuum velocity of light, and ε_m is the dielectric constant of the host medium. That equation determines the line shape of the absorption band of the particles. The bandwidth and the peak height are well approximated by ε''(ω). The position of the maximum absorption occurs when $\varepsilon'(\omega) \approx -2\varepsilon_m$, if $\varepsilon''(\omega)$ is small or if it is only a weakly dependent on ω. Other than that,

9

as can be observed from the equation, size dependence of the peak position is unpredicted. Nevertheless, experimental results shows opposite to the theory where size dependence is observed (Kreibig & Genzel, 1985; Kreibig & Volmer, 1995; Link & El-Sayed, 1999; Mulvaney, 1996). Again from equation (2.3), two limiting cases can be deduced for which σ_{ext} is equal to zero. As for the first case, the complex part for the dielectric constant is zero ($\varepsilon'(\omega) = 0$), i.e., the particle is non-absorbing (this applies to dielectric materials, i.e., quartz or sapphire, which do not absorb in visible range, that is why they are used as substrates for transmission measurements). While in the second case, ($\varepsilon''(\omega) \to \infty$), the material reflects all of incoming radiation at this wavelength, i.e., the complex part of the dielectric function for metals has a large value in the visible making them very shiny and totally reflecting for the incoming light. Since the shape of nanoparticles is not limited to spherical, Mie's model had to be extended for other metallic structures.

2.2.2 Gans Theory

In 1912, Richard Gans offered a modification of the Mie theory, which he extended the expression for the extinction cross-section of spheres to ellipsoidal particles (Hostetler et al., 1998). With this modified expression, calculation for the absorption resonance of rod-like nanoparticles can be achieved.

Because of the ellipsoidal shape, two fundamental oscillation directions for the conduction electrons must be put into consideration. First is along the short axis of the ellipsoid, and the second one is along the long axis. Both oscillations induce a charge separation and thus a localized plasmon resonance in the nanoparticle. The extinction cross-section proposed by Gans considered an ellipsoid dimensions that fulfil the condition: a > (b = c) as shown in Figure 2.1 below.
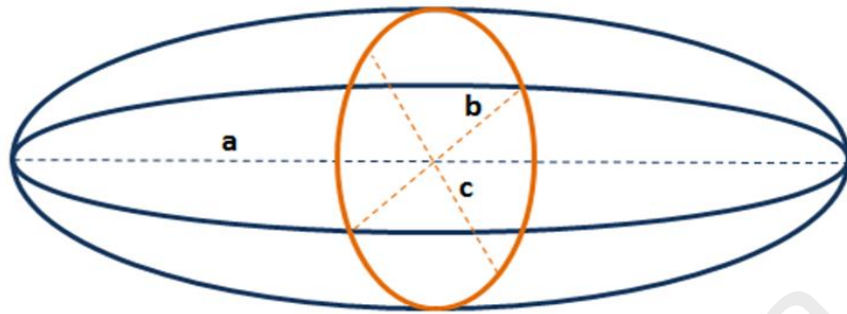
Figure 2.1 Schematic of an ellipsoidal particle with dimensions: a > b = c, where a, is the dimension of the longitudinal axis, b and c are the dimensions of the transverse axes.

These modifications for ellipsoidal nanoparticles give rise to two possible plasmon modes (longitudinal and transverse). The longitudinal mode is strongly dependant on the aspect ratio. For the case of many metals, the absorption region that is up to the bulk plasma frequency, ω_p, is dominated by the free electron behaviour. Thus, the dielectric response is well described by the simple Drude model, as introduced in the following section.

2.2.3 Drude Model

In 1900, a new and bold theory of electrical and thermal conduction of metals was introduced by a German physicist named Paul Drude. The theory applied the highly successful kinetic theory of gases to metal, considered as a gas of electrons (Drude, 1900a, 1900b). Drude's model has come to an assumption that the conduction of electrons in the metal can be treated like molecules:
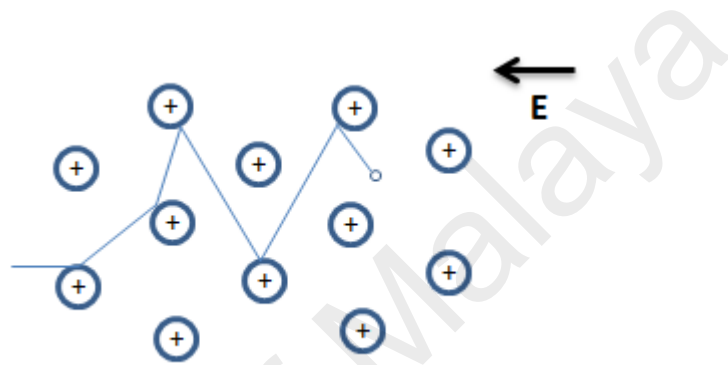
Figure 2.2 Drude's model of electrons constantly collide between heavier and stationary ions

According to this free electron model, the dielectric function of such free electron gas can be denoted as:

$$\varepsilon(\omega) = 1 - \frac{ne^2}{\varepsilon_o m \omega^2} \tag{2.4}$$

Where n is the electron density, ε_o is the vacuum permittivity, e and m are electron charges and mass respectively.

In a medium with an equal concentration of positive and negative charges, the bulk plasma frequency can be represented as:

$$\omega_p{}^2 = \frac{ne^2}{\varepsilon_o m} \tag{2.5}$$

Rewriting equation (2.4) with equation (2.5) results in the dielectric function:

$$\varepsilon(\omega) = 1 - \frac{{\omega_p}^2}{\omega^2} \qquad (2.6)$$

Introducing a constant offset, ε_∞, which adds the effect of interband transitions at frequencies above plasma frequency, which the Drude model does not include, the dielectric function is denoted:

$$\varepsilon(\omega) = \varepsilon_\infty - \frac{{\omega_p}^2}{\omega^2} \qquad (2.7)$$

All these presented models are used to interpret the plasmonic interaction with various nanostructures.

2.2.4 Plasmons

Generally, in metals, plasmon can be defined as the oscillation of free conduction electron density against the fixed positive ionic background. This oscillation is longitudinal and originates from long-range correlations of the electrons caused by Coulomb forces. In order to understand this phenomenon, one can visualize a rectangular metal slab placed in an external electric field, which points to the left (Figure 2.3). Electrons will start to take position to the right side consequently exposing the positive cores (ions) on the left side. The electron movement lasts until the field inside the metal is cancelled. If the given external field is switched off, the electrons will start to repel each other, attracted to the bare left positive ions on the left side. This occurrence will make the electrons oscillate back and forth at the frequency given by equation 2.5.

13
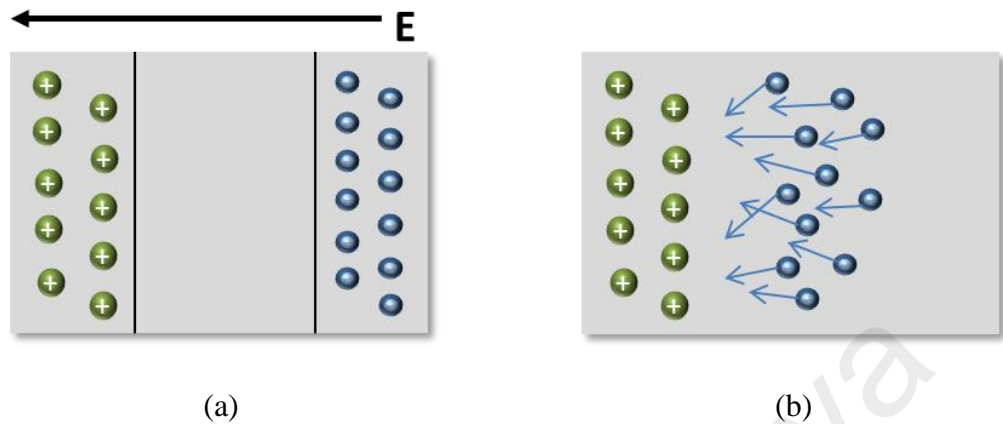
Figure 2.3 Simple schematic of plasma oscillations. Green spheres represent fixed positive background of ions and blue spheres represent the electron gas. **(a)** The charges are separated because of the applied external electric field. **(b)** Situation without external field. The electrons move back to cancel the charge separation.

Such oscillations in gaseous discharges were theoretically and experimentally investigated (Langmuir, 1928). These collective oscillations of plasma inside the metal with a frequency are called volume or bulk plasmons.

For the metallic particles that are similar or smaller in size than the wavelength of the incident light, a strong interaction occurs between the free conduction electrons in the metal and the electromagnetic radiation. Plasmons are the oscillations of these free conductions with the generation of the dipole into the particles when they interact with light. In a particle picture these oscillations are described as plasmons.

Plasmons play a large role in the optical properties of metals. Incoming light of frequency below the plasma frequency is reflected because of the screening of the light electric field by the electrons in the metal. Light of frequency above the plasma frequency is transmitted because the electrons cannot respond fast enough to screen it (Maier, 2007). Some metals, like gold and copper, on the other hand have electronic

interband transitions in the visible range, whereby specific colours are absorbed (Freise, 2012).

2.2.5 Surface Plasmons

The importantly extended study to comprehend the physical phenomenon of plasmons study was the concept of "surface plasmons" (SPs). Those are the result of solving Maxwell's equations giving a surface bound mode at the interface between a metal and a dielectric. Surface plasmons are oscillations of electron that may exist at the interface of two media which fulfils the condition where the real part of the dielectric function of the materials has to change sign across the interface. In this interaction, the free electrons respond collectively by oscillating in the same resonance with the light wave frequency. Note that SPs have a lower energy than bulk plasmons.

The strongly localized excited SPs across the interface are the classically considered EM surface waves that propagate along the interface and decay exponentially with normal distance to the interface. SP waves are tightly bound to metal–dielectric interfaces penetrating around 10 nm into the metal (the so-called skin depth) and typically more than 100 nm into the dielectric (depending on the wavelength) (Maier, 2007; Murray & Barnes, 2007). Hence, EM waves will be concentrated in a region that is considerably smaller than their wavelength. This feature proposes the possibility of using SPs for the fabrication of nanoscale photonic circuits operating at optical frequencies (Freise, 2012; Ozbay, 2006). The existence of surface plasmons was first predicted in 1957 by R.H. Ritchie (Ritchie, 1957). Then, the surface plasmons were widely studied by many scientists in the following two decades (Kretschmann & Raether, 1968; Otto, 1968).

The two main types of SPs in respect to their propagation behaviours along the interface are the extended or propagating SP and localized SP. The propagating SP is

said to be more classical, since it has been known for a longer time. However, the latest advancements in nanotechnology have made the fabrication of structures with nanometre scale features feasible, thus the localized SPR has become a subject of immense interest among researchers in the field. The localized surface plasmon resonance (LSPR) is explained in the following section.

2.2.6   Localize Surface Plasmon Resonance

To recall back, a strong interaction occurs between the free conduction electrons in the metal and the EM radiation. This happens when the metallic particles are very similar or smaller in size than the wavelength of the light of interest. Plasmons are the oscillations of these free conductions electrons with the generation of the dipole into the particles due to the interaction with the light (Figure 2.4). A resonance state occurs when the frequency of the light matches the frequency of the electrons oscillating and is defined as localized surface plasmon resonance (LSPR) in the case of nanometre-sized structures (Murray & Barnes, 2007).
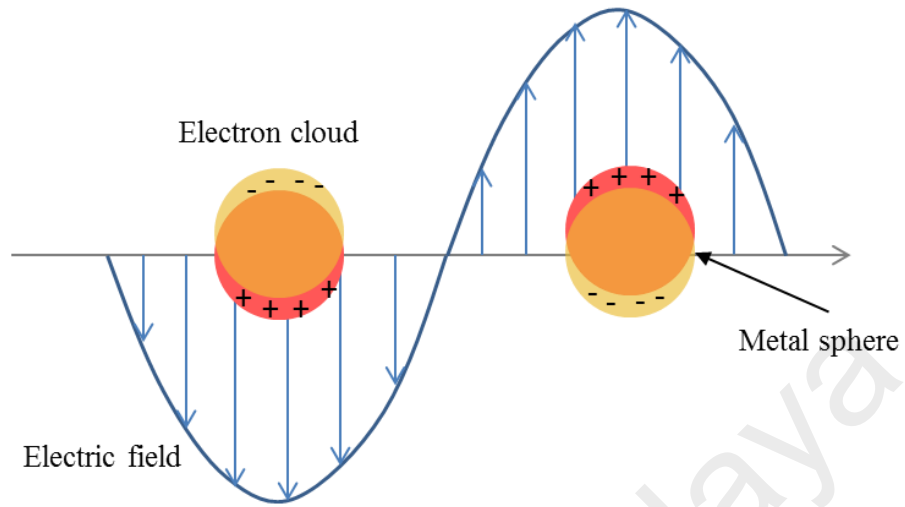
Figure 2.4 Schematic of surface plasmon resonance where the free conduction electrons in the metal nanoparticle are driven into oscillation due to strong coupling with incident light.

The plasmons energy in a free electron model is defined as (Maier, 2007):

$$E_p = \hbar \sqrt{\frac{ne^2}{m\varepsilon_0}} = \hbar\omega_p{}^2 \tag{2.13}$$

where, n is the density of free electrons, e is the elementary charge, m is the electron mass, ε_o is the permittivity of free space, $\hbar$ is the Planck constant, and ω_p is the bulk plasmon frequency.

For metal with low interband absorption, the dielectric function can be described by using the proposed Drude model, which explains the response of damped, free electrons to an applied electromagnetic field with a frequency of ω (Maier, 2007):

$$\varepsilon_r(\omega) = 1 - \frac{\omega_p}{\omega^2 + i\gamma\omega} \tag{2.14}$$

where $\tau = \frac{1}{\gamma}$ is the relaxation time and ω is the angular frequency of an applied electromagnetic field.

There are several factors that influenced the LSPR modes such as particle size, shapes, and particles distribution (Murray & Barnes, 2007). In other words, the LSPR can be supported by a wide variety of structure features. Even the individual particles can have shapes ranging from the simple sphere to ellipsoids, rods, stars, cubes, and many possible shapes. New types of resonance behaviours can be achieved with interacting particle pairs. One can also invert the geometry and consider the LSPR modes of holes or voids instead of particles. Other than that, there are also localized modes associated with particles distribution that have specific inter-particle distance that are able to tune the resonance modes.

There is an increase in the amount of absorption and scattering with the increase of the particle size. Both factors contribute to the optical extinction of a metallic nanoparticle, which scattering takes over from absorption as the dominant contribution to the extinction, when the particle size increases (Bohren & Huffman, 1998; Rukshan et al., 2012). Thus, a change in the position and width of the LSPR is expected. When the size of a sphere particle is increased from 10 nm to 90 nm, the resonance peak will shift from 400 nm to 800 nm (Bohren & Huffman, 1998; Kreibig & Vollmer, 1995). These changes are caused by the way in which the polarization field induced by the surface charges is affected by the amplitude and relative phase of the scattered and incident fields.

Other than particle size, particle shape is one of the important factors that influenced the LPSR modes. The optical studies of an extensive variety of different shaped particles were possibly done, as recently the sophisticated methods for the fabrication of

nanostructure are rapidly developed. As previously mentioned in the introduction, fabrication methods that are typically involved are either growing the particles from a solution or lithographic techniques whereby material is deposited through a patterned mask. The ultimate goal in many studies is to optimize the localization and enhancement of the field associated with the LSPR. Typically this is achieved by designing structures that have an inhomogeneous configuration, such as core-shell particles, or that have sharp geometrical features such as nanoprisms, nanocubes, and star-shaped particles (Das & Raj, 2010; Qadir et al., 2014; Sabuktagin et al., 2014; Sherry et al., 2005).

To further expand the range of available way in tuning the LSPR modes is by allowing an interaction between two or more particles separated by very small distances. Typically the distance is within the decay length of the electromagnetic (EM) field associated with the mode. Hybridization effect can arise from coupling between LSPR modes, and produces the high and low energy modes with differing EM field distributions (Murray & Barnes, 2007). The primary motivation for studying particle pairs is that strong EM field enhancements are expected to exist within the gap between the particles (Kinnan & Chumanov, 2010; Quidant et al., 2007).

2.3   Plasmonics Light Trapping in Organic Solar Cells

As what was realised in thin film silicon solar cell technology where the thickness of the silicon is reduced to only a few micrometers to save cost (Derkacs et al., 2006; Pillai et al., 2007) and to what was done to enhance the performance of dye-sensitized solar cells (Lin et al., 2012; Muduli et al., 2012), light trapping in organic solar cells has become an exciting work to increase the efficiency in organic solar cell devices.

Inclusion of periodic nanostructured, metallic nanoparticles, diffraction gratings, and a combination of gratings and metallic nanoparticles are among the techniques that have

been introduced to the study of light trapping in organic photovoltaics (Kim et al., 2008; Lindquist et al., 2008; Lu et al., 2013; Muduli et al., 2012). The advantage of including metallic nanoparticles into the organic photovoltaic device is it does not modify the basic architecture of the devices. In fact, the metallic nanoparticles can be easily added to one of the organic layers of the device (Notarianni et al., 2014).

Essentially, the addition of metallic nanoparticles can enhance the absorption of the light in a medium by two mechanisms. First is by increasing the forward scattering cross section, and the other is by a near-field enhancement (Atwater & Polman, 2010).

2.3.1   The Scattering Cross Section

When a metallic nanoparticle is embedded in a homogeneous medium, it will scatter the light in both forward and reverse directions (Bohren & Huffman, 1998; Kreibig & Vollmer, 1995). Certainly, when the nanoparticle is placed closed to the interface of two dielectrics, the entering light tend to scatter more into the dielectric with larger permittivity (Mertz, 2000). This way, by the angular spread of the light into the dielectric consequently it will increase the optical path length. When the scattered light hit the metal contact, it will reflect the light back towards the surface where the metallic nanoparticles are present. The reflected light are then scattered again resulting in multiple passes of light through the organic solar cell (Figure 2.5).

For metal nanoparticles with diameters below the wavelength of the light, a point dipole model expresses both the absorption and the scattering of the electromagnetic field. The scattering and absorption cross sections are given by (Bohren & Huffman, 1983):

$$C_{scat} = \frac{1}{6\pi}\left(\frac{2\pi}{\lambda}\right)^4 |\alpha|^2 \quad ; \quad C_{abs} = \frac{2\pi}{\lambda} Im[\alpha] \tag{2.15}$$

with

$$\alpha = \frac{\omega_p^2}{\omega_p^2 - 3\omega^2 - i\gamma\omega} = 3V \left[\frac{\varepsilon_p/\varepsilon_m - 1}{\varepsilon_p/\varepsilon_m + 2} \right] \tag{2.16}$$

where, α is the polarizability of the particle, V is the volume, ε_p is the dielectric function of the particle, and ε_m is the dielectric function of the embedding medium.

From the above equations, when $\varepsilon_p = -2\varepsilon_m$, the polarizability of particle will become very large. This occurs when the frequency is close to the surface plasmon resonance, ω_{sp}. At this resonance, the scattering cross sectional area can be larger than the area of geometric cross section of the particle (Bohren & Huffman, 1983). For example, when small silver nanoparticles in air have a scattering cross section that is around ten times the cross sectional area of the particle, then the incident light can be fully absorbed and scattered just by a substrates covered with only 10% of the particles (Catchpole & Polman, 2008).

For organic solar cells device application, it is important to increase the scattering cross section rather than the absorption to have the light trapping by scattering effect. This effect can be achieved by controlling the size of particles. By tuning other parameters such as particle shape, particle distribution, and material of the particles, the surrounding medium also can contribute to increase the scattering effect of organic solar cells device (Atwater & Polman, 2010; Wu et al., 2011).
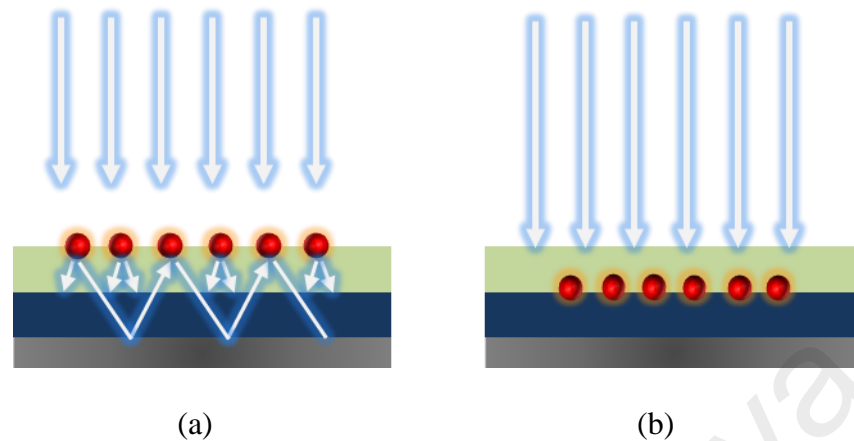
Figure 2.5 (a) Light trapping by scattering from metallic nanoparticles at the surface of a standard organic solar cell. The optical path length is increased because light is trapped into the device through multiple angle scattering. **(b)** Excitation of localized surface plasmons in metallic nanoparticles embedded in the organic solar cell.

2.3.2   The Local Field Enhancement

Strong local field enhancement around the metallic nanoparticles is an advantage that can benefit from resonance plasmon excitation in organic solar cell to increase the light absorption in its surrounding area i.e. in active organic layer of device. When the metallic nanoparticles are very similar or smaller in size compared with the wavelength of light, they can act as antennas for the incident light and store the energy in a localized surface plasmon modes with up to 100 times enhancement of the electric field (Duche et al., 2009; Rand et al., 2004). These antennas will be very useful in materials that have small carrier diffusion length like the conducting polymer with very short exciton lifetime. Indeed, the absorption rate should be higher than the reciprocal of the plasmon decay time to avoid the absorbed energy dissipate into ohmic damping in the metal (Atwater & Polman, 2010). This type of arrangement, where plasmonics structure are embedded in the active layer of organic device, is able to modify the coupling between

plasmon and exciton leading to the generations of the hot excitons (Wu et al., 2011). The hot excitons generation will increase the generation of free charges (Ohkita et al., 2008). Thus, the recombination of excitons can be reduced through radiative and non-radiative processes hence increasing the efficiency of the device (Figure 2.6) (Lee et al., 2008).
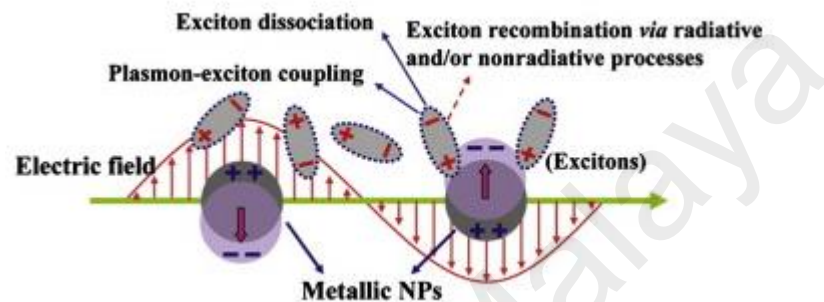
Figure 2.6 Depiction of the interaction between the localized surface plasmon resonance and the excitons. The interaction enhances the rate of exciton dissociation, thereby reducing the exciton recombination (Wu et al., 2011).

2.3.3   Metallic Nanoparticles Materials

Metallic nanoparticles materials that are commonly used for solar cells applications are usually made of metals that strongly interact with the sunlight such as aluminium, silver, gold, or copper. Metals like silver and aluminum have bright silvery appearance when exposed to sunlight because they are highly reflective across the entire visible spectrum. Metals like gold and copper are coloured because the high-frequency components of light are not well reflected, and the perceived light encloses predominantly colours in yellow to red wavelength range (Freise, 2012). In terms of surface plasmon resonance, aluminium and silver lead it to happen in the ultra violet spectrum while plasmon resonance for gold and copper happen in the visible spectrum (Catchpole & Polman, 2008). Recently, gold has been largely used for organic solar

cells application as it is believed that it will not be affected by oxidation and guarantees the long life of the device. However, the gold nanocluster at nanoscale range is able to act as an exothermic centre absorbing multiple molecules of oxygen (Frondelius et al., 2010). As a result, it is not possible to rule out the effects of oxidation in gold nanoparticles (Notarianni et al., 2014). Besides gold, silver is also widely studied for enhancing the performance of organic solar cells by plasmonic effects due to its low cost and low absorption. Even though silver suffers from oxidation effects and plasmonic properties are influenced but oxidation happens only on the surface, it can still be used for any plasmonic application (Kuzma et al., 2012).

2.4   Basic Study of Organic Solar Cells

A typical organic solar cell is composed of distinctive layers that can be organic and/or inorganic. A solar cell is defined as organic or inorganic depending on what the active absorbing layer is made of. If it is composed by only organic material, thus it is known as organic solar cell. The same goes to typical inorganic solar cell. The most common structure of an organic solar cell consists of two electrodes in which one of the two has to be transparent. In between the two electrodes, there will be the organic active layer where the generation of free charge carriers will occur. To prevent the reduction of the device's performance, insertion of buffer layer is usually needed to ensure that a charge selective transport occurrence could avoid the charge recombination effects. The inclusion of buffer layer is commonly between each electrode and active layer.

There are several ways to summarise the generation of a photocurrent from an incident light in organic solar cells. First is by the absorption of photon in conducting polymer, then by the creation of exciton (bound state of an electron and a hole, which are attracted to each other by electrostatic Coulomb force), and lastly by exciton separation at the interface of the heterojunction (interface between the donor and

acceptor material). The electrons and hole transportation to the respective acceptor and donor material that caused the creation of photocurrent is due to built-in electric field at the interface of heterojunction (Yang & Forrest, 2008). However, these steps react differently depending on the type of semiconductor. Whether it is organic or inorganic, made of crystalline or amorphous material, or bi-layer or bulk heterojunction photovoltaic (Rand & Richter, 2014). The following section explains briefly about the steps towards the generation of photocurrent in bi-layer organic solar cells made of amorphous organic material (Hoppe & Sariciftci, 2004).

2.4.1 Photo Absorption and Exciton Generation

In inorganic photovoltaics, the photon absorption produces two free charges of an electron in the conduction band and a hole in the valence band. In organic photovoltaics, the absorption of photon produces two charges, which are an electron in the lower unoccupied molecular orbital (LUMO) and a hole in the higher occupied molecular orbital (HOMO). However, they are very much bound to each other due to lower dielectric constant that is usually observed in inorganic materials (Jørgensen et al., 2008). Generally, when an electron receives energy from the photon, it will be excited from HOMO to LUMO leaving a hole behind. However, this excited electron still cannot move freely within the LUMO as the bound state neutral electron-hole pairs called exciton is generated. Figure 2.7 shows the illustration of exciton generation within the donor material. The next step is the exciton diffusion.

Photo absorption   *Excitation of electron*   *Exciton generation*
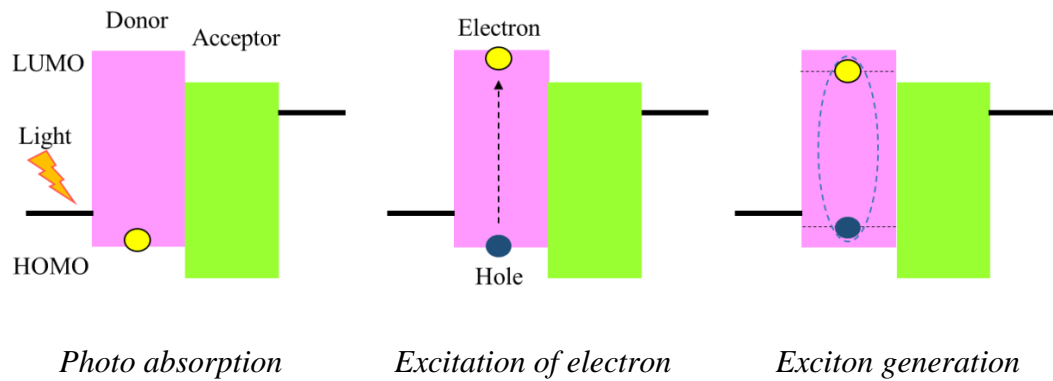
Figure 2.7 The process of exciton generation in organic solar cells

2.4.2 Exciton Diffusion

Exciton diffusion is when the electron-hole pair migrates in organic semiconductor. In this process the exciton diffuses from donor towards donor-acceptor interface. Only excitons that reach donor-acceptor will be dissociated where this excitons dissociation is important in photocurrent generation. Since the excitons has finite lifetime, the diffusion length, which is the travel distance to donor-acceptor, is limited. Therefore, to let the exciton dissociate, it must be formed within the diffusion length or it will decay back to its ground state. Figure 2.8 shows the exciton migrating towards donor-acceptor interface in organic semiconductor of a bi-layer organic solar cell.

Exciton generation   *Exciton diffusion*
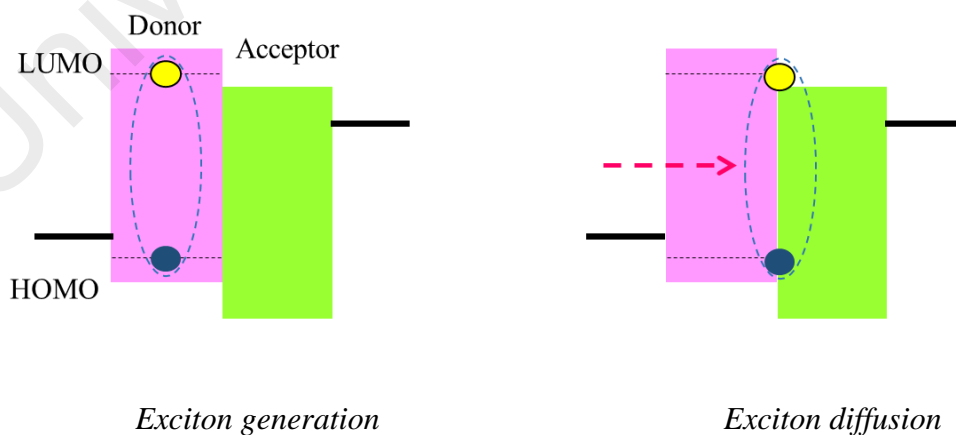
Figure 2.8 Exciton diffuses towards donor-acceptor interface

26

2.4.3 Exciton Dissociation

The exciton dissociation process is really important to the photocurrent generation, which normally occurs during this process. Instead of exciton decay, in organic photovoltaic, the exciton is separated into mobile charge carriers. The carriers that form exciton upon the presence of light will be dissociated into free electron and hole at donor-acceptor. Note that, the dissociation of exciton requires a strong acceptor component so that the electron can escape from the bound state with hole before it can be separated. The process of exciton dissociation is depicted in the figure below.

Exciton diffusion   *Exciton dissociation*
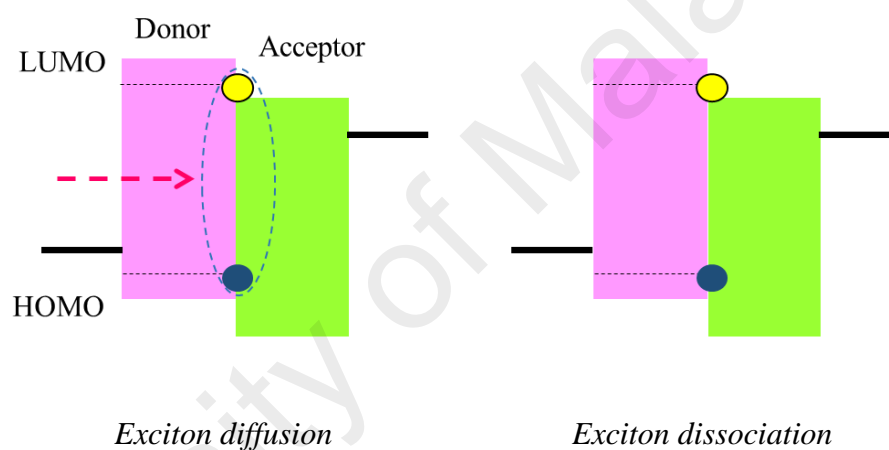
Figure 2.9 Exciton dissociation process right after diffusion

2.4.4 Charges Transport and Collection

The dissociated excitons into mobile electron and holes must be transported and collected to respective electrode. This final phenomenon of charge leads to the photocurrent generation. The charge-carriers can travel in opposite directions to the respective electrodes for collection. This transport is enabled by charge-carrier diffusion and the force is experienced by the charges due to the bias across the electrode. Positive holes will move along donor molecules because of diffusion (electrochemical gradient-driven) and/or drift (driven by built-in electric field) towards the anode, while electrons will move along electron acceptor molecules in a direction opposite to the holes,

towards the cathode. Charges that reach the electrodes can then be extracted. The total

current density in a solar cell is the sum of the drift currents driven by the electric field

and by diffusion current driven by the concentration gradient of the carriers.

Charge transport   *Charge collection*
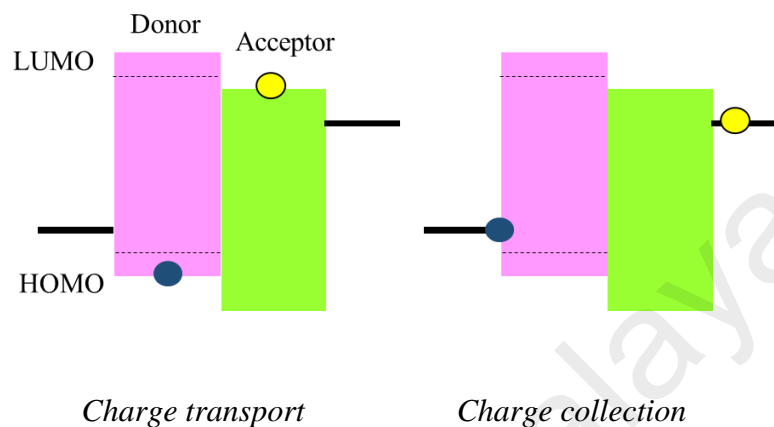
Figure 2.10 Charges transport and charges collection at respective electrodes

2.4.5   Current-Voltage (I-V) Characterization

Generally, an organic solar cells device involves several important parameters such

as maximum output current density (J_{max}), maximum output voltage (V_{max}), maximum

output power (P_{max}), open-circuit voltage (V_{oc}), short circuit current density (J_{sc}), and fill

factor (*FF*). All of these parameters are used to determine its power conversion

efficiency (η) and can be extracted from a current-density (J-V) curve (Ishii et al.,

2015). A schematic diagram of the current density–voltage curve of an organic solar cell

under illumination is as shown in Figure 2.11.
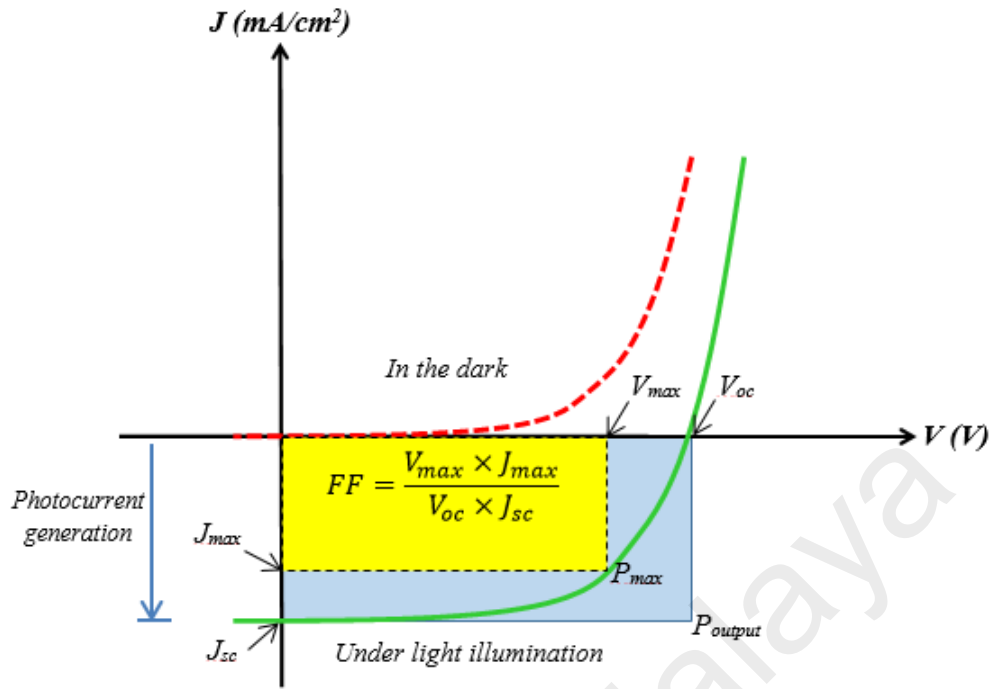
Figure 2.11 The current density versus voltage (J-V) curve of OSCs

Typically, during charge transport and collection, the separated electrons and holes flow towards the low and high work function electrodes respectively. Accordingly, the open circuit voltage (V_{oc}) is the potential difference maximum value reached by the collection of free charge carriers at respective electrodes (Elumalai & Uddin, 2016). A current flow is produced when connection is made to both electrodes allowing the free charge carriers to circulate throughout the external circuit. The short circuit current density (J_{sc}) is the maximum current that can flow throughout the cell and is determined under illumination when the potential is zero (Lu et al., 2014). As shown in the figure the square of $J_{max} \times V_{max}$ produced the maximum power (P_{max}) and the fill factor (FF) is given by ($J_{max} \times V_{max}$) / ($V_{oc} \times J_{sc}$). Then, the power conversion efficiency (η) of the OSC device is defined as the ratio of the maximum generated electrical power (P_{max}) compared with the incident optical power (P_{input}) from light illumination into the OSCs (Rand & Richter, 2014): $\eta = \frac{P_{max}}{P_{input}} = \frac{FF \times (J_{sc} \times V_{oc})}{P_{input}}$. The characterization of OSC performance has to be done by using a standard value of illumination, which is defined

as 100 mW/cm^2 as suggested by Committee Internationale d'Eclairage (CIE) or International Commission on Illumination (International Commission on Illumination & Committee, 1970).

2.5   Improving VOPcPhO:P3HT Organic Solar Cells Device

Other than improving the absorption of solar spectrum, materials from phthalocyanine family have been reported to exhibit very intense absorption in the UV-Vis spectral region (El-Nahass et al., 2005; Şener et al., 2008; Shen et al., 2008; Varotto et al., 2010). It also has been testified that the electron's mobility in phthalocyanines can be as high as the hole's mobility (Kraus et al., 2010). Vanadyl 2,9,16,23-tetraphenoxy-29H,31H-phthalocyanine (VOPcPhO) is among the phthalocyanines, which has a dominant absorption in the Q-band region specifically from 600 nm to 750 nm. That is the range where the P3HT absorbs very little (Abdullah et al., 2012). The VOPcPhO has high solubility in a variety of organic solvents, which makes it attractive to use for photovoltaic applications (Ahmad Makinudin et al., 2015).

Due to the above-mentioned interesting properties of VOPcPhO, a work on a new system of donor–accepter blend for bulk heterojunction solar cell of poly(3-hexylthiophene) (P3HT) by using vanadyl 2,9,16,23-tetraphenoxy-29H,31H-phthalocyanine (VOPcPhO) as acceptor material has been fabricated and characterized for its electrical and optical properties (Abdullah et al., 2012). They reported that the P3HT:VOPcPhO blend system has the potential to be applied in bulk heterojunction solar cells, due to its high absorption solar spectrum in the visible region and considerably good electrical behaviour.

Although several research has been done to investigate the properties of this material blend or the material VOPcPhO itself, very little or none reported that work has been done to improve its properties as bulk heterojunction organic solar cells especially by

the inclusion of plasmonics features (Izzat Azmer et al., 2016; Supangat et al., 2014). The inclusion of metallic particles in this device will become an added proof of the study on plasmonics behaviour in organic solar cells; despite most studies have been done towards an already high performance organic solar cells material. Other than that, this study shall significantly show the tunability of plasmonics behaviour to increase light absorption inside the organic active photovoltaic layer.

As previously explained, several processes were include in photocurrent generation which started with light absorption, then the formation of excitons, followed by the exciton diffusion towards donor-acceptor interface and subsequently dissociates into free electrons and holes. The separated free electrons and holes are then transported through their distinct percolating pathways, and then extracted by the corresponding electrodes. Hence, the improvement in efficiency and the devices performance can take part in one or more of those photocurrent generation steps. For this research, the inclusion of plasmonics features on top of ITO layer in the OSCs was meant to trap and confine light. Consequently, the device performance enhancement by this approach was generated at the first step of photocurrent generation, which is enhancing the performance of light absorption of the device.

CHAPTER 3: EXPERIMENTAL METHOD

In this chapter we will discuss the details about experimental works that have been carried out in achieving the research objectives, from the very beginning of finding the best features of silver particles in tailoring plasmonic properties that are suitable for incorporation with organic solar cells. This chapter is prepared in two sections. First is the fabrication of silver particles and another one is the fabrication of plasmonic organic solar cells.

3.1   Substrates Preparation

Basically, glass and indium-tin oxide (ITO) coated glass are substrates that have been used throughout the experiments in this research. The glass substrate was used prior to the experiment for characterization and optimization purposes while the ITO coated glass substrate was used for the end product of organic solar cells. The plain ITO substrates were bought from Ossila with resistivity of ~30 ohm. Glass substrate was from local laboratory equipment supplier.

Before beginning any experiment or samples deposition, substrates must be cleaned thoroughly as the surface cleanliness may affect the precision of samples deposition. These three substrates have different ways of cleaning. Practically, the way of cleaning glass and ITO are almost the same and only differs in the use of cleaning solvent. The steps of cleaning those substrates are listed as follows:

Steps to clean glass substrate

1. Mix DI water with decorn soap water in a beaker with ratio 2:1

2. Immerse glass substrate in the mixture and sonicate for 15 minutes.

3. Rinse the substrate with DI water until the indications of soap disappeared.

4. Rinse the substrate with acetone and ethanol respectively.

5. Finally, rinse the substrate again with DI water.

6. Dry the substrate using nitrogen blow to finish the cleaning process.

Steps to clean ITO coated glass substrate

1. Mix DI water with decorn soap water in a beaker with ratio 2:1

2. Immerse glass substrate in the mixture and sonicate for 15 minutes.

3. Rinse the substrate with DI water until the indications of soap disappeared.

4. Rinse the substrate with acetone and iso-propanol respectively.

5. Finally, rinse the substrate again with DI water.

6. Dry the substrate using nitrogen blow to finish the cleaning process.

3.2 The Deposition Process of Silver Particles

In order to study how different features of silver particles film change the optical properties of the film, various techniques have been used to obtain different types of silver particles film. The best features and technique were selected in the proceeding of fabricating plasmonic organic solar cells. This section explains the general procedure about the technique that has been used for integrating its yield in organic solar cells device. The factors of choosing the specific technique will be discussed in the next chapter.

3.2.1 Electron Beam Deposition

Electron beam (e-beam) evaporation process is a "top-down" fabrication method of metal nanoparticles along with other methods that are categorized under physical vapour deposition such as e-beam lithography, sputter coating, and thermal evaporator. In the present study, an e-beam evaporation machine assembled by Korea Coating Materials and Components (KCMC) model EB43-T was used to produce silver nanoparticles (Ag NPs). This e-beam evaporation machine consists of two main parts

where the first part is the vacuum system and the second part is the deposition system (Figure 3.1). Every part has their own several components and each component plays an important role in running the whole system and depositing the metal. All the components and works are as follows;

a) *Vacuum Systems of e-Beam Process*

Figure 3.1 shows the schematic diagram of the vacuum system of an e-beam machine. The vacuum system is important in initiating the e-beam evaporation process. The role of this system is to pump the chamber where the deposition system is located. It is important to vacuum the chamber prior to the deposition process. This vacuum system consists of:

i. *Rotary Pump*

A rotary pump is a foundation of a system where it initiates the pump process of the whole system. In this system, a rotary pump has two functions. First is to initiate the pumping process of the chamber from a high pressure of atmospheric pressure and secondly is to back pump the turbo molecular pump. Even though the rotary pump is strong enough to suck out the molecules from the atmospheric pressure of the surrounding chamber, it can only pump the deposition chamber down to $\sim 1 \times 10^{-3}$ mbar. This reading of pressure is still not enough for pursuing the deposition process. So, other high power pump is needed to pump down the chamber to a lower pressure of $\sim 1 \times 10^{-7}$. Then, for this part another component namely *turbo molecular pump* was operated.

The turbo molecular pump is a high-speed pump that can pump down a chamber to a lower pressure compared with the rotary pump as previously stated. The maximum speed of motor fan for this turbo pump is up to 633 Hz (rotations per second), which is very high. Therefore, only small molecules can be sucked out and big particles should be extremely avoided to maintain its workability because sucking big particles may damage the fan blades of the pump. This is also the reason why the rotary pump must initiate the chamber vacuum process before the turbo molecular pump takes turn. On the other hand, this turbo pump can be run by its own, but must be backed by the turbo molecular pump. In the turn on process the rotary pump must be operated first before the turbo pump while in the shutdown process the turbo pump must be stopped first before the rotary pump.

b) *Deposition System*

The deposition system is located in a chamber in the e-beam machine where the processes of depositing samples happen here. Figure 3.2 shows the schematic diagram of the deposition system inside the chamber. The deposition system consists of several components that are very important in taking part in the deposition process. Inside the chamber, with the help of a built-in substrate holder, substrates are located at the top position and are faced downwards. The target metals are located at the bottom with other depositing components.

To start the deposition process, the chamber of the deposition system has been pumped down by the vacuum system as explained earlier. When the pressure of the chamber reaches the reading of $\sim 1 \times 10^{-5}$ to $\sim 1 \times 10^{-7}$, it means the deposition process

is ready to be operated. To initiate, the power supply is turned on to allow current to flow through the tungsten filament inside the chamber (Figure 3.2). The tungsten filament is where electrons are emitted from to be beamed on the target metal. Then, the amount of current and voltage are increased high enough for the tungsten filament to emit electrons. When the electrons are emitted, a deflecting magnet will bend the electrons pathway so they will beam directly onto the metal targets. The electron beam causes the atoms from the target metal to transform into a gaseous phase. These gaseous atoms will then precipitate into a solid form, coating everything in the vacuum chamber.

However, the amount of metal coating should be control following desired thickness. Hence, a shutter and a thickness monitor are included in the deposition system inside the vacuum chamber. There is a thickness monitor positioned at the same level with the substrate setting and it is connected to a programmed control unit. At the control unit box, there is display screen that shows the deposition rate (thickness (Å) / time (seconds)) and the progressing deposited thickness. However, some parameters must be set at the control unit before fully relying on the displayed rate and thickness. Basically, the parameters are the information about the target metal material, whereas different materials have different properties and different amount of electrons are needed to be ditched out. The deposition rate can be simply changed by tuning the amount of current flows. As the desired deposition rate is achieved and the substrates are ready to be coated, the shutter would open and the deposition time starts to count simultaneously. Whereas, as the desired thickness is achieved, the shutter would close and time counted would stopped instantly. Note that the shutter is situated between the metal target and substrate positions.
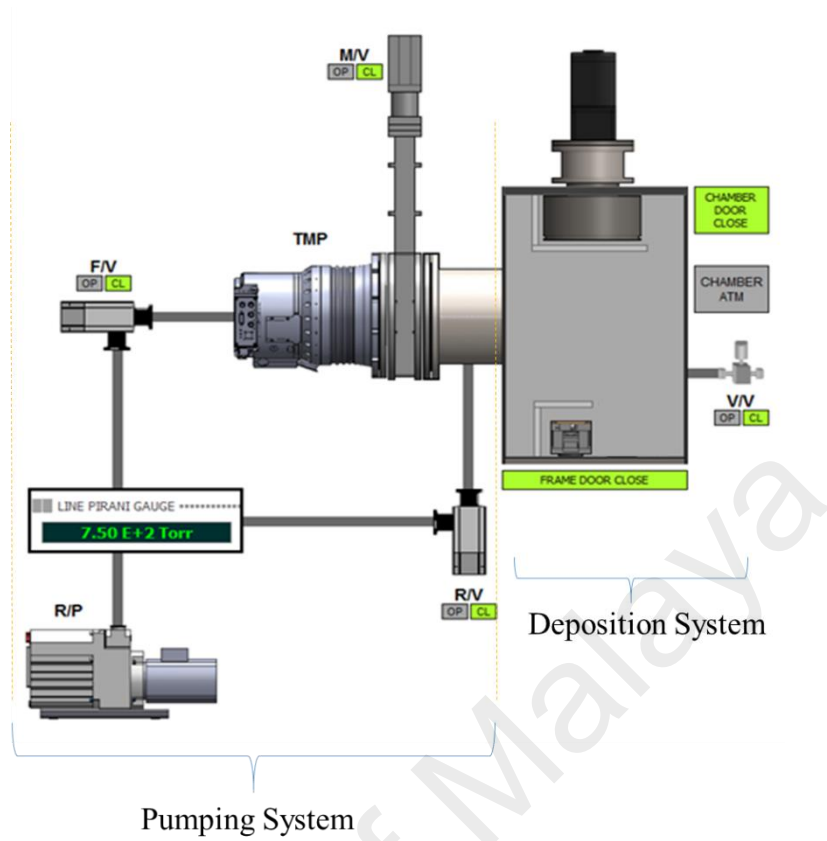
Figure 3.1 Schematic of the whole e-beam system model EB43-T
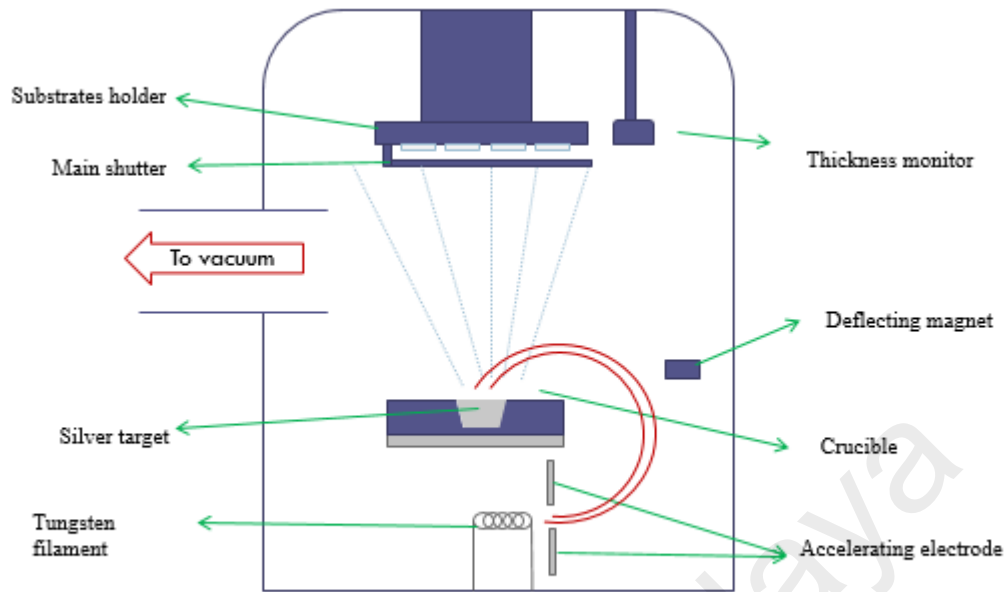
Figure 3.2 Schematic diagram of deposition process inside the chamber of deposition system of e-beam technique

3.2.2 Electrophoretic Deposition Technique

Electrophoretic deposition (EPD) is a term for a broad range of industrial processes, which includes electro-coating, e-coating, cathodic electrodeposition, anodic electrodeposition, and electrophoretic coating, or electrophoretic painting. A characteristic feature of this process is that colloidal particles suspended in a liquid medium will move under the influence of an electric field (electrophoresis) and is deposited onto a substrate electrode. Materials that are involved in electrophoretic deposition are all colloidal particles that can be used to form stable suspensions and can carry a charge. These include materials such as polymers, pigments, dyes, ceramics, and metals.

Literally, as depicted in Figure 3.3, the experimental set up of this technique consists of an electrical power supply that is connected to a pair of electrode where one of the

electrodes must be the substrate to collect the deposited materials. Those electrodes must be immersed in the colloidal dispersion of desired materials.

In this work, two types of colloids have been used to deposit silver particles. One is colloid silver dispersion in aqueous buffer solution that was obtained directly from the supplier, Sigma Aldrich. The other one is silver nitrate that undergoes several processes to form colloid. Both types of solutions gave different unique types of plasmonic features that will be further discussed in Chapter 5.
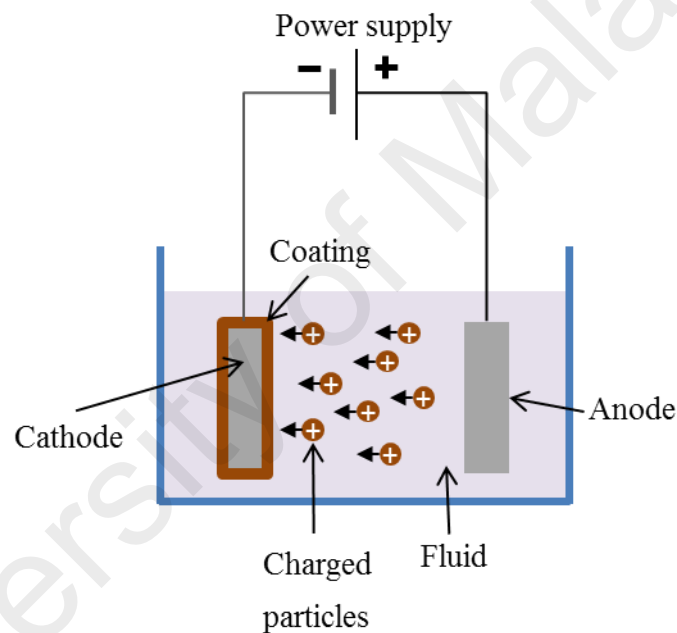
Figure 3.3 Schematic diagram of electrophoretic deposition process

3.2.3   Spin Coating Technique

Generally, spin coating is a technique that has been used to deposit uniform thin films onto a flat substrate by using a machine called spin coater. Usually, the procedure begins by putting a small amount of coating material (normally in a form of liquid) on the centre of the substrate. The substrate may be already being spinning at low speed or

not spinning at all. The substrate is then spun at high speed of rotation to spread the coating material by centrifugal force.

Rotation continues while the fluid spins off to the edges of the substrate and until the desired thickness of the film is achieved. The solvent used is usually volatile, and simultaneously evaporates. Thus, the higher the angular speed of spinning, the thinner the film. Other than that, the thickness of the film may also depend on some parameters like the viscosity and concentration of the solution and the solvent. In this research the spin coater has been used for the deposition of silver particles and in the process of device fabrication. The details of the procedure of each coating were explained in respective sections.

Figure 3.4 Spin coater machine that has been used in this research

3.3   Characterization of Silver Particles Structure

The two main things that should be taken into account in the study of plasmonics are the type of structure of metal nanoparticles and its plasmon resonance behaviour. Thus,

imaging and scattering behaviour characterization must be carried out. In this research, field emission scanning electron microscopy (FESEM) has been used to study the surface structure of the deposited silver particles and UV/VIS/NIR spectroscopy was used to study their plasmon resonance behaviour.

3.3.1   Field Emission Scanning Electron Microscopy (FESEM)

FESEM imaging is commonly used in the study of microstructure and thin film fabrication. Like normal SEM (scanning electron microscopy) imaging, FESEM imaging is meant to capture the structure of tiny objects. However, instead of focusing on micro-sized objects, FESEM imaging is more powerful that it can capture the size of structures in the nano range. The FESEM machine that was used in the present study is JEOL JBM-7600F. The quality of FESEM images depends on the type of samples. For example, the non-conductive surface of samples usually gives poor quality image and are hard to focus compared with conductive surface.

FESEM technique was used to study the morphology of the film surface. Throughout the scanning process, a film specimen was bombarded with electrons generated from a source and elastically reflected from the specimen. This energetic incident beam will then produce secondary electrons and X-rays from the specimen surface. This causes a small energy loss and change in the path of incident beam. As a result, ionization of electrons occurs in the specimen atom. An image is obtained from several secondary electrons that are produced by each of the incident electron. The film thickness is measured from the cross-section of the SEM image of the sample. The size of particles in the film can be measured directly from the FESEM images using the scale of the scanning magnification. Figure 3.5 shows the FESEM system that was used in this research.

As the work concept of an FESEM machine captures image by the beam of electrons on the sample's surface, charging may happen on non-conductive surface and may burn the samples. Hence, for non-conductive surface samples, a layer of metal like gold must be coated first before proceeding for characterization.

Figure 3.5 FESEM machine used in the research

3.3.2   UV/VIS/NIR Spectrophotometer

Spectroscopy is the study of the interaction of electromagnetic radiation (in the range of ultraviolet, visible, and near infrared range) and a matter, whereas spectrophotometer is an instrument to measure spectroscopy. In this study, the electromagnetic radiation used are in the range of ultraviolet, visible, or near infra-red (UV-Vis/NIR). It measures the intensity of light passing through a sample (I), and compares it to the intensity of light before it passes through the sample (I_o). The ratio I/I_o is called *transmittance*, and is usually expressed as a percentage (%T). The absorbance, A, is based on the transmittance where $A = -log\frac{T\%}{100\%}$. R% is the reflectance percentage obtained from

the ratio of intensity of light reflected from a sample to the intensity of light reflected of a reflectance material.

In this research, PERKIN ELMER LAMBDA 750 UV-vis spectrometer has been utilized to study the visible wavelength absorption profile of the photoactive films of the photodetectors. The instrument parameters and works have been controlled by UV Winlab version 6 software. The image and technical specifications of PERKIN ELMER LAMBDA 750 UV-vis spectrometer are as follows:
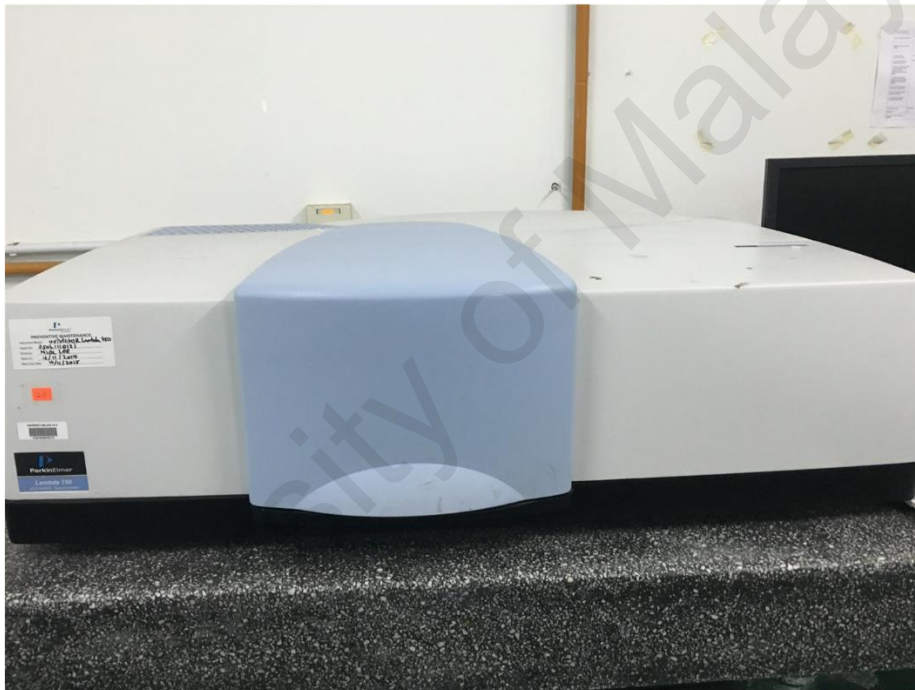
Figure 3.6 UV/VIS/NIR spectrophotometer PERKIN ELMER LAMBDA 750
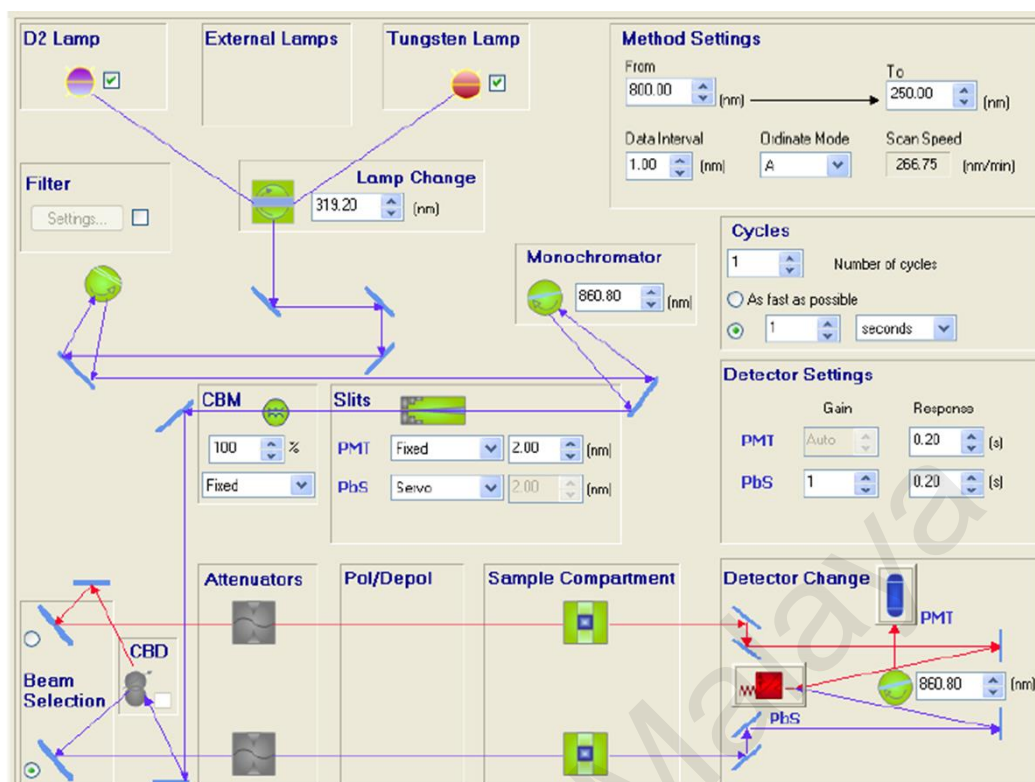
Figure 3.7 Software configurations of method settings for UV-Vis measurement

Table 3.1 Specifications of UV/VIS/NIR spectroscopy

Wavelength range	190 nm – 3,300 nm
Wavelength accuracy	± 0.15 nm UV/vis ± 0.5 nm NIR
Wavelength reproducibility	UV/vis ≤ 0.06 nm
Light source	Tungsten-Halogen (vis) and Deuterium (UV)
Light detector	Photomultiplier R955

3.4   Fabrication of Solar Cells Device

There are several steps in the process of fabricating organic solar cells device. Generally, the steps are preparing materials solutions, deposition of thin film layers which includes buffer layer and active layer, and lastly deposition of top electrode. In this fabrication, aluminium was used as the top electrode material. Basically, some annealing is needed throughout the process.

3.4.1   Materials and Solution Preparation

Before proceeding with the deposition of thin film layers, choosing the material for buffer layer and active layer must be made first. In the present research the materials used for buffer and active layer are as follows:

      i.   The PEDOT:PSS as buffer layer

Thin film of Poly (3,4-ethylenedioxythiophene):poly(styrene sulfonate) (PEDOT:PSS) was used in the device structure to act as buffer layer because of its high work function. The supplementary advantages of buffer layer are that it displays smooth morphology and high conductivity thereby assisting efficient hole collection at ITO anode (Zhang et al., 2004). Because of its desirable work function, it is frequently applied to decrease the energy barrier at the electrode/organic interface to improve the charge extraction (Saito, 2007). In addition, this type of buffer layer material is well known in its high transparency in the visible range and thermal stability. For the present study, aqueous dispersion of Heraeus Clevios™ PH1000 PEDOT:PSS with conductivity 900–1000 S/cm has been used. Prior to deposition of PEDOT:PSS layer, its aqueous dispersion has been filtered by commercially available nylon 0.45 µm filters to obtain uniform smooth surface morphology. Figure 3.8 shows the molecular structure of PEDOT:PSS.
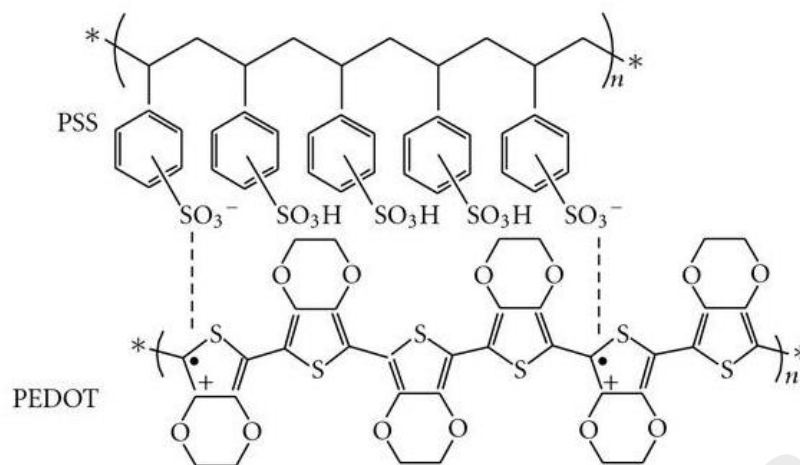
Figure 3.8 Molecular Structure of PEDOT:PSS

ii. P3HT:VOPcPhO Material Blend as Thin Active Layer

P3HT (regioregular poly (3-hexylthiophene-2,5-diyl)) and VOPcPhO (vanadyl 2,9,16,23-tetraphenoxy-29H,31H-phthalocyanine, with dye content 98 %) are photo-sensitive organic materials. For the present research work, these materials have been used for active material in the device and were obtained from Sigma-Aldrich (product of Rieke Metal®, Inc.). P3HT is a π-conjugated polymer that has greater than 90% regioregularity. Its molecular formula is $(C_{10}H_{14}S)_n$ and it has high solubility in most of organic solvents (Machui et al., 2012). On the other hand, one of phthalocyanine (Pc) derivatives, VOPcPhO ($C_{56}H_{32}N_8O_5V$), has a good solubility in organic solvents. For both in powder and solution form, VOPCPhO appears to be dark green in colour. By virtue of their desirable solubility in organic solvents, P3HT and VOPCPhO find their extensive use in the fabrication of solution processable devices. Both of these materials are well known electron donor materials, which are normally used in the fabrication of OSCs. Both P3HT and VOPCPhO materials have been dissolved in chloroform (with 99.99% purity) in 20mg/ml concentration separately. The solutions have been stirred at 200 rpm stirring speed at room temperature using magnetic stirring bar for at least an hour so that they will dissolve completely. The solutions have been filtered using

disposable PTFE filter (filtration membranes size ~0.25μm). The P3HT:VOPcPhO blend was prepared by mixing the P3HT and the VOPcPhO material in the ratio of 1:1.5. The mixed solutions was stirred up to 24 hours until it was well blended prior to the deposition of active thin film.
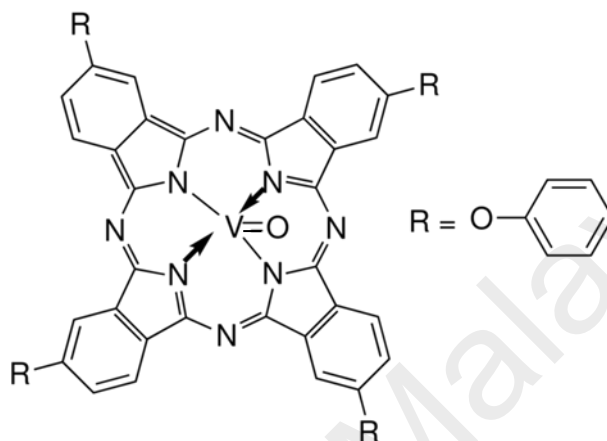
Figure 3.9 The molecular structure of Vanadyl 2,9,16,23-tetraphenoxy-29H,31H-phthalocyanine (VOPcPhO)

3.4.2   Deposition of Organic Thin Films

As it has been introduced earlier about spin coating technique, it has been majorly used in the fabrication of OSCs device. Both PEDOT:PSS buffer layer and P3HT:VOPcPhO thin active layer were deposited by using this technique employing previously mentioned spin coater from Laurell model WS-650MZ-23NPP. A small amount of solution is dispensed on the top surface of cleansed substrate just before it is spun with a desired spin rate. Figure 3.6 shows the spin-coating process for the thin film formation.
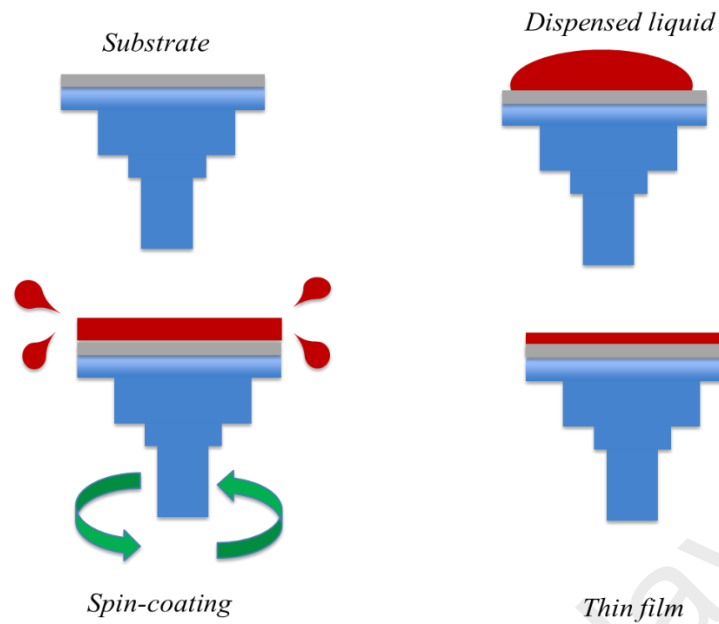
Figure 3.10 Spin coating process

Device fabrication began by adding a buffer layer of PEDOT:PSS on ITO substrates (~10 Ω sheet resistance) employing spin-coating technique at 3,000 rpm for 60 s. Samples were then annealed on a hot plate at 120 ^{0}C for 30 minutes to let it dry completely and also to increase its conductivity. At this parameter, the PEDOT:PSS buffer layer will usually form ~40 nm thick layer. Subsequently, another layer of VOPcPhO: P3HT, which acts as the active material was spun onto the sample at 3,000 rpm for 30 s to get the thickness of about 100 nm to 150 nm followed by annealing process at 120 ^{0}C for 30 minutes. Several sets of individual films (different in concentration) have been prepared at several spin rates for the optimization of thin film. These sample films were used for the material characterization prior to the device fabrication.

3.4.3   Top Aluminium Electrode Deposition

To complete the organic solar cells device fabrication, top electrode must be deposited on top of the active layer. The materials for top electrode that have been used is aluminium (Al). Edwards AUTO 306 thermal evaporator has been utilized in present research work for the deposition of Al cathode. This machine is automatically controlled by Automatic 306 microprocessor based controller. As the e-beam machine, this thermal evaporator was also built with its own pumping system that consists of turbo molecular pump and rotary pump. The rotary pump and turbo molecular pump were respectively for rough pumping and fine pumping to let the thermal chamber be in the vacuum. The chamber consists of electrodes to place target material, samples holder, and thickness monitor.

To start the deposition, the chamber must be pumped down to reach the vacuum state (Pressure: $< 1 \times 10^{-6}$ mbar). While in the chamber, two electrodes were connected to a tungsten filament and a few of Al wires were tightly tied to that filament. The prepared samples for the deposition were placed on the sample holder facing down the Al target. The arrangement was set in a chamber that was closed tightly. After the desired pressure was reached, the deposition of aluminium electrode started. The current was slowly increased so that the tungsten filament coil could heat up. At a certain point, the tungsten filament reached the temperature of Al melting point. After the Al wires melted and covered up the tungsten filament, the current continued to increase until at a certain point it will be evaporated and consequently deposited on the samples. The shutter will be opened for about 40 s to let Al deposited on samples to get 100 nm thick of Al electrode. Figure 3.10 below shows the arrangement of the thermal evaporator.
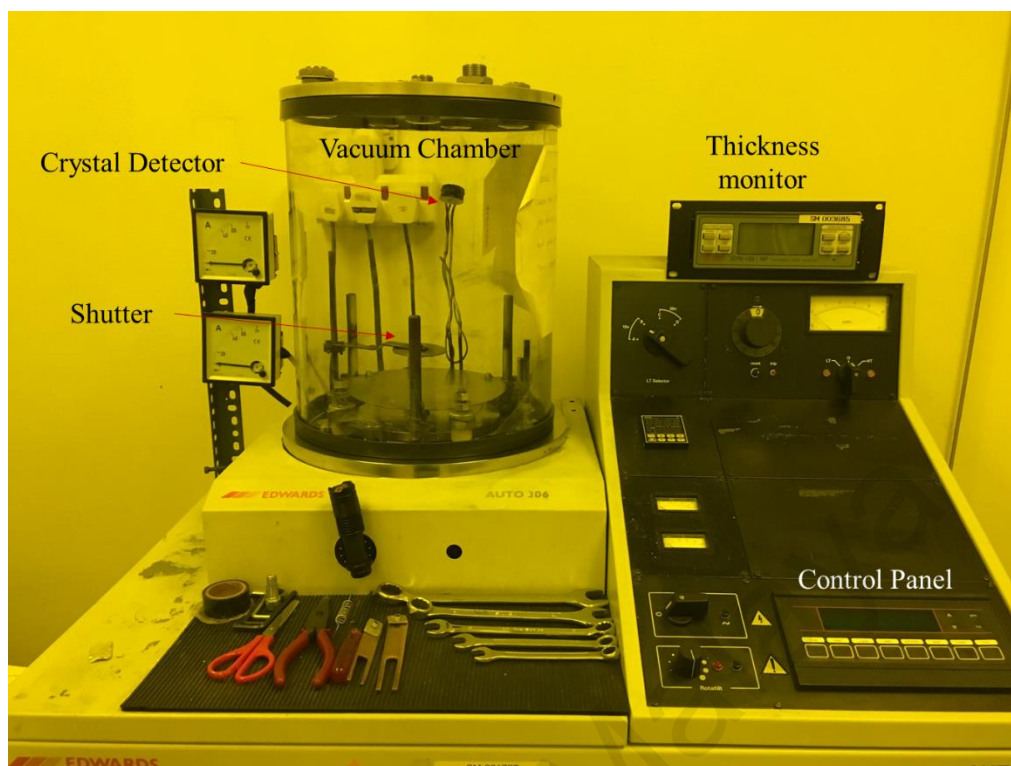
Figure 3.11 Thermal Evaporator System (Edwards Auto 306)
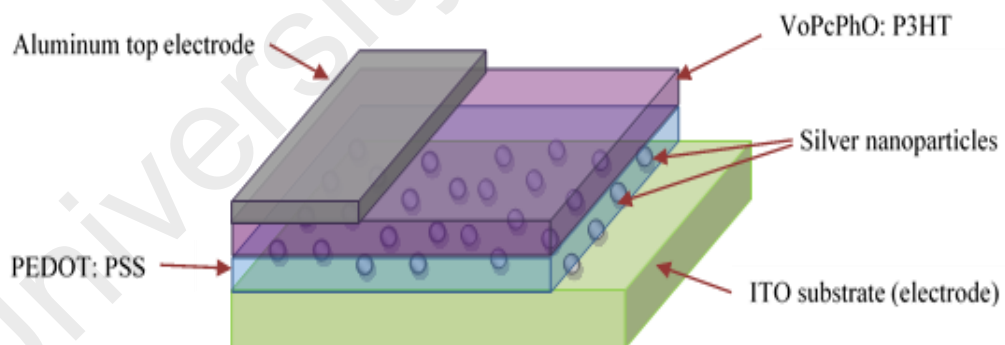
Figure 3.12 Schematic diagram of complete deposited organic solar cells device with introduction of Ag NPs

3.5 Characterization of Organic Solar Cells Device

The main characterization used in this research can be sectioned into two. First is the optical characterization of the deposited organic layers and the other is the electrical characterization of fabricated device. For optical study, the same UV/VIS/NIR spectrophotometer as mentioned previously for nanostructures study has been utilized. In this study, the spectrophotometer is used to observe the absorption behaviour in the organic active layer. Furthermore, the absorption spectra of bare organic active layer will be compared with the one that has Ag structures included. The optical characterization should indicate some significant increase in light absorption of the device active layer. Thus, the same as previously mentioned PERKIN ELMER's model UV/VIS/NIR spectroscopy has been utilized to study the photo absorption of organic thin layer film with and without silver particles.

However, in optimizing the organic materials layer, KLA-TENCOR P6 Surface Profiler has been used to measure the thickness of buffer layer and active thin layer. The working principle of P-6 profilometer is based on the movement of diamond stylus on thin film surface. Thus, it can measure the step heights and surface roughness. Figure 3.12 depicts the KLA-Tencor P-6 Surface Profiler that has been used.
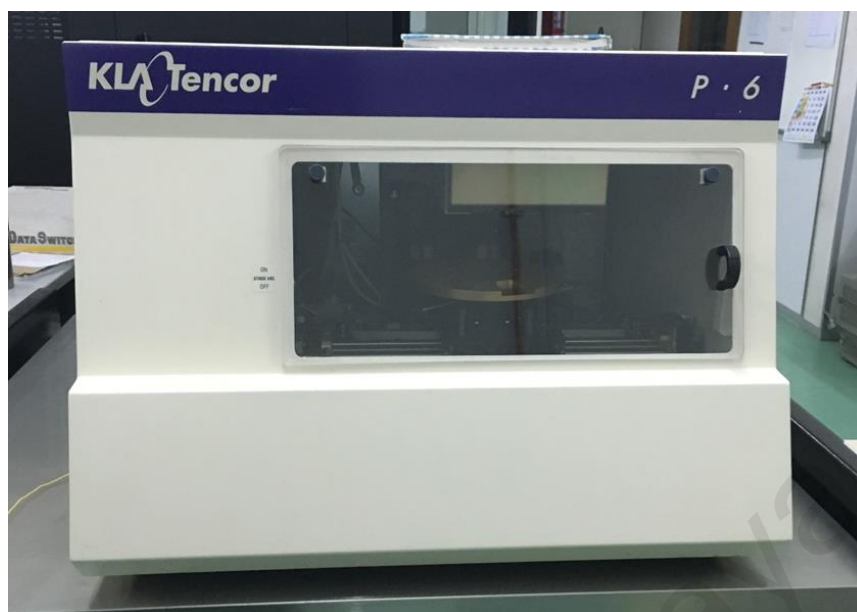
Figure 3.13 KLA-Tencor P-6 Surface Profiler

3.5.1 Photoluminescence (PL) Spectroscopy

The photoluminescence (PL) spectroscopy study gives helpful information in organic light emitting diode (OLED) and OSC studies regarding the optoelectronic properties of the photoactive materials. In OLED application, higher PL spectrum is desired indicating a better material for the production of light due to the large number of recombination units. While in OSC application, lower magnitude of PL peak is preferable for the production of photocurrent due to less recombination process. The PL results might give a first perception on electron-hole pair interaction that either tend to recombine back or further dissociate under a circumstance where energy is emitted in the form of photonic energy.

In the present research work, a luminescence spectroscopy machine by Perkin Elmer (model LS-50B) has been utilized to study the improvement of thin organic film when added with Ag structures. The measurement of PL was purposely conducted to investigate the potential improvement made by including Ag particles towards organic active material in the mean to lessen the recombination process. This measurement was

done to the samples of Ag structures in which the samples are difficult in pursuing for device fabrication to observe the electrical improvement.

3.5.2   Current-Voltage (I-V) Measurement

Figure (a) depicts the schematic of the electrical arrangement used to measure the I-V characteristics of OSCs. The solar illumination source for the measurement of device in light, a laboratory assembled solar simulator using Xe and Hg (Xe) bulb, enclosed in the 50 to 500 W NEWPORT 67005 arc lamp housing and sourced by NEWPORT 69907 Oriel Digital Arc Lamp Power Supply, has been used. The I-V measurements of the OSCs were attained using Signatone H-150 manual probe station equipped with keithley-236 source measurement unit (SMU). Electrical contacts with the electrodes of devices were assisted by magnetic-based micro positioners (Signatone S-600) placed at platen of the probe station. Data acquisition from SMU was done by interfacing it to the computer with NI LABVIEW software. Figure 3.14 (b) portrays the probe station along with solar simulator used to measure the I-V characteristics of the photodiodes.
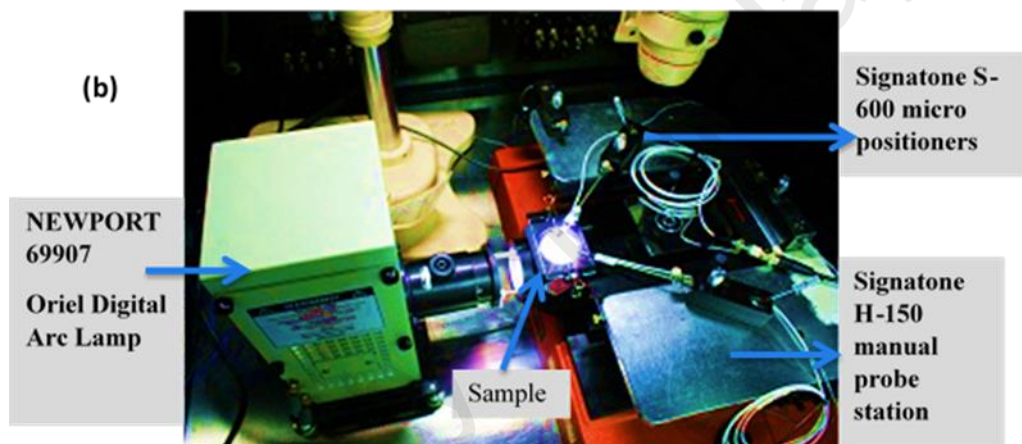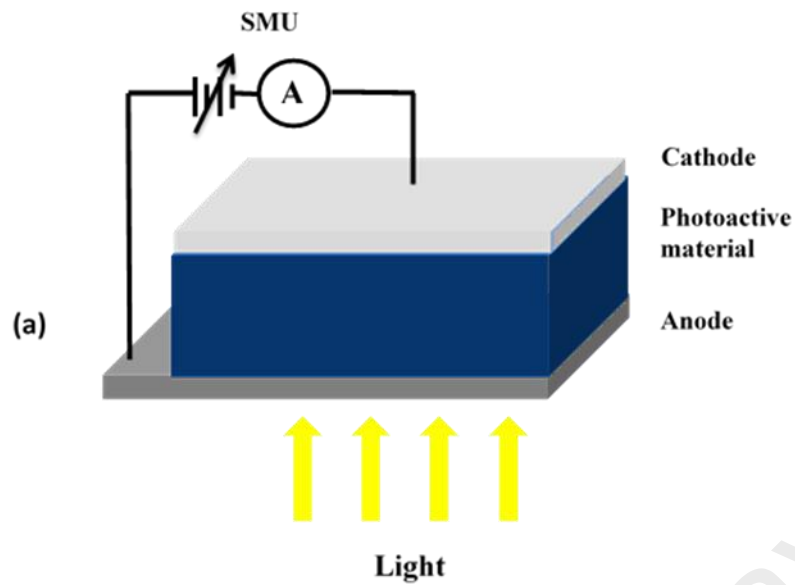
Figure 3.14 (a) Schematic of the photoelectric characterization of photodetectors, **(b)** Signatone H-150 manual probe station used for measuring I-V characteristics of photodetectors

3.6 FDTD Simulation

Finite-difference time-domain or Yee's method (named after the Chinese American applied mathematician Kane S. Yee, born 1934) is a numerical analysis technique used for modelling computational electrodynamics (finding approximate solutions to the associated system of differential equations). Since it is a time-domain method, FDTD solutions can cover a wide frequency range with a single simulation run, and treat nonlinear material properties in a natural way.

The FDTD method belongs in the general class of grid-based differential numerical modelling methods (finite difference methods). The time-dependent Maxwell's equations (in partially different form) are discretized using central-difference approximations to the space and time partial derivatives. The resulting finite-difference equations are solved in either software or hardware in a leapfrog manner: the electric field vector components in a volume of space are solved at a given instant in time; then the magnetic field vector components in the same spatial volume are solved at the next instant in time; and the process is repeated over and over again until the desired transient or steady-state electromagnetic field behaviour is fully evolved.

CHAPTER 4: OPTICAL STUDY OF PLASMONICS NANOSTRUCTURES USING FDTD SIMULATION AND APPLICATION IN CORE-SHELL TYPE NANOWIRES

4.1   Introduction

In this research simulation tools were used to understand the interaction of light and nanostructures enabling design of devices with desirable optical properties. A number of simulation tools such as effective medium theory, quasi-static calculation, discrete dipole approximation, finite element, and finite difference time domain methods are widely used for studying optical interactions in nanostructures. Among these tools, the finite-difference time-domain (FDTD) method is well recognised as a reliable technique to solve the most challenging photonic design problems by solving Maxwell's equations in two and three dimensions, thus accrediting us to analyse interactions of a wide range of radiation wavelengths with complicated nanostructures (Sullivan, 2013; Taflove & Hagness, 2005).

Lumerical FDTD software provides graphical user interface (GUI) to solve different types of electromagnetic and photonic problems. In addition, it can also obtain frequency domain solution by exploiting Fourier transforms, thus complex Poynting vector and the transmission/reflection of the light as a function of frequency can also be calculated. Therefore, in this chapter, Lumerical FDTD software is used to simulate optical interactions of various nanostructures in the proposed devices.

Finite-difference time-domain (FDTD) algorithm divides space and time into a regular grid and simulates the time evolution of Maxwell's equations (Kunz & Luebbers, 1993; Oskooi et al., 2010). FDTD method can be used to calculate electromagnetic fields in a complex device structure containing nanostructures and multiple patterned thin film layers. Robustness and accuracy of such calculations are

well established for both 2D and 3D device structures. In this work simulations were carried out to understand the optical properties of silver nanostructures and the advantages of integrating silver nanostructures in thin film solar cells. It is crucial to increase light trapping effects in thin film solar cells to enhance light absorption efficiency. Here optical properties of various nanostructures with different sizes and shapes were studied to determine the best combinations for device performance. The following are the topics that will be discussed in this chapter:

i.   Introduction to Lumerical FDTD software tools

ii. 3D simulation set up: Size-dependant tunable plasmonic light scattering properties of silver nanospheres and absorption enhancement in silicon film by addition of silver nanospheres

iii. 2D simulation set up: Long wavelength plasmonic absorption enhancement in silicon using optical lithography compatible core-shell type nanowire.

4.2   Lumerical's FDTD Software Tools

There are numerous tools built in this software. However, not all tools will be used at the same time when running this software. The tools used depend on the application that will be run and also on the data results that are desired. In this section, only basic data that are used in this research were introduced.

4.2.1   Material Data Base

The material database can be accessed through the Materials button on the main toolbar. The Material database allows us to manage (create, modify, delete) the materials used in the simulations.

The default optical material database includes refractive index data for a number of common materials. When creating a new simulation, the default database will be loaded. The default materials cannot be edited directly. However, users can modify one of the default materials by creating a copy of the material, which can then be edited.

Lumerical FDTD also allows to add other data set for any materials that are not include in the material list. The experimental broadband refractive index data of a material as a constant values of *n*, *k* can be imported to the material database. In this case, the experimental material data (the broadband refractive index and extinction coefficient of material as a function of frequency) over the frequency range specified by the excitation source in a simulation are required as shown in Figure 4.1.
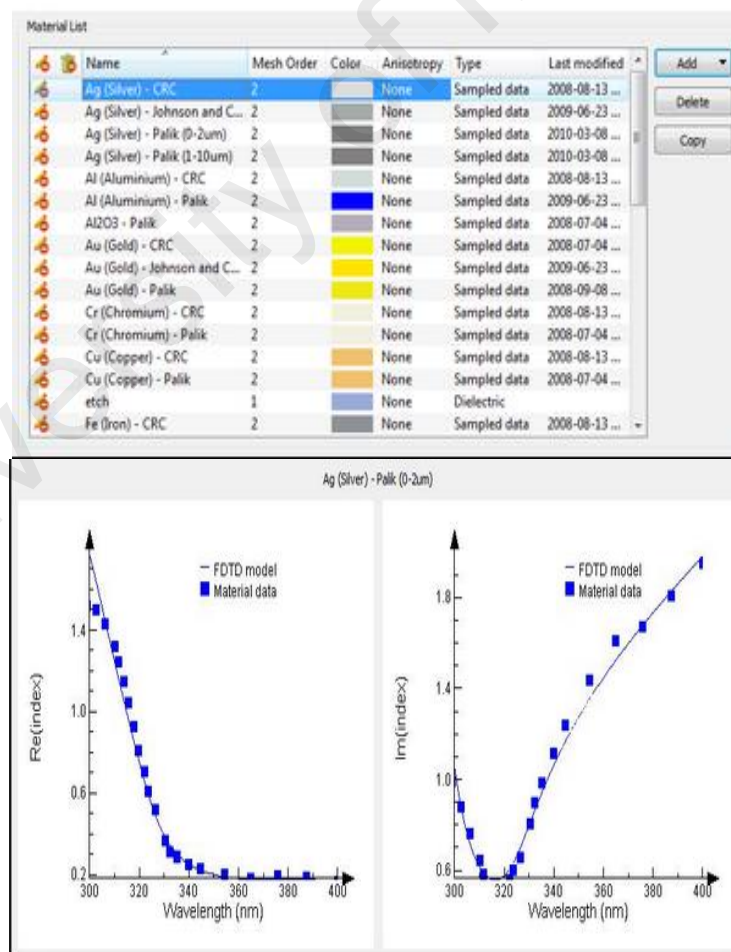
Figure 4.1 FDTD program material database and program material fitting plot respectively.

4.2.2 Simulation Objects

In the photovoltaic device structures, we are often interested in calculating the near field enhancement around the particles, as well as the far field angular distributions. It is also beneficial to explore the absorption/scattering cross sections. The Lumerical FDTD technique provides several objects to set up the simulation. These objects are used to model the physical structure, define the solver region, any sources of light or doping/generation regions as well as monitors to collect data. The following sections provide the detailed descriptions of each simulation object.

4.2.3 Perfectly Match Layer (PML) and Periodic Boundary Condition

In any FDTD field modeling, computation must be confined to a bounded space due to limited computer resources. The field is truncated at an outer boundary that encloses all scatterers. The boundary is said to be ideally absorbing if all waves are out-going without non-physical reflection back into the simulation region. Thus an accurate field distribution may be obtained ideally as if there were no truncation. Clearly, any non-physical reflection will result in artifacts and excessive errors in the obtained field data. Among the different types of absorbing boundary conditions, in this thesis, the attention was focused to FDTD domain with Perfectly Matched Layers (PML), Periodic Boundary Condition (PBC), and Block Boundary Condition (BBC).

i. Perfectly Matched Layer (PML)

A perfectly matched layer (PML) is an absorbing medium that is commonly used to truncate computational grids for simulating Maxwell's equations. It is designed to ensure that interfaces between the PML and adjacent media are reflectionless (Berenger, 1996). The PML method involves adjusting the medium of the simulation in a thin layer around the boundary.

(a)   (b)
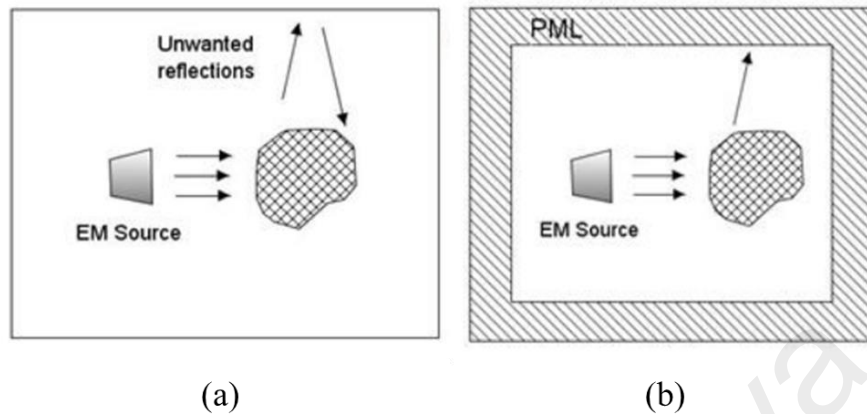
Figure 4.2 Without an absorbing boundary condition, outgoing waves would be reflected back into the problem space. Perfectly Matched Layers are placed adjacently to the edges of the computational region, which truncates outgoing waves.

ii.   Periodic Boundary Condition

Periodic BCs are generally used when both structures and EM fields are periodic and injects radiation in the direction normal to the surface of the structure. It can be chosen in one or more directions so that the simulation is equivalent to an infinite structure composed of the basic computational domain repeated endlessly in one or more dimensions.

To analyse electromagnetic characteristics of a periodic structure, the FDTD grid needs only to be applied to a single unit cell of the structure with boundary condition set as periodic to solve the entire structure. Therefore, the thin-film solar cell with periodic structures can be converted to a single-unit cell of the FDTD calculation model, as shown in Figure 4.3. Where P is the periodicity, PML is the absorbing boundary condition; PBC is the periodic boundary condition. The incident light propagates into the single-unit cell from top to bottom.

60
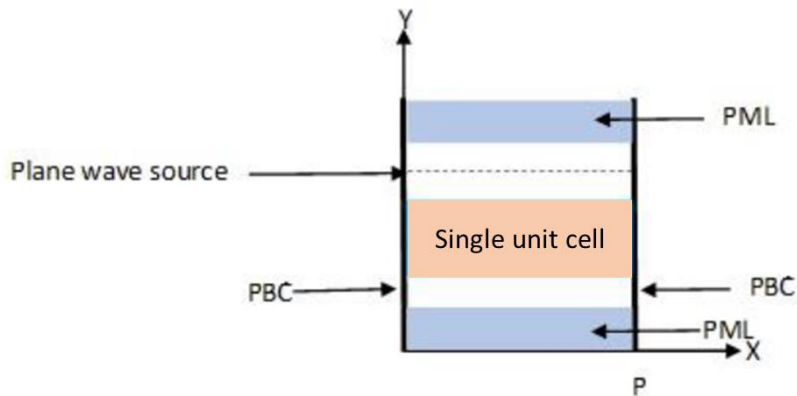
Figure 4.3 The unit cell of FDTD calculation model with a plane wave source and periodic boundary condition.

4.2.4 Radiation Sources

Radiation source defines the electromagnetic energy input for a simulation. There are different types of sources such as point/dipole, Gaussian, plane wave, and total field scattered-field (TFSF). Mode sources are available in the Lumerical FDTD Solutions software. Any radiation source from ray tracing design environment can be imported into the 3D design environment of Lumerical FDTD Solutions software as well.

4.2.5 Meshing

FDTD solution uses a rectangular Cartesian style mesh, as shown in Figure 4.4. It is important to understand that the fundamental simulation quantities (material properties and geometrical information, electric and magnetic fields) are calculated at each mesh point. Using a smaller mesh allows for a more accurate representation of the device, but at a substantial cost of increased memory and simulation time requirement.
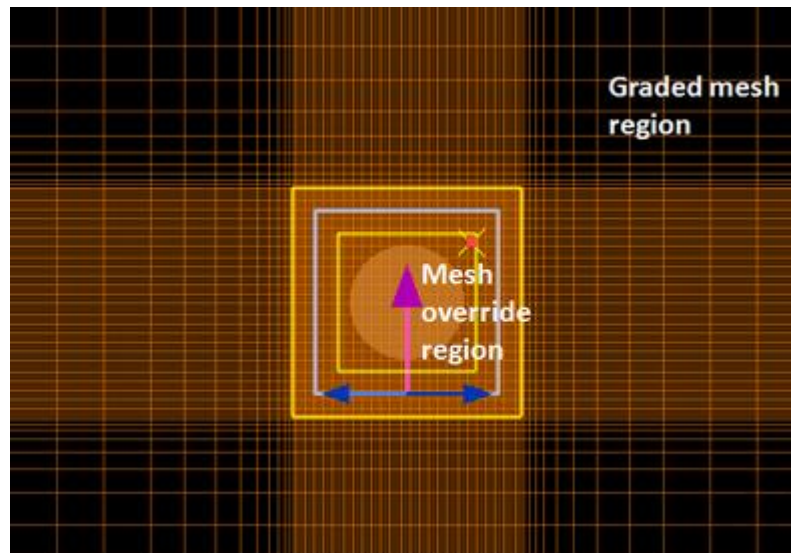
Figure 4.4 FDTD mesh style

Numerical dispersion is an artifact resulting from the discrete spatial sampling of the FDTD mesh. This means that for a coarse mesh, the speed of light on the FDTD mesh may depart slightly from the exact value of the speed of light in the material being simulated. Furthermore, the speed of light becomes slightly anisotropic, where it depends on the direction of propagation of the light relative to the mesh.

4.2.6   Measurement Monitors

Monitors are the measurement units of the simulator with the capability of recording electromagnetic fields at specified directions, locations, or regions. Monitors can generate frequency domain information by Fourier transform. Data such as complex refractive indices, temporal or spatial distribution, and motion pictures of given field components can be gathered using various measurement monitors. Frequency-domain power monitors are used to capture individual field components, pointing vectors, and power flow as a function of frequency.

4.3 Tunable Plasmonic Light Scattering Properties of Size-Dependent Silver Nanosphere

OSCs are a type of thin-film solar cells, which are typically 1-2 μm thick. The major limitation of thin film solar cells is that they do not absorb light as much as thick film solar cells, as most of the sunlight passes through the thin active layer unabsorbed. To make thin film solar cells viable, it is crucial to increase absorption by trapping light on the surface or in the solar cells. Several methods of absorption enhancement have been explored over the past few years. One such method is to scatter light using metal nanoparticles excited at their surface plasmon resonance (Catchpole & Polman, 2008). This allows strong light absorption in a thin film solar cell directly without the relatively thick layer used in normal solar cells.

The aim of exploiting surface plasmons in solar cells is to enhance light absorption in the active layer. The necessity for absorption enhancement in thin-film solar cells is due to the poor electrical properties of their active layer materials that limits the device's thickness, which in turn leads to incomplete light absorption especially near the absorption tails. On the other hand, for crystalline Si solar cells, absorption enhancement is necessary to achieve higher efficiency.

In order to understand how integration of silver nanoparticles enhance light absorption in silicon thin film solar cell, a 3D simulation set up with silver nanosphere on a silicon substrate was created in Lumerical FDTD Solutions software. Initially, the scattering behaviour of individual silver nanospheres with different diameters was studied. Note that 3D simulation set up require more memory compared with 2D simulation. Only simple 3D simulation set ups were created to save computer memory and simulation time. Therefore, low accuracy of plotted results may be expected, but the pattern of the results is something that can be rely on in this study.

4.3.1   Simulation Set Up

In the FDTD software, the sphere-shaped structure was selected and set the material to silver (Ag-palik) from the material database. A total-field scattered-field (TFSF) source surrounding the silver particle was used as the source power in the simulation. There are two types of analysis groups, each of them consists of a box of power monitor; one in the total field region and one in the scattered field region. These analysis groups can be used to calculate the absorption and scattering cross sections, as well as the angular distribution of scattered radiation. In addition, three frequency profile monitors are added in the total field region to calculate the electric field enhancement. The total scattered field source covers a wavelength range from 300 nm to 600 nm. The FDTD simulation region was set to 3D with PML boundary on all sides. The distance from the PML boundary to the simulation objects was at least 1 µm to avoid evanescent coupling. Using this set up, simulations were run for various silver nanosphere sizes from r = 10 nm to r = 100 nm.

4.3.2   Results and Discussion

Figure 4.5 shows the effects of size variations on scattering cross-section silver particles in the air. The resonance peaks are broader and shifts to longer wavelengths with the increase of nanoparticle size. However, these peaks will be red shifted and the smallest particle will have more prominent peak if the particles were run in higher refractive index such as in Si medium (n = 3.5) (Pillai & Green, 2010). Note that the resonance peaks shift to longer wavelengths range with the increase in size, as well as under the influence of a medium with high refractive index. This shift is desirable for Si devices as increase in scattering at longer wavelengths would enable good light trapping close to the bandgap of Si, where Si normally absorbs weakly.
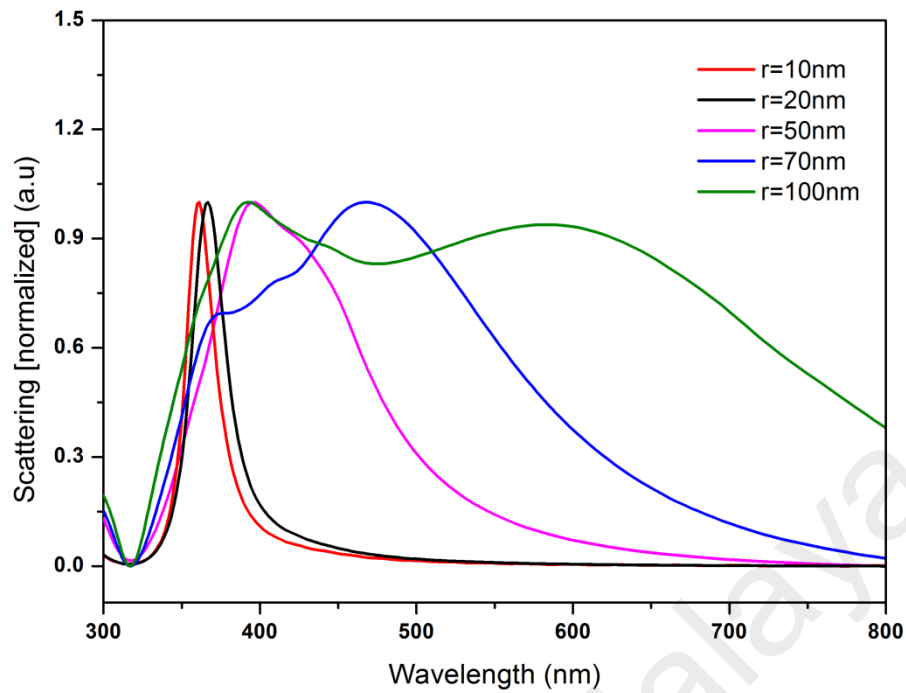
Figure 4.5 Normalized scattering of silver sphere with different particle size

Observation on enhancement in silicon with addition of silver particles was done by adding a silicon layer right below a spherical particle with 100 nm diameter in the similar simulation set up. The result was compared with the one without any silver particles. Figure 4.6 shows the absorption profile of silicon with and without silver particles. It is clearly shown that the particle increases absorption in the silicon substrate by enhanced forward scattering, which arises from surface plasmon resonance.
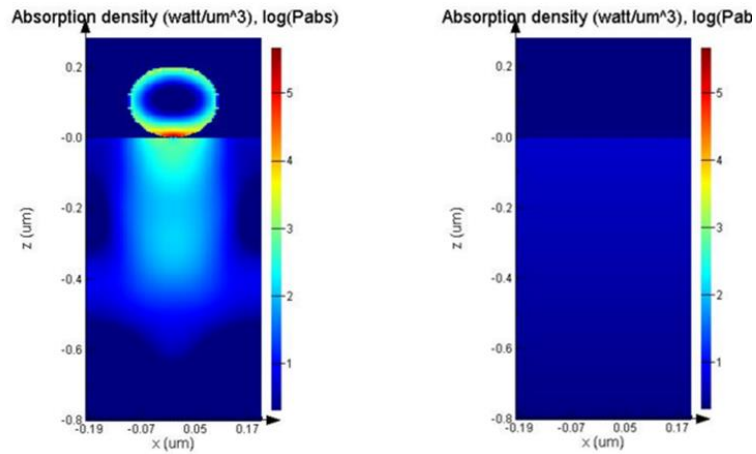
Figure 4.6 Absorption profile of **(a)** plasmonic solar cell and **(b)** bare solar cell

4.3.3   Highlights

FDTD simulations were performed for silver nanoparticles in silicon solar cell structures. Even though the simulation set up was quite simple, the results showed significant patterns of size-dependent tunable light scattering properties of spherical silver nanoparticles. An increase of particle size was observed to cause large red shift of resonance peaks. Addition of silver nanoparticles on top of silicon substrate increased absorption in silicon by forward light scattering. This result showed the usefulness of Lumerical FDTD simulation software, and gives a better idea on planning the experimental part, as it may be possible to increase the efficiency of organic-based solar cells by applying organic material in a similar device structure.

4.4   Long Wavelength Plasmonic Absorption Enhancement in Silicon Using Optical Lithography Compatible Core-Shell Type Nanowires

4.4.1   Introduction

Metal nanoparticles and nanowires can be grown by a number of methods (Fedlheim & Foss, 2001) and applied to solar cells by spin coating. However, spin coating do not allow placement of the nanoparticles with controlled spacing. Aggregation of the nanoparticles causes large change of their plasmonic properties due to coupling and

sparse distribution makes plasmonic enhancement less than optimal. E-beam lithography, Nano Imprint Lithography (NIL), and Substrate Conformal Imprint Lithography (SCIL) can be used for forming regular arrays of sub-100 nm structures. These techniques have yet to meet the low cost of large-scale fabrication requirements of solar cell technologies.

E-beam lithography can be applied to small areas and throughput is low due to the sequential nature of the process. Both NIL and SCIL needs highly clean environment. NIL has stringent surface flatness and roughness requirements. SCIL technique has been developed to relax the surface quality requirements of NIL so that it can become the volume production technique for nanofabrication. Still, SCIL needs high resolution e-beam lithography for making master masks and special equipment for replicating production masks, which have limited lifetime. On the other hand, Deep Ultra Violet Lithography (DUVL) and Laser Interference Lithography (LIL) techniques can be used for large area of high volume fabrication of photonic nanostructures with feature sizes larger than 100 nm (Bläsi et al., 2011; Bogaerts et al., 2002). LIL is particularly suitable for making periodic grating type patterns in square metre scale areas without requiring a mask (Bläsi et al., 2011).

In this work FDTD simulations were performed to explore the feasibility of using DUVL and LIL fabricated nanostructures for plasmonic absorption enhancement in silicon solar cells. Core-shell type rectangular nanowires were chosen for this studies since plasmon resonance of core-shell type structures can be tuned widely by varying core or shell dimensions (Oldenburg et al., 1999) and rectangular shape is compatible with planar thin film fabrication technologies. Silicon and silver were the core and shell materials. Simulation results showed plasmon resonance wavelength of these nanostructures can be tuned from $\lambda=750$ nm to $\lambda=2400$ nm by adjusting dimensional

parameters. These plasmonic structures can improve performance of impurity photovoltaic solar cells by serving the dual purpose of absorption enhancement and effective separation photogenerated carriers.

4.4.2   Simulation Set Up

Simulations were performed in 2D using Lumerical FDTD Solutions. Nanowires significantly longer than the wavelength of light can be considered infinitely long in the context of light scattering. The nanowires fabricated by DUVL or LIL techniques can be much longer than the optical wavelengths near the bandgap of silicon. Hence, these nanowires can be assumed infinitely long and cross-sectional 2D simulation can be applied to study their localized plasmon properties. Silver and silicon models were based on data from Palik (Palik, 2012). Staircase approximation was applied at the material boundaries. Mesh size was at least 10 times smaller than the smallest feature present in the simulation. The nanowires were positioned at the centre of an 800×800 nm simulation cell with Perfectly Matched Layer (PML) boundary. A 300 nm of glass substrate and a 500 nm of silicon layer were included in the simulation cell (Figure 4.7). The same parameters of the TFSF source were used in all related simulations so that power absorption data from different simulation runs could be compared. Spatial distribution of optical power absorption was recorded using Lumerical's built-in advanced power monitor for better accuracy.

According to Lumerical documentation, electric field component values are interpolated to the centre of Yee cells for power absorption calculations. Advanced algorithms are used for more accurate estimation of electric field values at metal-non-metal boundaries. Power absorption was recorded in a (200×150) nm box-shaped region with the nanowire at the centre for all simulations with the nanowire widths smaller than 150 nm. The size of the power absorption recording box was (300×150) nm for wider

nanowires. In this geometry, power absorption due to enhanced local electric fields of the nanowire can be assumed to be much larger than absorption due to scattered and incident fields. Plasmon resonance causes an increase in electric field intensities in the metal of the nanowire and in the semiconductor near the nanowire surface. Power absorption at a wavelength 'ω' in a Yee cell with refractive index 'n(x,y, ω)' and electric field intensity 'E(x,y, ω)' was calculated using the formula:

$$P_{abs} (\omega) = 0.5* \omega*|E(x,y, \omega)|^2*imag(n(x,y, \omega)) \qquad (4.1)$$

Summation of absorption from all Yee cells in the simulation area has given the total absorption at a particular wavelength. This process is repeated for all wavelengths. Hence, plasmon resonance gives rise to peaks in the power absorption vs. wavelength plots. A computer program was used to determine whether a Yee cell is located in silicon or silver. Thus, power absorption in silicon and silver regions were determined separately.
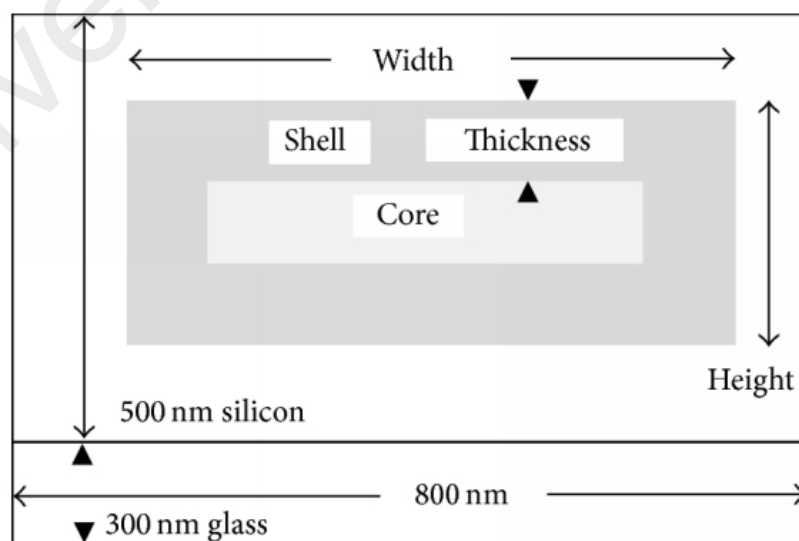
Figure 4.7 Sketched diagram of core shell nanowire in simulation set up

4.4.3 Structure of the Nanowires and Suggested Deposition Process

The dimensional parameters of the nanowire such as width, height, and shell thickness are also shown in Figure 4.8. The figure suggested fabrication sequence and structure of a half-shell nanowire. Photolithography process can be used experimentally for defining the width and height of the nanowires. A metallization method with good step coverage such as sputtering or e-beam evaporation with sample rotation should be used for depositing the shell layer, which is explained in the section below. For half-shell nanowire fabrication, the next step is lift-off process followed by silicon deposition to embed the nanowires in silicon. For core-shell nanowires, silicon deposition should be done next after forming the core. A directional deposition method such as e-beam evaporation without sample rotation should be used for silicon deposition so that metal on the sidewalls do not get coated with the silicon. Residual silicon from the sidewalls can be removed by mild etching. Then deposition of the top metal layer and lift off would complete the core-shell nanowire. These fabrication steps and structures are compatible with polycrystalline silicon solar cell development using e-beam evaporation (Kunz et al., 2009).
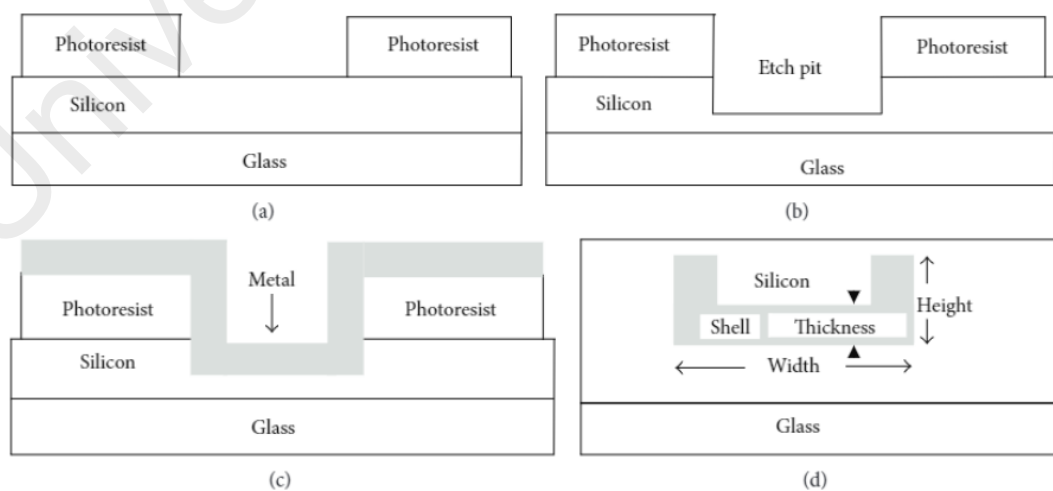
Figure 4.8 Suggested fabrication sequence for half-shell nanowires **(a)** lithography **(b)** etching **(c)** metal deposition **(d)** a half-shell nanowire after lift-off and silicon deposition

4.4.4 Plasmonic Enhancement Properties of Core-shell and Half-shell Silver Nanowires

Figure 4.9 shows the absorption in silicon and silver for the core-shell and half-shell nanowires. The core material for the core-shell nanowire is silicon and shell material for both types of nanowires is silver. By keeping the shell thickness constant at 10 nm, the widths and heights of the nanowires were adjusted to bring their plasmon resonance wavelengths close to $\lambda = 950$ nm to simplify absorption comparison, since plasmon resonance wavelength, enhanced electric field distribution, and absorption vary with wavelength-dependent refractive indices of the metal and surrounding semiconductor.
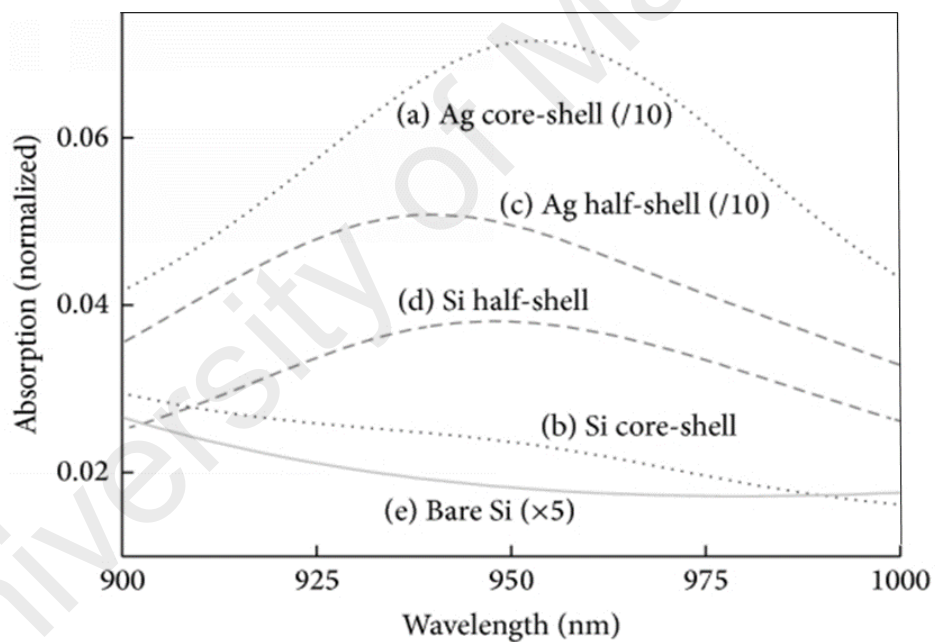
Figure 4.9 Power absorption spectra in silver and silicon for core-shell and half-shell silver nanowires.

Plasmon resonance was approximately at $\lambda = 940$ nm for a core-shell nanowire with 120 nm width and 40 nm height. A half-shell nanowire with 120 nm width and 25 nm height showed plasmon resonance at nearly the same wavelength. Traces (a) and (c)

showed absorption in silicon for the core-shell and half-shell nanowires. Traces (b) and (d) showed absorption in silver downscaled by five times for the same nanowires. Trace (e) showed absorption in bare silicon scaled up by a factor 8 without any nanowire in the simulation area. The data were scaled for improving graphical representation. Comparing the traces of (a), (c), and (e) at $\lambda = 940$ nm, absorption enhancement in silicon for the core-shell and half-shell nanowires was 13 and 18 times respectively. These enhancements are roughly three times larger than enhancement due to a solid spherical silver nanoparticle at 870 nm (Spinelli & Polman, 2012).
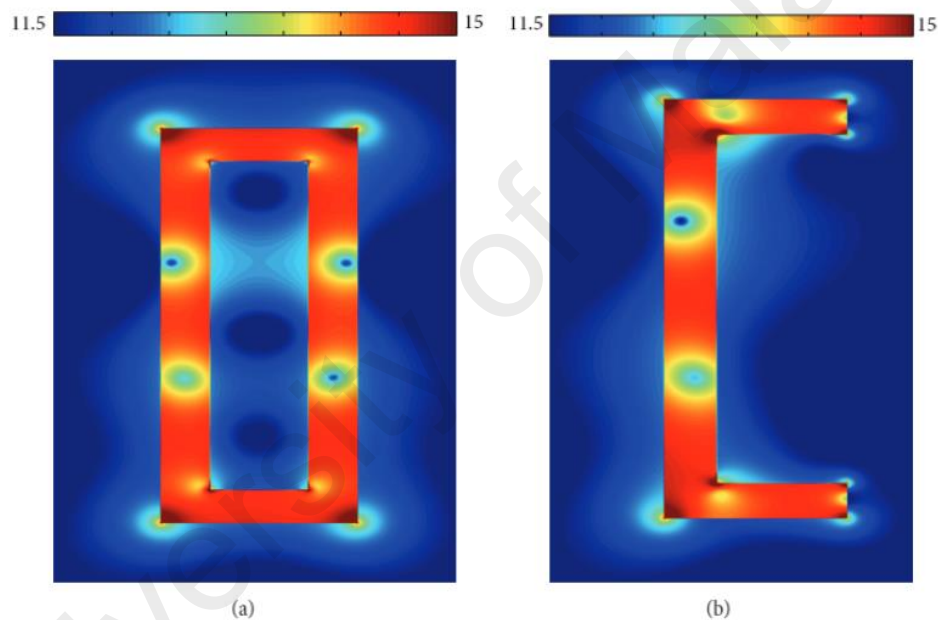
Figure 4.10 Spatial map of power absorption in logarithmic scale for a **(a)** core-shell nanowire (120 x 40) at λ=951nm **(b)** half-shell nanowire (120 x 35) at λ= 946nm. Shell thickness was 10nm.

Figure 4.10 shows spatial distribution of optical power absorption for a core-shell nanowire in logarithmic colour scale. Power absorption was calculated using Equation 4.1. Strong absorption in the core region can be observed in this figure. In commonly used solar cell structures such as *p-i-n* or *p-n* type devices, effective extraction of the

photo-generated carriers from the core region would require additional device design and fabrication steps. Hence, the half-shell nanowire structures were investigated for further understanding. Fortunately, absorption enhancement due to the half-shell nanowire was even larger than the core-shell nanowire. Optical power absorption map for a half-shell nanowire is shown in Figure 4.10. From this figure, it is apparent that photo-generated carriers can drift towards collection contacts in conventional solar cell structures without encountering obstacle. Comparison of the traces (c) and (d) in Figure 4.9 shows that even the enhanced absorption in silicon was less than 10% of the Ohmic absorption loss in the silver shell of the half-shell nanowires. Similar ratio was reported for a solid spherical silver nanoparticle embedded in silicon (Aden & Kerker, 1951). This is due to very low absorption coefficient of silicon in the near bandgap region. As discussed below, the suggested half-shell nanowires can potentially reduce this unfavourable ratio by serving the dual purpose of plasmonic enhancement of impurity optical absorption and extraction of one type of the photo-generated carriers.

Since spherical silver nanoparticles must be isolated from each other in a solar cell structure to preserve their individual plasmonic properties, they cannot play effective role in carrier transport. According to the material models used in this simulations, imaginary component of refractive index of silver was 6,200 times larger than silicon at $\lambda = 940$ nm.

However, absorption in silver was only five times larger. Hence, plasmonically enhanced electric field distribution is very effective in increasing absorption in the silicon region. Formation of narrow impurity photovoltaic zones around the nanowires may enable better utilization of such field distribution for increasing optical absorption. In impurity photovoltaic effect, electron-hole pairs are generated by sub-bandgap photons through transitions involving deep level impurities.

Recombination loss in the impurity zone prevents effective extraction of the generated carriers. The proposed structure can resolve this dilemma by serving the dual purpose of plasmonic enhancement and carrier collection. The silver shell can form Ohmic contact to n-type silicon and sweep away electrons fast. Reduction of the impurity zone thickness and immediate collection of one type of the photogenerated carriers would decrease recombination loss in the impurity zone. Since the real parts of refractive index of amorphous silicon (a-Si:H) and crystalline silicon are comparable, it can be speculate that nanowires with similar dimensions embedded in a-Si:H would show plasmon resonance at nearly the same wavelengths. The poorly absorbing photons on the upper side of crystalline silicon bandgap are sub-bandgap photons for a-Si:H due to larger bandgap of a-Si:H. Hence, these nanowires can be used for enhancing impurity photovoltaic effect in a-Si:H as well. Plasmonic enhancement of impurity photovoltaic effect in a-Si:H has been reported recently (Lükermann et al., 2012).

4.4.5 Plasmon Resonance Tuning of Half-shell Nanowires

Solar radiation has significant power of density up to approximately $\lambda = 2,500$ nm, which can be harvested by impurity photovoltaic effect discussed above. Hence, tunability of plasmon resonance of the half-shell nanowires was investigated for absorption enhancement at the longer wavelengths of solar spectra. Keeping the shell thickness constant at 10 nm, widths and heights of the nanowires were varied to study their effect on plasmon resonance. Optical power absorption spectra were recorded for the bandwidth $\lambda = 750$ nm to $\lambda = 1,850$ nm. Figure 4.10 shows total power (silicon +silver) absorption spectra of half-shell nanowires for the heights of 20, 40, 60, and 80 nm, while the width of these nanowires was 120 nm. Absorption spectrum for a nanowire with 140 nm width and 60 nm height is also shown in this figure to demonstrate the effect of width variation.
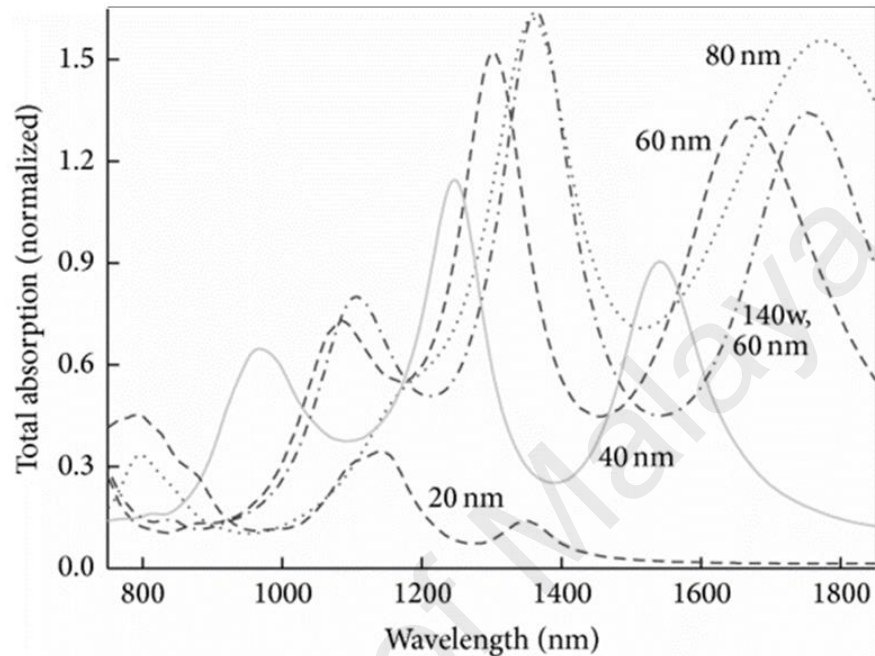
Figure 4.11 Total (silicon + silver) power absorption spectra for half-shell nanowire with heights from 20 to 80 nm. Width of this nanowire was 120 nm. The trace marks of (140 w, 60 nm) show the spectrum for a (140 x 60) nanowire. Power absorption was normalized with respect to source power.

Most of the absorption took place in silver at longer wavelengths. Absorption in silicon and silver were not separated since the purpose of this plot was to show tunability of plasmon resonance. Three plasmon resonance peaks could be observed in Figure 4.11 for each nanowire. These peaks shift to longer wavelengths with increase of nanowire height. It is possible to tune plasmon resonance between $\lambda = 750$ nm to $\lambda = 1850$ nm by choosing an appropriate nanowire height from 20 nm to 80 nm, keeping the nanowire width fixed at 120 nm.

The increase of nanowire width also caused a shift of plasmon resonance peaks to longer wavelengths, as can be seen by comparing the absorption traces for the (120×60) nm and (140×60) nm nanowires in Figure 4.11. The longest plasmon resonance peak for a (250×60) nm nanowire was located at $\lambda = 2,400$ nm. This nanowire is not shown in Figure 4.11 since simulation bandwidth and power absorption recording box size for this nanowire were different from the other nanowires. Simulation bandwidth was from $\lambda = 1,000$ nm to $\lambda = 2,500$ nm for this nanowire due to validity limit of silver material model from $\lambda = 1$ μm to 10 μm. Silver model used in the previous simulations was valid up to $\lambda = 2$ μm. Hence, plasmon resonance of half-shell nanowires can be tuned in the $\lambda = 750$ nm to $\lambda = 2,400$ nm range by adjusting the width and height dimensions. These nanowires may enhance impurity photovoltaic effect over the entire long wavelength range of solar radiation.

4.4.6 Highlights

Numerical investigations were performed on the possibility of fabricating plasmonic absorption enhancement structures for silicon solar cells using mass fabrication capable optical lithography techniques. The simulation results indicated that reliable volume production capability of optical lithography techniques can be utilized for fabricating nanowires with plasmon resonance tunability from $\lambda = 750$ nm to $\lambda = 2,400$ nm covering the entire long wavelength range of solar radiation. Absorption enhancement due to these nanowires was larger than reported absorption enhancement due to solid spherical silver nanoparticles near silicon bandgap. These nanowires may prove to be distinctly advantageous in boosting performance of impurity photovoltaic solar cells by their ability to serve the dual purpose of plasmonic enhancement and extraction of one of the types of the photo-generated carriers.

CHAPTER 5: TUNABLITY OF SURFACE PLASMON OVER DIMENSION DEPENDANCE

5.1   Introduction

This chapter presents the study of Ag NPs properties via different deposition processes. The first two sections in this chapter will discuss the effect of silver particles shape towards plasmonic behaviour. The dendritic and flower-like silver structure were formed via two different preparation process of electrochemical and template method respectively. The following section discusses the plasmonic dependence in size distribution and particle separation that also includes several deposition processes such as electrophoretic deposition, spin coating, and e-beam evaporation. Finally, the best preparation method for Ag NPs that has optimum plasmonic behaviour was favoured to implement the fabrication of organic optoelectronic device and will be further discussed in the next chapter.

5.2   Study of Electrochemically Deposited Silver Dendritic Structure (Ag NDs)

In this section, plasmonic behaviour of dendritic silver structure prepared by chemical method has been studied. The UV-Vis result shows the optical properties of this Ag NDs structure are quite promising. This result is important to study the enhancement made in active photovoltaic layer, which will be further discussed in Chapter 6.

5.2.1   Experimental Procedures

The utilized electrochemical deposition technique involved an indium tin oxide (ITO) electrode as the working electrode, and platinum foil of 2 cm^2 surface area performing as a counter electrode. A solution containing 40 mM Ag (NH$_3$)$_2$OH was prepared by adding ammonia (1 wt. %) to a 50 mM silver nitrate solution. Distilled water was added at a volume ratio of 1:12 (Ag (NH$_3$)$_2$OH:water) in the cyclic

voltammetry process. Scan rates of 1 and 10 mVs^{-1} were invoked by the application of two different potentials, and the eventual Ag NDs mass residing on the ITO electrode was washed to eliminate any impurities and then dried at 50 ºC.

5.2.2   Results and Discussion

5.2.2.1 Surface Configuration Study

Figure 5.1 shows FESEM images of two samples; (a) and (b) these are Ag NDs prepared at 1 mVs^{-1} at different magnification, where (c) and (d) are Ag NDs prepared at 10 mVs^{-1} scan rate in two different magnification.
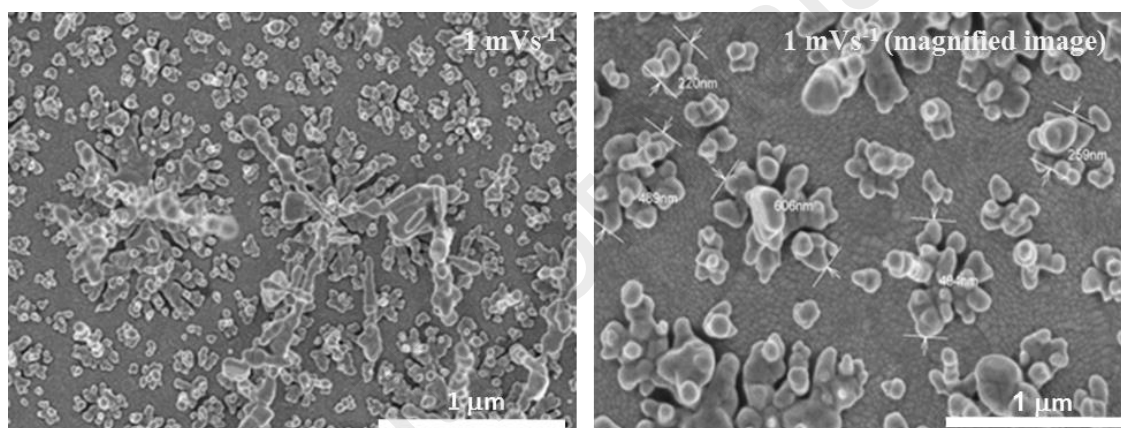
(a)

Figure 5.1 FESEM images of Ag NDs **(a)** prepared at 1 mVs^{-1} scan rate and **(b)** morphology of Ag NDs at scan rate of 10 mVs^{-1}
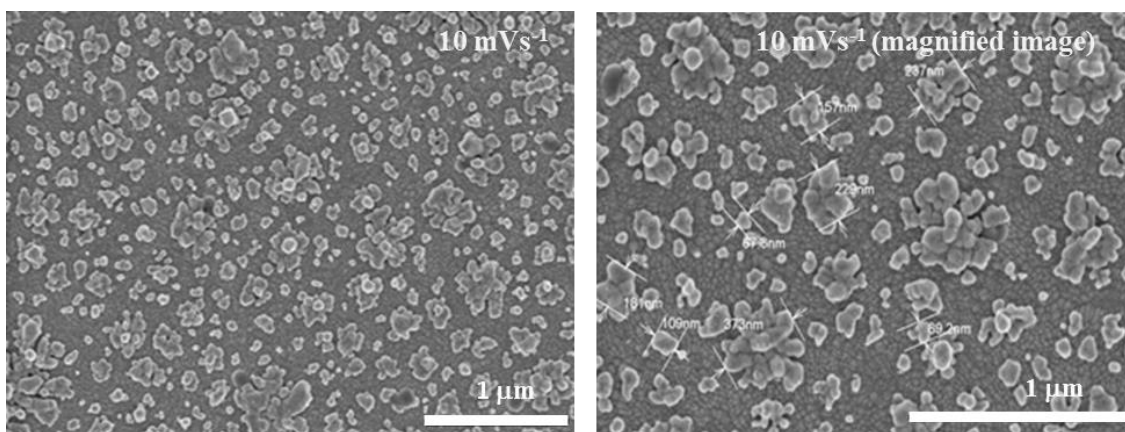
(b)

Figure 5.1 (Continued) FESEM images of Ag NDs (a) prepared at 1 mVs-1 scan
rate and (b) morphology of Ag NDs at scan rate of 10 mVs-1

In Figure 5.1, the morphologies of Ag NDs using different scan rates show dendritic
shape of Ag nanoparticles. Only two types of scan rates, which has large different
values were used to study the obvious different response when the scan rate were
increased. Size of Ag NDs prepared at 10 mVs^{-1} scan rate is smaller compared with the
morphology obtained at 1 mVs^{-1} scan rate with inter-particles distance of the Ag NDs
since the current density could be increased because of increasing scan rate for the
diffusion controlled process (Bond, 2002). The nucleation number can be promoted in
the faster scan rates, where the sufficient time for electro-crystallization growth is not
provided. Therefore, the particle size and electro-crystallized morphology changed
while the variety scan rates were applied (Ebadi et al., 2011). Moreover, morphology of
Ag NDs prepared at lower scan rates has inhomogeneous structure that appeared bigger
than the one with a higher scan rate. Size distribution in Figure 5.1 (a) and (b) has the
ranges from ~50 nm to ~600 nm size and the larger flower-like showed the size was
raised up to ~2 µm. In contrast, the size distribution for Ag NDs at a higher scan rate of
10 mVs^{-1} (Figures 5.1 (b) and (c)) differs from ~50 nm to ~300 nm. The smallest

79

structures are the simplest nanoparticle seeds and the largest ones are the flowers, these being clusters of nanoparticles, forming bigger structures. The annealing process contributed to the agglomerations of Ag NDs. The magnification images at both conditions revealed that the NDs structures size and inter-particles spacing are consistent.

Energy dispersive X-ray spectroscopy (EDX) was carried out to both samples with different scan rate in order to verify the elemental composition and their distribution. Figures 5.2 (a) and (b) are the EDX spectra obtained for both samples. Both EDX spectra showed a high peak of Ag detected from the samples. The comparatively small existence of oxygen for both samples seen in the data may due to slight oxidation occurring on the surface of Ag samples. However, the oxidation will not harm the plasmonics behaviour of the Ag structures (Kuzma et al., 2012).
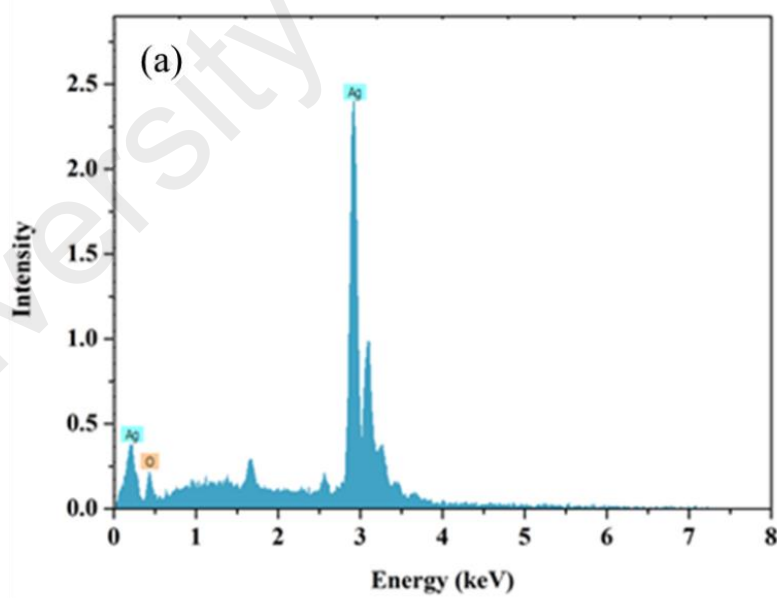
Figure 5.2 EDX results for **(a)** Ag NDs at 1 mVs^{-1} scan rate and **(b)** Ag NDs at scan rate of 10 mVs^{-1}
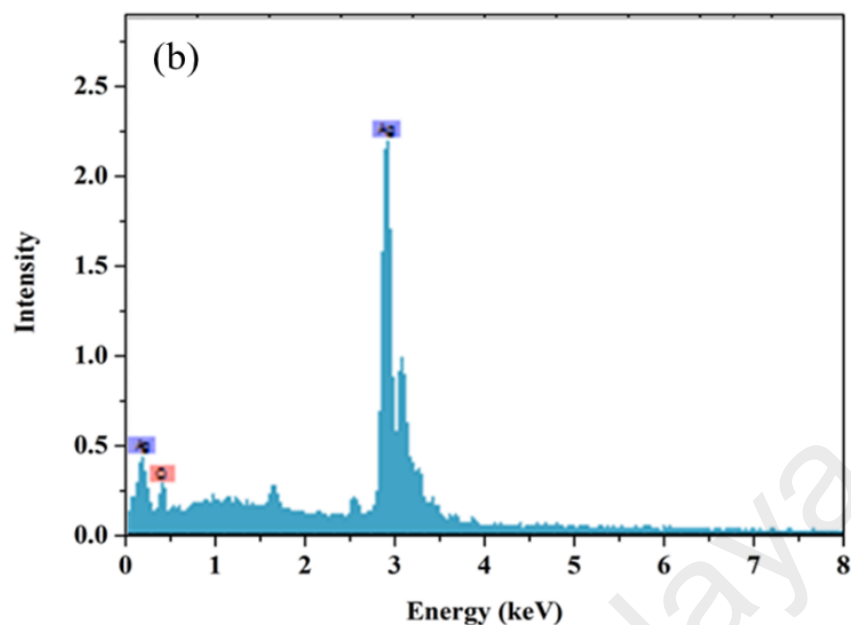
Figure 5.2 (continued) EDX results for (a) Ag NDs at 1 mVs-1 scan rate and (b) Ag NDs at scan rate of 10 mVs-1

5.2.2.2 UV/VIS Absorption Spectra

Figure 5.3 shows the absorption spectra for both samples where black line is Ag NDs prepared at 10 mVs^{-1} scan rate and red line is absorption spectra of Ag NDs film prepared at 1 mVs^{-1} scan rate. Both absorption spectra exhibit similar absorption behaviour with peaks at 370 nm and at 525 nm. As there were various sizes and unique shapes of the Ag NDs plus the inter-particle distances are quiet close, some electromagnetic coupling between two or more adjacent particles might happen and affect the resonance frequency leading to absorbance behaviour in a sample of 10 mVs^{-1} (Malynych & Chumanov, 2003; Sherry et al., 2005). Meanwhile, for sample of 1 mVs^{-1}, only a small resonance occurred at those wavelength, as shown by the broad peak of the spectra. Morphology, particle size, and inter-particle spacing considerably affected the optical property. Light scattering by this mechanism increases with decreasing particle with scattering efficiency being extremely dependent upon the particle size distribution (Kiomarsipour et al., 2013).
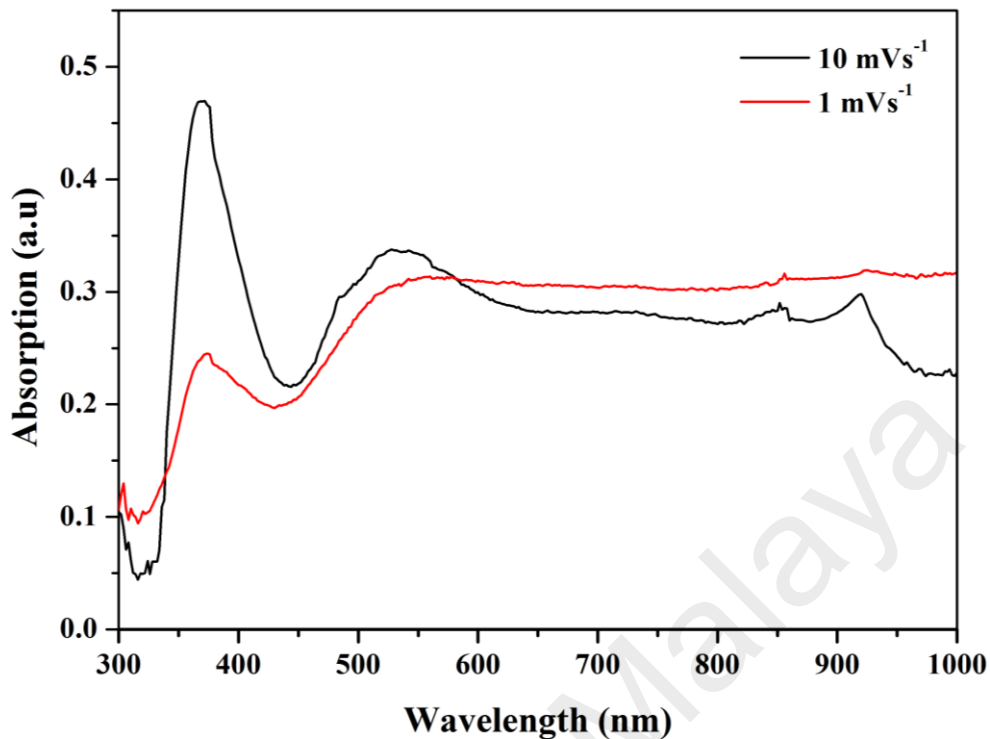
Figure 5.3 Absorption spectra of Ag NDs indicate 10 mVs^{-1} scan rate and 1 mVs^{-1} scan rate.

5.3 Study of Silver flower-like Structure Deposited Using Template Method

This section presents formation of flower-like shape of silver particles using a template method to study their plasmonic behaviour. Silver particles were deposited onto the alumina template using e-beam evaporation and annealed to make the silver grow through the template hole.

5.3.1 Experimental Procedure

Firstly, a thin layer of Ag was deposited on ITO-coated glass substrates using electron beam evaporation techniques in a high vacuum chamber of 2 x 10^{-5} mbar. Then, the sample was annealed for two hours at 250°C. In this process, Ag spherical particles were produced in a nano-size (10-20 nm) and they were distributed uniformly on the ITO substrate.

Anodic aluminum oxide (AAO) template with nominal pore diameter of 20 nm and thickness of 60 μm was purchased from Whatman Anodisc Inorganic Membrane (Sigma-Aldrich, St. Louis, MO, USA). Notably, the commercial template (Whatman) exhibits the branched structure throughout the template, which may support the preceding observation. The templates were cleaned prior to use by sonication in water and acetone for 15 minutes each. The deposition process was carried out by using electron beam evaporation to obtain structures of Ag that fit the mould of the alumina template. The samples were then annealed at 250 °C for two hours in an oven so that the micro-flowers will further grow within the template pores. After the annealing process was done and the samples were cooled down to ambient temperature, an adhered copper tape was carefully stuck on the top surface of the template. Then, the copper tape was carefully peeled off from the glass substrates leaving the samples turned upside down on the copper tape (see Figure 5.4 for clear figuration of the process). After that, the alumina template was dissolved in a 3M sodium hydroxide (NaOH) solution and rinsed thoroughly with deionised water until the pH of the solution became neutral. These micro-flowers were characterised using field emission scanning electron microscopy (FESEM) (Quanta FEI 450), UV/VIS spectroscopy (Perkin Elmer), and photoluminescence spectroscopy (RENISHAW).
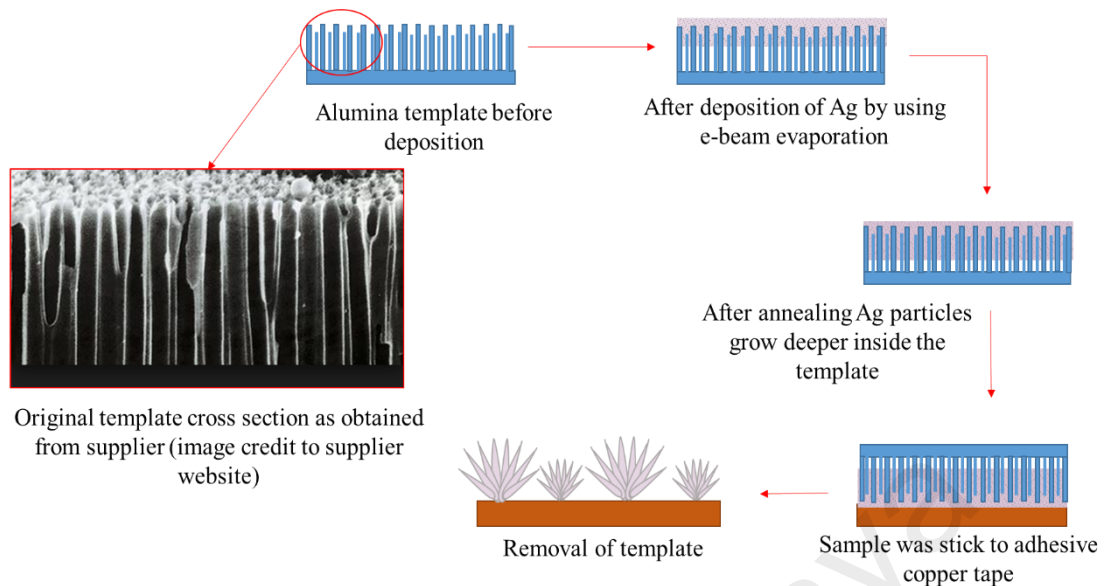
Figure 5.4 Schematic diagram of the fabrication of Ag micro-flowers

5.3.2 Results and Discussion

5.3.2.1 Surface Configuration Study

Figure 5.5 shows the FESEM image of Ag micro-flowers. The smallest micro-flower measured at ~ 60 µm with a distance arrangement of ~ 60 µm from centre-to-centre of B and C, ~ 110 µm centre-to-centre from C and D, and ~130 µm from B to D. This figure also illustrates that the Ag flower-like structure had a large size and spacing of micro-range unit. Figure 5.5 (b) shows a higher magnification of an Ag micro-flower from Figure 5.5 (a). This single flower structure consisted of tens of spikes. This structure appeared to be almost the same as it was proposed earlier in the experimental method. However, the structures are not homogeneously distributed on the copper tape, which may cause a few of the structure not being able to stick on the copper tape properly. Note that the purpose to stick the structure onto the surface of the copper tape is for it to be able to be seen in the FESEM imaging.
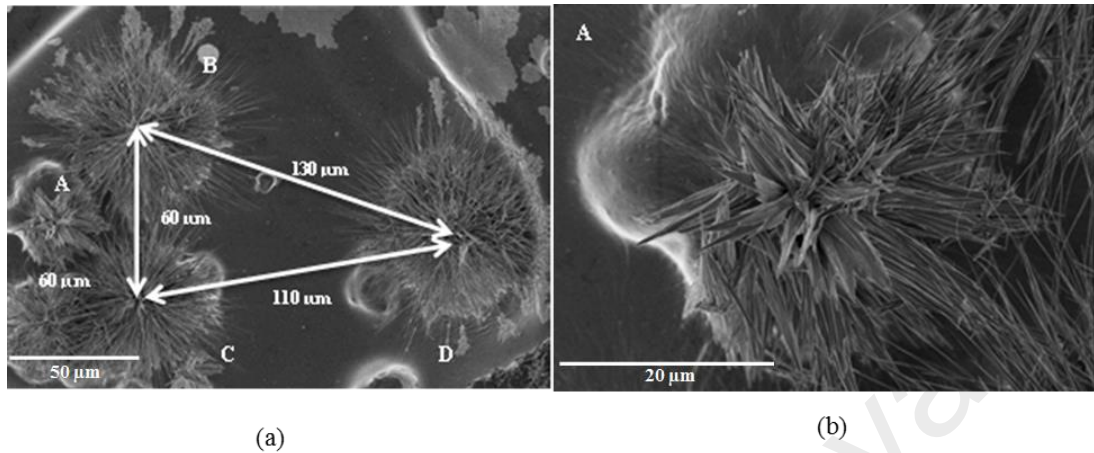
Figure 5.5 FESEM images of **(a)** several clusters of Ag micro-flowers at the selected area with sizes and spacing stated **(b)** a cluster from area A in (a) at a higher magnification.

5.3.2.2 UV/VIS Absorption Spectra

The result of UV-Vis absorption spectra between Ag micro-flowers is presented in Figure 5.6. Note that the UV/VIS was done before sticking the structure on the copper tape and the data obtained was after subtracting the value for the template. It shows that Ag film has the main absorption at a low wavelength (< 500 nm). The Ag micro-flowers had a single broad peak maximum at 440 nm and gradually decreased with the longer wavelengths, which is contrarily compared with previously mentioned of Ag dendritic structure that have double peaks of prominent and broad peak at 370 nm and 525 nm, respectively. It is clearly seen that the absorption peak of Ag micro-flowers occurred at a wavelength range where the absorption of Ag NDs dropped. This occurrence might be caused by a huge difference in structure shape and size between Ag NDs and Ag micro-flowers (Qadir et al., 2014). Ag NDs have been reported to have a better surface

plasmon behaviour compared with Ag micro-flowers, as it has a more prominent absorption peak (Kumar, 2013).
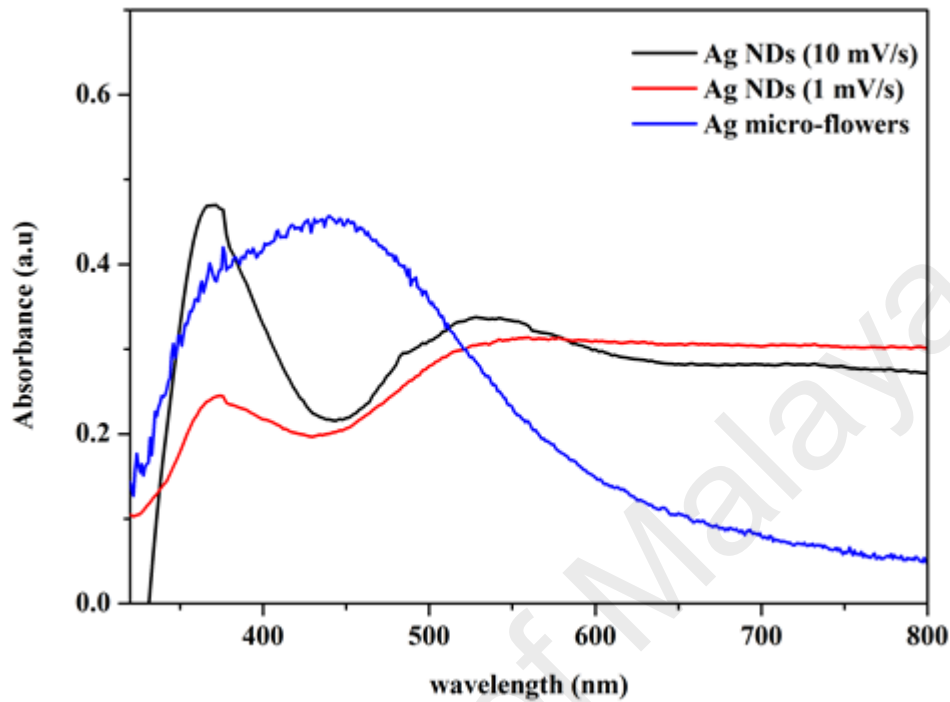
Figure 5.6 UV-Vis absorption spectra of Ag micro-flowers compared with previously studied Ag NDs

5.3.3 Highlights

In this work, a little modification of depositing silver nanostructure via e-beam evaporation technique has been done by adding the alumina template to the ITO substrate. Annealing process of the samples made the deposited silver particles grew deeper into the template holes. Even though the flower structure was in micro size, the spikes of the flower were in nano size to accommodate the holes of the template. The resultant micro-flower shape displayed quite a strong absorption spectra compared with dendritic shape of silver. Even though it has weaker SPR behaviour, it is considerable to study its potential to be applied in several applications. However, in order to study its potential in organic photovoltaic, the preparation method of this silver shape must be optimized so that the final structures are lying on the ITO substrates.

5.4 Effects of Particles Size Distribution and Inter-particles Spacing

The effects of size distribution and inter-particles spacing of silver nano-particles towards its optical behaviour has been discussed. Three different methods have been employed to obtain three different distributions of silver particles, which include closely packed distribution, far-off particles, and particles in close proximity. This section will elaborate the details of the experiment and the result outcome.

5.4.1 Experimental Procedure

a) <u>Closely Packed Distribution by Electrophoretic Depositions (EPD) Technique</u>

In this study, the experimental set up for EPD technique was self-built by using two small ITO slides as anode and cathode. The ITO-coated glass with sheet resistance of about 10 ohm was purchased from Sanyo, Japan. This ITO will be used as substrate through all the depositing process in the research. The electrodes were connected to a 5 V voltage power supply with crocodile clip and were dipped into an aqueous buffer solution that contained silver nanoparticles ink with size ranging from 20 to 80 nm. The experimental set up is as shown in Figure 5.7 below and the Ag NPs will be deposited on the negative electrode of the conductive ITO surface.
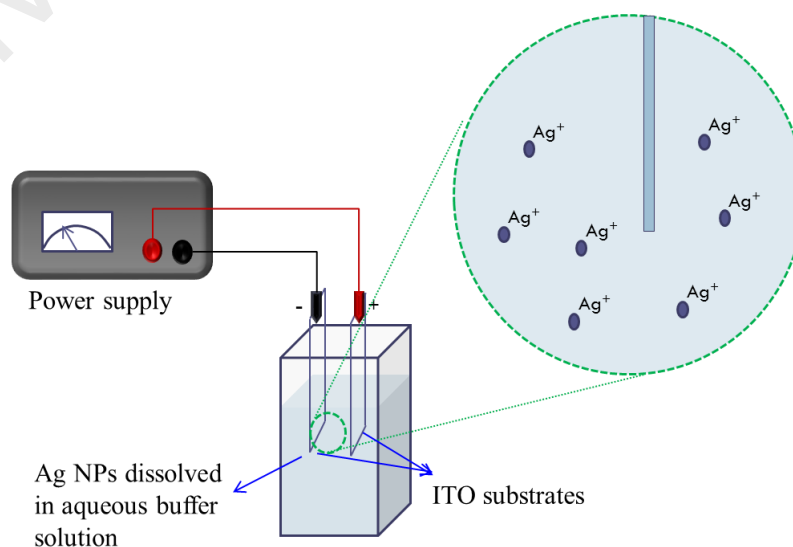
Figure 5.7 Schematic diagram of electrophoretic deposition (EPD) technique

For this technique, a spin coater (WS-650MZ-23NPP) has been used to hold and spin the ITO substrate during the formation of far-off distributed Ag particles. 2 ml silver nanoparticles ink (purchased from Sigma Aldrich with average size <150nm) was dispensed onto the ITO coated glass substrate during the spinning process. The desired thickness (< 20 nm) of thin film containing silver nanoparticles was formed by 6,000 rpm spinning rate for 1 minute. Figure 5.8 shows the diagram of spin coating process of Ag NPs. The samples were heated at about 50 °C to remove excessive solution residue.
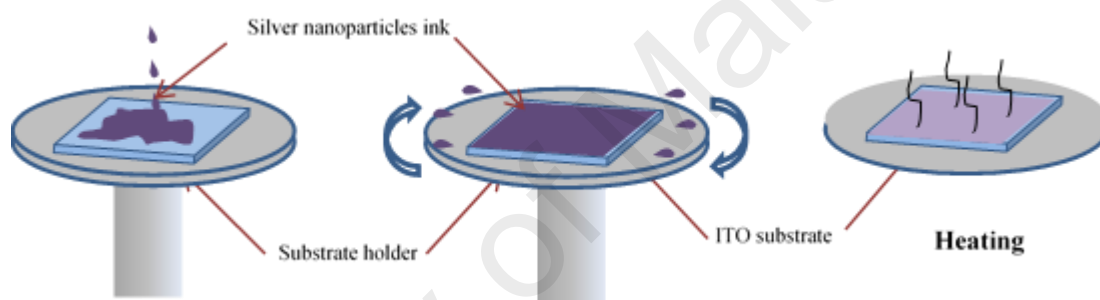
Figure 5.8 Schematic diagram of spin-coat technique

c) Close Proximity and Uniform Size Distribution by E-beam Evaporation

Electron beam evaporator (KCMC assembled model EB43-T) was used in the third technique for the preparation of Ag NPs and it is illustrated earlier in Figure 3.2 of Chapter 3. ITO substrate was placed on top of the chamber with the ITO surface facing downwards towards the silver pellet target. The chamber was pumped down until the pressure reached ~ 1 x 10^{-6} mbar. When the desired pressure was achieved, the deposition was initiated at 4 kV and 25 mA. At this stage, the target anode of the silver pellet was bombarded by an electron beam from the charged tungsten filament. This process led to the change of the solid silver pellet target into a gaseous phase and coating the substrate with a thin layer of silver. The deposition took place for 15

seconds under low evaporation rate to control the formation of a very thin Ag layer with thickness below than 10 nm. After 15 s, the shutter was closed to stop the deposition of silver onto ITO substrate. The sample was then annealed at 250 °C for two hours in the oven for the formation of Ag nanoparticles from Ag thin layer.

5.4.2 Results and Discussion

5.4.2.1 Surface Configuration Study

In order to get the best deposition technique to produce silver nanoparticles orientation that could create the plasmonic effect, three different approaches were used namely EPD, spin coating, and e-beam evaporation techniques. After each deposition process, FESEM measurement was conducted to observe the configuration of nanoparticles thin film. Figure 5.9 shows the FESEM image of the silver nanoparticles thin film prepared using EPD technique. Figure 5.10 and Figure 5.11 illustrate the FESEM surface morphology of the silver nanoparticles prepared via spin coat and e-beam evaporation technique respectively. It is shown that all three methods can produce spherical or near spherical silver particles. It is suggested that the formation of spherical shape is mainly attributed to the particle agglomeration during the annealing process (Lv et al., 2007).

In Figure 5.13, it is shown that the silver nanoparticles are formed in a stacked particles configuration with non-uniform particle size (which restricts the distribution graph to be plotted). As calculated using provided scale given from FESEM image, the particle size formed are in the range of ~ 50 nm to 500 nm, which may be due to the stacked layer arrangement. In terms of inter-particle spacing, it could be seen that the silver nanoparticles from EPD technique are closely packed and stacked on each other. In comparison, via spin coat and e-beam evaporation techniques, morphology of single layer particles together with the inter-particle distance distribution was managed to be

obtained as depicted in Figure 5.10 (b) and Figure 5.11 (b). It is observed that silver nanoparticles-prepared spin coat technique shows non-uniformity and large inter-particle spacing, which is in the range of 100 nm to 1 μm. Via e-beam evaporation deposition, silver nanoparticles were shown to exhibit the smallest particle size, ranging from 2 nm to ~ 16 nm compared with EPD and spin coating methods. It is also observed that the sample prepared by e-beam evaporation technique is observed to form a better uniformity in both particle size and inter-particles spacing, which is ~2 nm to 8 nm.
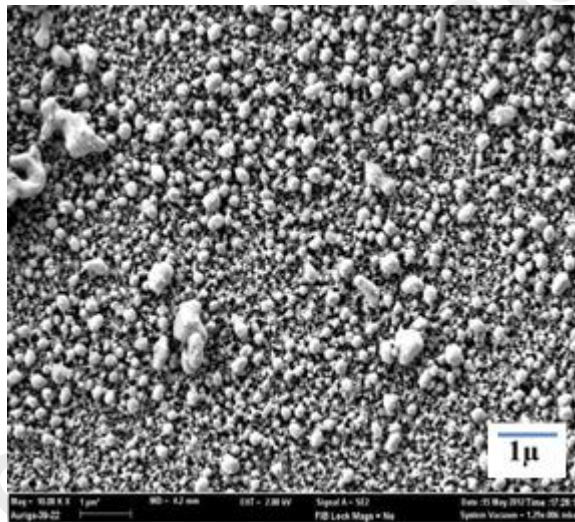
Figure 5.9 Field Emission Scanning Electron Microscopy (FESEM) image of silver nanoparticles prepared by EPD deposition method.
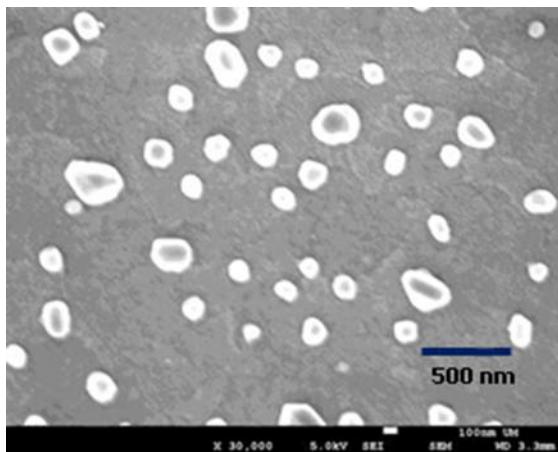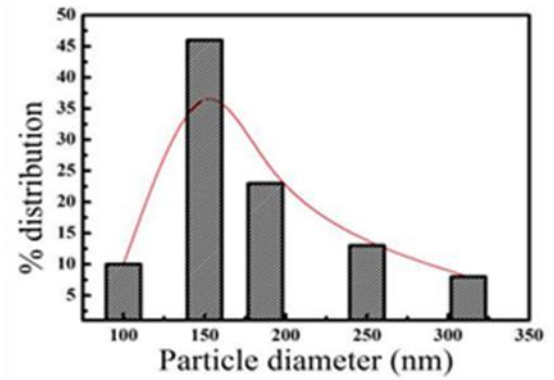
Figure 5.10 FESEM image of **(a)** silver nanoparticles prepared using spin coat technique and **(b)** graph of its particle size distribution.
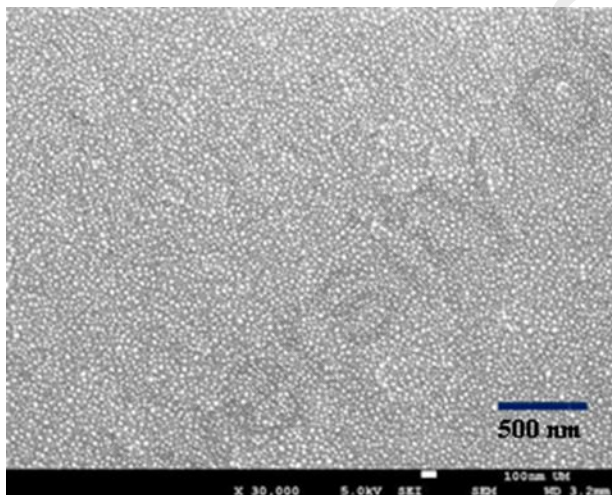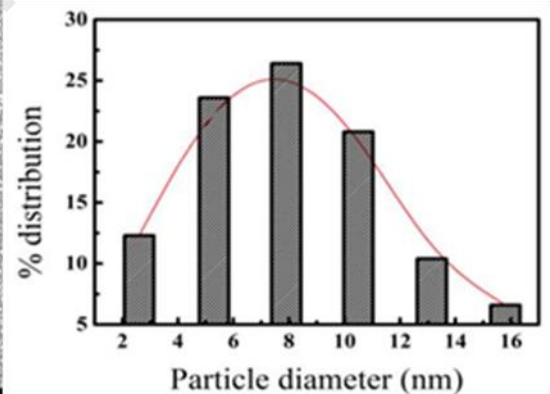
Figure 5.11 FESEM image of **(a)** silver nanoparticles prepared using e-beam evaporation method and **(b)** its particle size distribution shows particles sizes distributed evenly.

5.4.2.2 UV/VIS Absorption Spectra Behaviour

Figure 5.12 shows the absorbance spectra of the silver nanoparticles compared from these three techniques using the UV/VIS spectrometer. The absorbance spectrum of silver nano-particle prepared by EPD produced a very broad absorption across the whole EM wavelength range and a slight peak at 335 nm. Silver nano-particles prepared by spin coating technique showed an absorbance peak at a wavelength of 400 nm with a shoulder peak at a wavelength of 335 nm. The sample prepared by e-beam evaporation exhibited two absorbance peaks at 325 nm and the broader peak at ~430nm. The highest intensity of absorbance obtained was from the sample prepared by the EPD technique, while the lowest intensity obtained was from the e-beam evaporation technique. This may be due to the silver nanoparticles in EPD samples being in dense stacked particles, which may absorb a higher amount of light (Krishnan et al., 2014). Hence, from this comparison, it can be concluded that using e-beam evaporation gives the best results of SPR at the wavelength range of 450-500 nm, which implies the homogeneity and uniformity of particles on the substrate. The study of plasmonic behaviour on sphere-like silver nanoparticles formed with e-beam was continued by varying the annealing temperature in the next section.
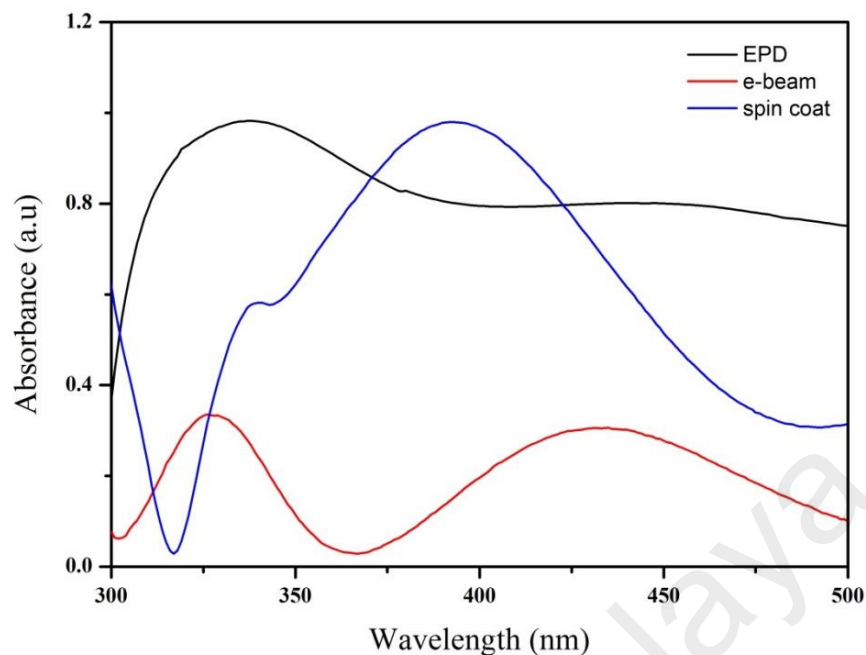
Figure 5.12 UV-Vis spectra shows absorbance of silver nanoparticles prepared by each technique.

5.5 Controlling the Size of Ag NPs Prepared by E-beam Evaporation Through Thermal Annealing

Generally, it is stated that the sphere-shaped formation of deposited silver nanoparticles (Ag NPs) is influenced by the annealing (Chan et al., 2013; Fleetham et al., 2015; Hung et al., 2010; Rukshan et al., 2012), thus, in this section, the post-annealing temperature was varied to get the optimum sphere shape with a desired particle size of silver nanoparticles with the most intense surface plasmon behaviour to be embedded inside organic solar cells device.

5.5.1 Results and Discussion

Figure 5.13 shows the FESEM images of silver nanoparticles prepared by e-beam evaporation technique with different annealing conditions; control sample (not annealed), annealed at 150 °C (herein known as 150 °C sample), and annealed at 250 °C (herein known as 250 °C sample). The samples were annealed for two hours. It can be observed that the control sample consists of a single layer adhered silver particles.

When the annealing temperature was set at 150 °C, the adhered particles started to detach from each other and form an island-like particles. As the temperature was further increased to 250 °C, the island-like particles were seem to be further detached and isolated from each other until they formed a spherical-like particles, which are very small and have specific inter-particle distance.
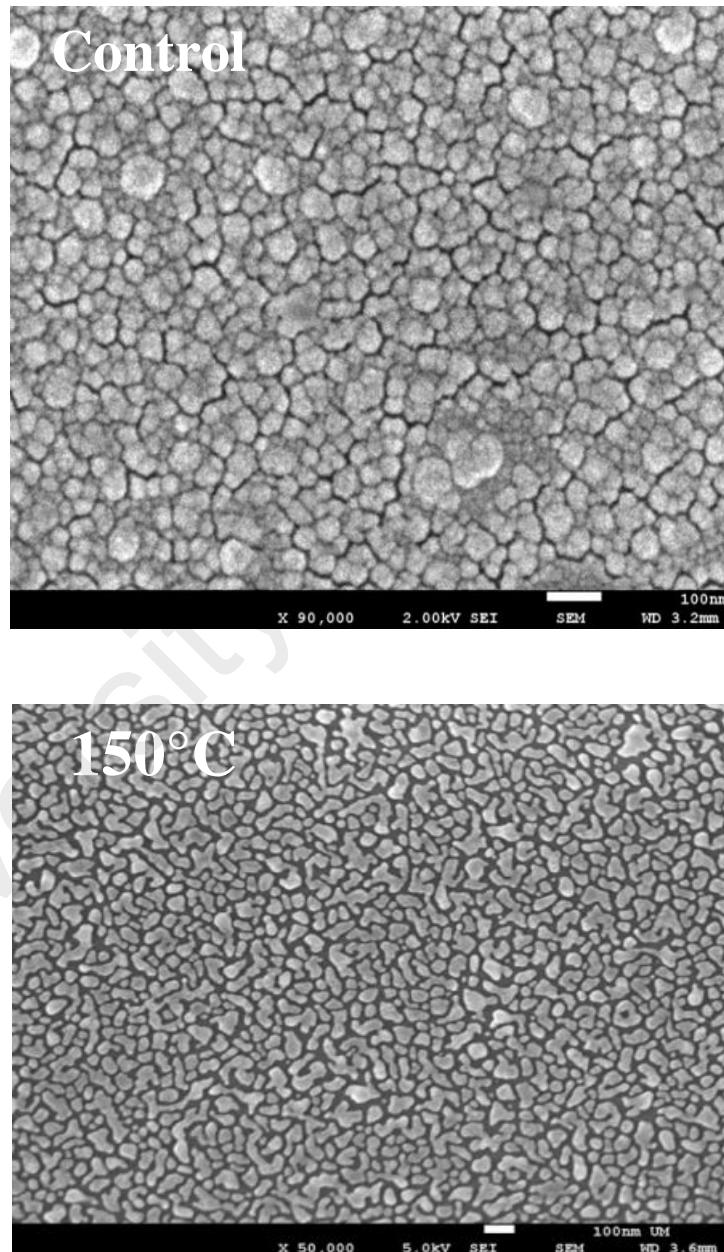
Figure 5.13 FESEM images of silver nanoparticles prepared by e-beam evaporation technique with different annealing condition
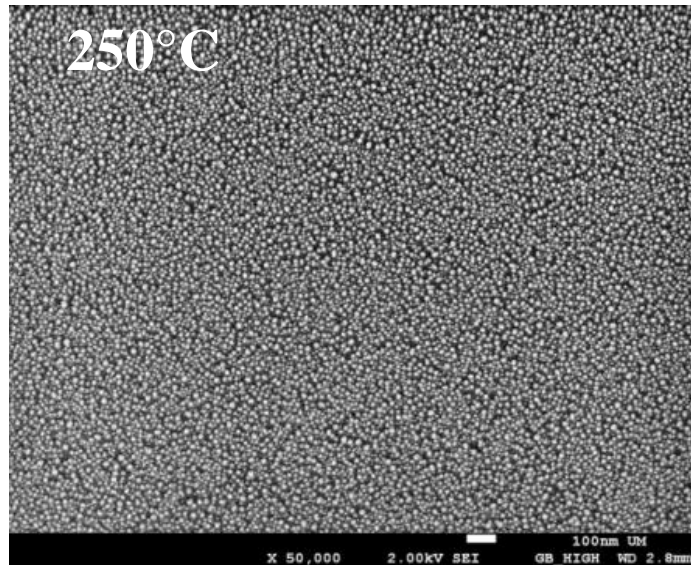
Figure 5.13 (continued) FESEM images of silver nanoparticles prepared by e-beam evaporation technique with different annealing condition

Figure 5.14 shows the absorption spectra of control, 150° C, and 250° C samples. The absorption peak of control sample, 150 °C sample, and 250°C sample are at 565 nm, 515 nm, and 455 nm respectively with 250 °C sample exhibiting a shoulder peak at 365 nm. The multiple peaks occurred may attribute to the plasmon generated by the coupling electromagnetic wave between two particles (Kinnan & Chumanov, 2010; Krishnan et al., 2014). As the temperature increases, the particle size is decreased and the absorption peaks move towards the blue shift. The smaller size of particles also shows the narrower absorption peak obtained. The narrower peak of sample annealed at 250°C shows the behaviour of surface plasmon resonance (SPR). This type of SPR is suitable for photovoltaic application as it enhances the light confinement inside the cells (Atwater & Polman, 2010; Fleetham et al., 2015; Liu et al., 2015).
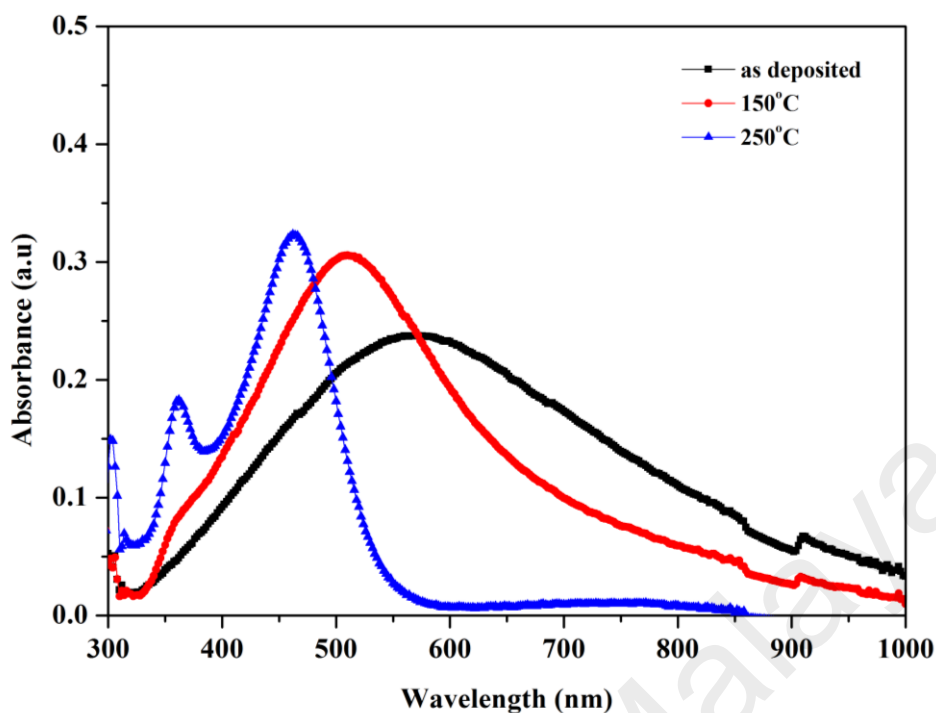
Figure 5.14 UV-Vis spectra shows absorbance of silver nanoparticles prepared by e-beam evaporation technique with different annealing condition.

5.5.2 Highlights

Three different distributions of Ag NPs have been successfully prepared by three different methods to study the surface plasmon tunability. The three different methods namely spin coating technique, EDP technique, and e-beam evaporation technique produced different particle sizes and distributions. From UV-Vis absorption spectra, it is clear that the surface plasmon varies with the variation of Ag NPs size distribution. The results showed that Ag NPs prepared e-beam, which has uniform particles distribution, produced narrower absorption peak. Narrower UV-Vis absorption peak of metal film leads to better surface plasmon behaviour (Kumar, 2013). The Ag NPs samples prepared by e-beam evaporation were then set into three different annealing conditions (not annealed, annealed at 150 °C and 250 °C) to study the annealing effect towards the plasmon behaviour. The UV-Vis result shows that Ag NPs annealed at 250 °C have the

smallest particle size, better particles shape consistency, and its uniform distribution has the narrowest absorption peak. It can also be concluded that as the annealing temperature increases to 250 °C, the particle size will be decreased, the absorption peak will be narrower and shifts to lower wavelength.

5.6   Summary

Various methods have been used to produce a variety of silver particles that differ in terms of particles shapes, sizes, and distribution. Flower-like shape silver was prepared via templating method, and dendritic shape silver was prepared by electrochemical process. The Ag NPs were almost spherical shape and were produced by several techniques such as e-beam evaporation, spin coating, and EPD technique to vary the particle sizes and distribution. The Ag NPs prepared by e-beam evaporation varied in their annealing condition so that the effect of annealing towards the silver particles' growth and its plasmon behaviour can be studied. These differences of silver particles' features offer the idea to study the surface plasmon tunability of silver. The surface plasmon changes when the size distribution of the silver particles changes and when the shapes are different. For example, dendritic shape of silver produces two absorptions peak with one is more prominent than the other, while flower-like structure produced a single broad absorption peak. Even for the same shape such as spherical, Ag NPs give a different line shape of SPR as they differ in terms of size, inter-particle distance, and particle distribution. Samples with smaller size of particles have more prominent and sharp peaks, while for sample of closely-packed Ag NPs produced broad absorption band. At adequate distance between two particles where the inter-particle distance is about the size of the particles itself, two absorption peaks occurred because of EM coupling between two particles. As every shape structure of silver particles have their

own unique properties of surface plasmon behaviour, their potential to enhance organic solar cells will be studied in the next chapter. The best method that produced Ag NPs, which have potential to enhance the organic solar cells, will be used to fabricating the real device.

CHAPTER 6: ENHANCEMENT OF VOPCPHO:P3HT ORGANIC SOLAR CELLS BY INCORPORATING SILVER NANOPARTICLES (AG NPS)

6.1   Introduction

Among the phthalocyanines family, vanadyl 2,9,16,23-tetraphenoxy-29H,31H-phthalocyanine (VOPcPhO) has a dominant absorption in the Q-band region i.e., from 600 to 800 nm, where the P3HT absorption is very little. This potential blend system is interesting, as the VoPcPhO has a bipolar transport and can act as an electron, as well as a hole transport material (Abdullah et al., 2012). From the previous chapter, various methods have been used to produce several types of plasmonic features such as dendritic, flower-like, and sphere particles to demonstrate the tunability of surface plasmon resonance. Their optical response towards the effect light absorption behaviour of VOPcPhO: P3HT blend system has been studied.

In this chapter, Ag NPs were incorporated in an organic layer for solar cells application. It is well known that Ag NPs are capable of inducing plasmonic effect that could increase the device efficiency (Kalfagiannis et al., 2012; Pillai et al., 2007). Ag NPs that have unique plasmonics behaviour would assist light trapping of organic solar cells hence increasing the efficiency of the device. VOPcPhO:P3HT blend system was first introduced by Abdullah *et al*. as the first donor-acceptor blend used as active material in organic solar cells (OSCs) device, in which the introduction of Ag NPs is the first approach in enhancing its efficiency (Abdullah et al., 2012). Despite chemically deposited Ag NPs, which has previously been introduced and optimized, the e-beam evaporation process in preparing Ag NPs is indeed an easy process, which could produce a very thin layer of particles down nano-meter range in controllable manner. In this chapter, the e-beam deposited Ag NPs sample was pursued for device fabrication process to study the enhancement proposed by the surface plasmon behaviour towards

the organic solar cells. Note that the Ag NPs were located between the ITO layer and the buffer layer of the organic device to help harvest light.

6.2 Effect of Ag NDS on VOPcPhO:P3HT Thin Film

In the previous chapter, results showed that Ag NDs were prepared by a chemical method of EPD, while Ag NPs were prepared by e-beam evaporation, which obtained prominent properties of plasmonic behaviour that is promising for device enhancement. Hence, this section discusses how Ag NDs structures affect the active layer, which composes of organic solar cells device. Silver nanodendrites (Ag NDs) have been included in the polymer thin films, as described previously in Chapter 3 (see Figure 3.11).

6.2.1 UV/VIS Spectra Analysis

The effect of Ag NDs preparation scan rates on the absorption spectroscopy of PEDOT: PSS/VOPcPhO: P3HT is presented here. The Ag NDs FESEM images have been presented and discussed in Section 5.2.2.1, and the results showed that Ag NDs were prepared at 10 mVs^{-1}, which produced smaller Ag NDs prepared at 1 mVs^{-1}. Figures 6.1 show the spectrum for UV-Vis PEDOT: PSS/VOPcPhO: P3HT in comparison with Ag NDs at 10 mVs^{-1}, Ag NDs at 1 mVs^{-1} and without Ag NDs. Generally, P3HT and VOPcPhO are mostly in the 450–800 nm range of the visible spectral region. In the P3HT spectrum, the absorption peak existed at 518 nm (Abdullah et al., 2012). The absorption spectrum of VOPcPhO has a main absorption at 665–715 nm, which corresponds to Q-band, as well as the Soret absorption bands in the region of 300–500 nm (Kamarundzaman et al., 2013). The presence of VOPcPhO material in the donor–acceptor blend P3HT:VOPcPhO results in the absorption spectrum of the composite extending to a longer wavelength, even with the presence of metallic structures. It is noticeable that the absorptions intensities are reduced for the

P3HT:VOPcPhO blend film implanted with Ag NDs at shorter wavelength ($\lambda < 450$ nm), but increases at wavelengths of 500–550 nm and 600–700 nm, which can be explained as the occurrence of LSPR-enhanced electromagnetic waves.

The UV-Vis results indicate P3HT:VOPcPhO film for organic solar cells provides considerable benefit; a high intensity occurs at low wavelength, and this intensity gradually decreases for the case of the polymer film, where it is embedded with bigger morphology of AgNDs (1 mVs^{-1}) and decreases noticeably with the smaller morphology of AgNDs (10 mVs^{-1}). In alignment with the well-known enhancement of solar cells by introducing Ag nanoparticles (Hamdan et al., 2014), Ag NDs also contributes enhancement up to a factor of 3 (~450 nm) in comparison with polymer blend film without Ag NDs. Thus, the scattering cross-section is believed to exceed the geometrical cross-section of the NDs at surface plasmon resonance, thereby increasing the amount of light scattered into the cell. Such rise in the light scattered within the polymer blend has caused the increment as shown in the absorption spectra in this study.
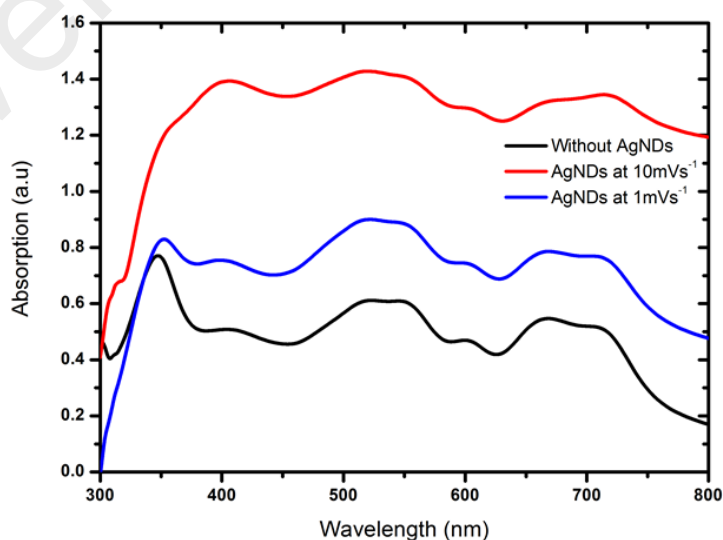
Figure 6.1 UV-Vis PEDOT:PSS/VOPcPhO:P3HT in comparison with Ag NDs at 10 mVs^{-1}, AgNDs at 1 mVs^{-1} and without AgNDs

6.2.2   PL Measurement

To study the influence of photoluminescence by using PL spectroscopy (RENISHAW), spectra were acquired under excitation from a frequency-doubled neodymium-doped yttrium aluminium garnet laser operating at λ_{exc}=532 nm focus through 10 x microscopy objective (NA = 0.8) at normal incidence. In the comparison of the photoluminescence of the Ag nano-dendrites with that of the Ag nanoparticles, the fluorescence enhancement should be attributed to the metal enhancement effect (Ye et al., 2011). The field enhancement can affect the spontaneous decay rate and PL intensity. According to theoretical studies of photoinduced luminescence, a single-photon luminescence power P_1 can be calculated for the excitation and emission energies $h\omega_{exc}$ and $h\omega_{em}$ using the following equation (Mohamed et al., 2000):

$$P_1 = 2^4\beta_1|E_0|^2V|L^2(\omega_{exc})L^2(\omega_{em})|, \tag{6.1}$$

where E_0 is the incident electric field and β_1 is the proportionality constant, which includes the intrinsic luminescence spectrum of the metallic compound. The resonant luminescence power increases with the increasing nanorod (Mohamed et al., 2000) length to a longer emission wavelength.

It was shown in other study that VOPcPhO: P3HT with the presence of Ag NDs showed quenching phenomena, which affect the photo-induced charge transfer efficiencies (Gfroerer, 2006). Thus, in order to find whether the electrochemically deposited Ag NDs has the effect on the photo-induced charge transfer efficiencies, the samples were subjected to PL measurement. Here, the effects of Ag NDs on PL spectra of PEDOT: PSS/VOPcPhO:P3HT and   P3HT: VOPcPhO (at ratio of 1:1.5), were studied. Figure 6.2 depicts the PL spectra of the thin films and their blends, obtained by an excitation wavelength of 325 nm in the range between 400--800 nm. The PL of the

film without Ag NDs (PEDOT:PSS/VOPcPhO:P3HT) shows a strong emission peak at 600 nm and a shoulder at 660 nm, laying near the red region, where the result is in agreement with the previous report (Abdullah et al., 2012). Introducing the Ag NDs into the PEDOT:PSS/VOPcPhO:P3HT blend film has caused a significant PL quenching compared with the film without Ag NDs. Furthermore, it can be seen that the film with Ag NDs prepared at 10 mVs^{-1} scan rates produced better quenching effect compared with the films prepared at 1 mVs^{-1} scan rate. The results indicated that the smaller size of silver nanodendrites (prepared at 10 mVs^{-1} scan rate), the better photoinduced charge transfer. The result from PL is also in agreement with the finding obtained from the absorption spectra. The excitons produced from light excitation in PL measurement have a limited lifetime and decayed or dissociated during charge transfer process. A photo-induced charge transfer process is considered to be the most common way to dissociate excitons into free electrons and holes (Motaung et al., 2009). The PL measurement suggests that one with integration of Ag NDs could improve the photo induced charge transfer in organic solar cells consisting the PEDOT:PSS/VOPcPhO:P3HT blend.
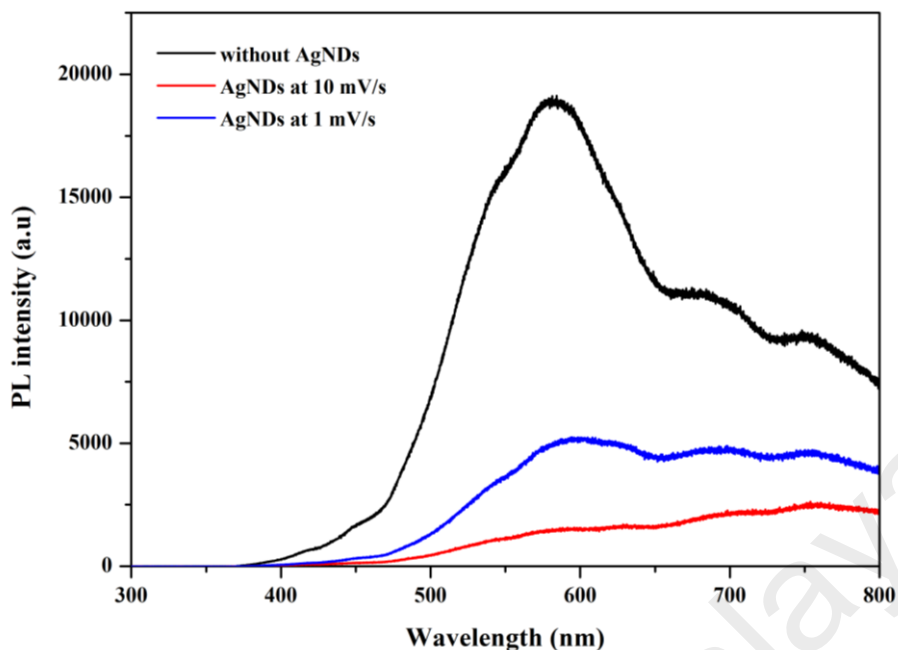
Figure 6.2 PL spectra of PEDOT:PSS/VOPcPhO:P3HT blend films (black line) without Ag NDs (red line) Ag NDs prepared at 10 mVs^{-1} scan rate and (blue line) Ag NDs prepared at 1 mVs^{-1} scan rate.

6.2.3   Constrain for further application of Silver Nanodendrites

Even though Ag NDs has shown promising result, the chemical method of EPD for this type of nano-structure is restraining it from further device fabrication. The substrate used in this deposition was small and did not fit in the mask that was used in device fabrication (deposition of aluminium top electrode). If larger substrates were used, larger container may be needed hence large amount of liquid solution must be added so that the substrate can be immersed. This may lead to a waste of solution liquid and is not economically friendly. Besides, this EPD method of silver nanodendrites is not suitable to be applied on the pre-patterned ITO substrates, which would reduce the ITO conductivity during electrochemical process. There are many constrains for application of silver nanodendrites prepared using electrochemical method in organic solar cells. Therefore, silver nanoparticles (Ag NPs) prepared using e-beam technique are used to

incorporate in organic solar cells device of VOPcPhO:P3HT blend. This e-beam method of the nanoparticle deposition has promising surface plasmon properties and it is a feasible technique.

6.3   The Incorporation of Ag NPs in VOPcPhO:P3HT Organic Solar Cells Device

6.3.1   Optical Investigation at PEDOT:PSS Buffer layer

Generally, the choice of buffer layer material has been studied and it has been proven that some criteria must be taken into account to produce optimum performance in organic photovoltaic device. Indeed, it has been demonstrated that selected material of buffer layer could noticeably increase the amount of absorbed light into active photovoltaic layer. By reducing the parasitic reflection of light at the interface, the amount of light that reaches active layer may be maximized. On the other hand, a mismatch in refractive index between two adjacent layers should be avoided as it leads to a reflection of light and causes the loss in light absorption of solar cells. Thus, to avoid losses in layers of the device structures, the absorption in active layer itself must be maximized. Therefore, the material for buffer layer must not absorb light effectively within the visible spectrum at the same wavelength range (Rand & Richter, 2014). The position of Ag NPs in between ITO and buffer layer in this research was concerning the fact mentioned above.

In this research, the addition of Ag NPs prior to PEDOT:PSS thin film deposition, has affected the optical behaviour of the buffer layer. Figure 6.3 shows the absorption and transmission spectra of PEDOT:PSS with and without the addition of Ag NPs. The line shape of the spectra of both graphs showed the common PEDOT:PSS absorption and transmission spectra at nano-meter range of thickness.

In terms of intensity, the addition of Ag NPs does not change the light absorption of PEDOT:PSS. However, the transmission spectra in Figure 6.3 (b) increased with the supplement of Ag NPs. Additionally, the total of incident light on a medium equals to the sum of absorbed, transmitted, and reflected light by that medium, therefore, in this case, the reflected light of buffer layer was decreased by the addition of Ag NPS.
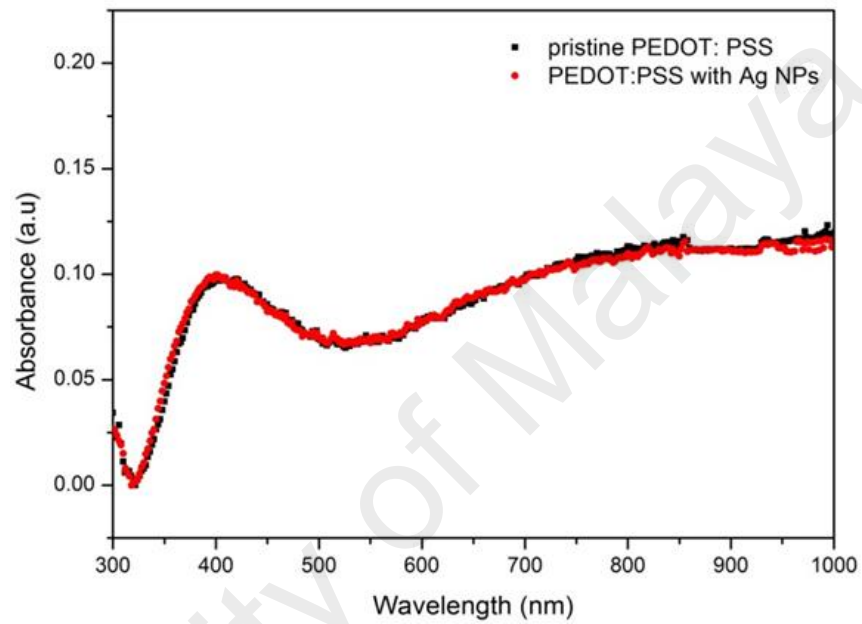
(a)

Figure 6.3 (a) absorption transmission spectra at buffer layer of PEDOT:PSS with and without the presence of Ag NPs and **(b)** transmission spectra at buffer layer of PEDOT:PSS with and without the presence of Ag NPs.
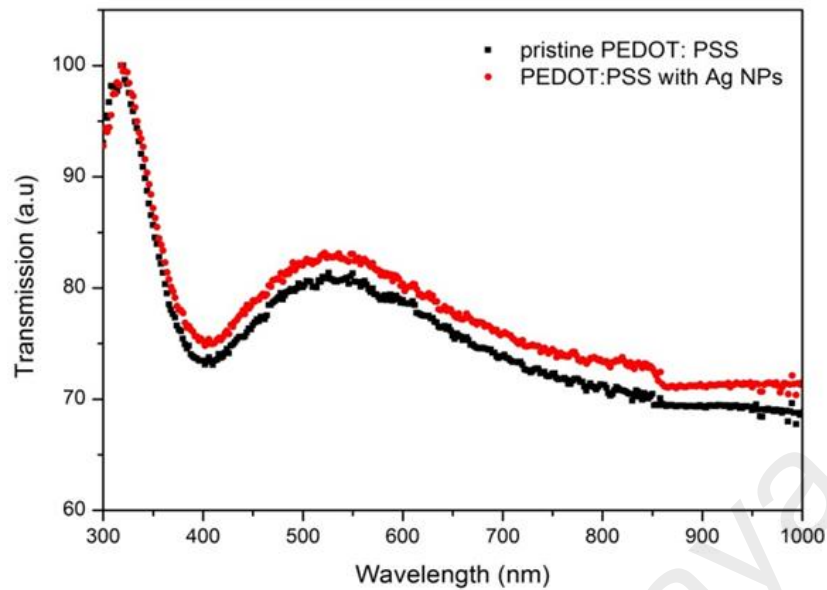
(b)

Figure 6.3 (continued) (a) absorption transmission spectra at buffer layer of PEDOT:PSS with and without the presence of Ag NPs and (b) transmission spectra at buffer layer of PEDOT:PSS with and without the presence of Ag NPs.

6.3.2   Optical Investigation at VOPcPhO:P3HT Organic Active Layer

It is important to have high absorption of light at active layer of OSC, thus contributing exciton production leading to better device performance. The VOPcPhO is perfectly suited to extend the absorption spectrum of P3HT, as shown by the blend absorption spectrum in Figure 6.4 (a). The figure shows that blend film exhibits an absorption spectrum that includes features of the two components, P3HT and VOPcPhO with respect to the wavelength shifts within 600-700 nm range. Effectively from Figure 6.4 (b), absorption increased with the presence of Ag NPs compared with none. As P3HT:VOPcPhO film is much thicker compared with the size of silver nanoparticles, a very small change can be seen on the absorbance as indicated by a small broad peak at 550 nm and 595 nm wavelengths. But overall, the existence of silver nanoparticles has made almost all the P3HT:VOPcPhO absorbance peak seems more prominent. This

suggests that at surface plasmon resonance, the scattering cross-section is believed to exceed the geometrical cross-section of the particle, thereby increasing the amount of light scattered into the cell (Stratakis & Kymakis, 2013).
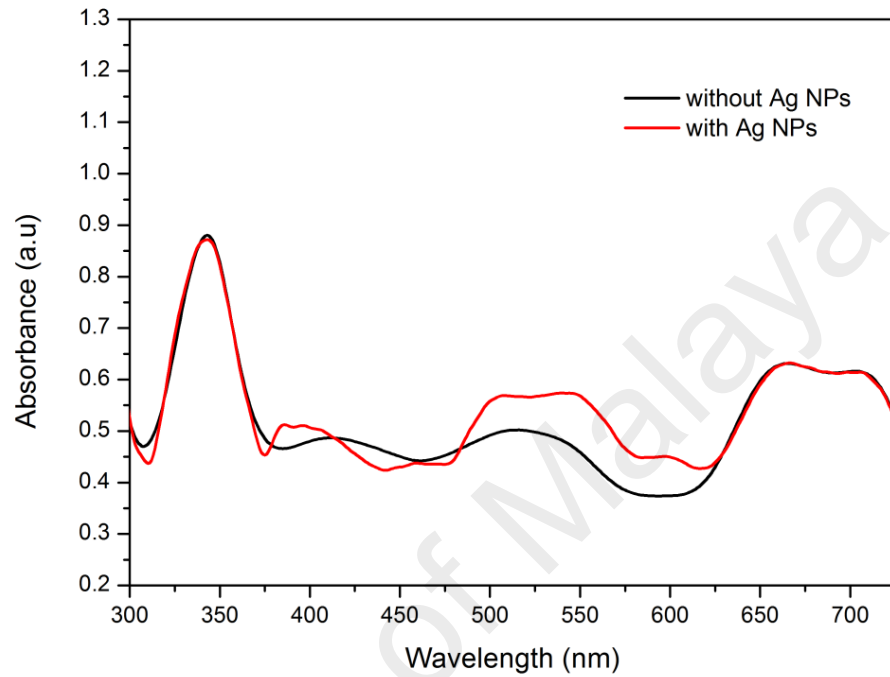
(a)

Figure 6.4 Optical absorption for material blend organic solar cell with and without the presence of Ag nanoparticles **a)** absorption spectra at whole visible wavelength range **b)** absorption spectra at wavelength range at the most affected absorption
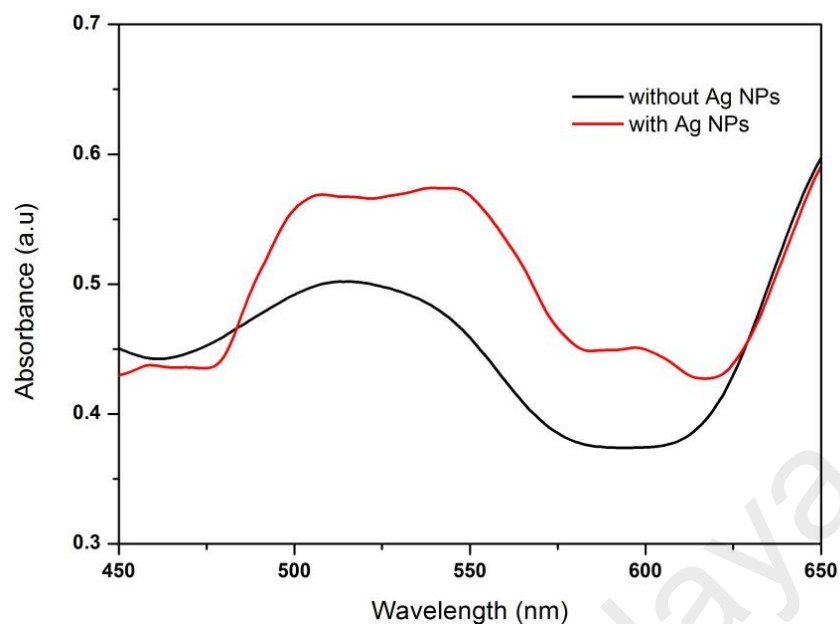
(b)

Figure 6.4 (continued) Optical absorption for material blend organic solar cell with
and without the presence of Ag nanoparticles a) absorption spectra at whole visible
wavelength range b) absorption spectra at wavelength range at the most affected
absorption

6.3.3 Current Density-Voltage (J-V) Characterization

The effect of silver nanoparticles within organic solar cells have been investigated
using the device configuration of ITO/PEDOT:PSS/VOPcPhO:P3HT/Al. The result in
Figure 6.5 shows improvement in VOPcPhO:P3HT organic solar cells with
incorporation of silver nanoparticles, compared with the reference device (without silver
nanoparticles). Better current density (J_{sc}) can be clearly visualised from this electrical
characterization. The overall performance of these organic solar cells is tabulated in
Table 6.1.
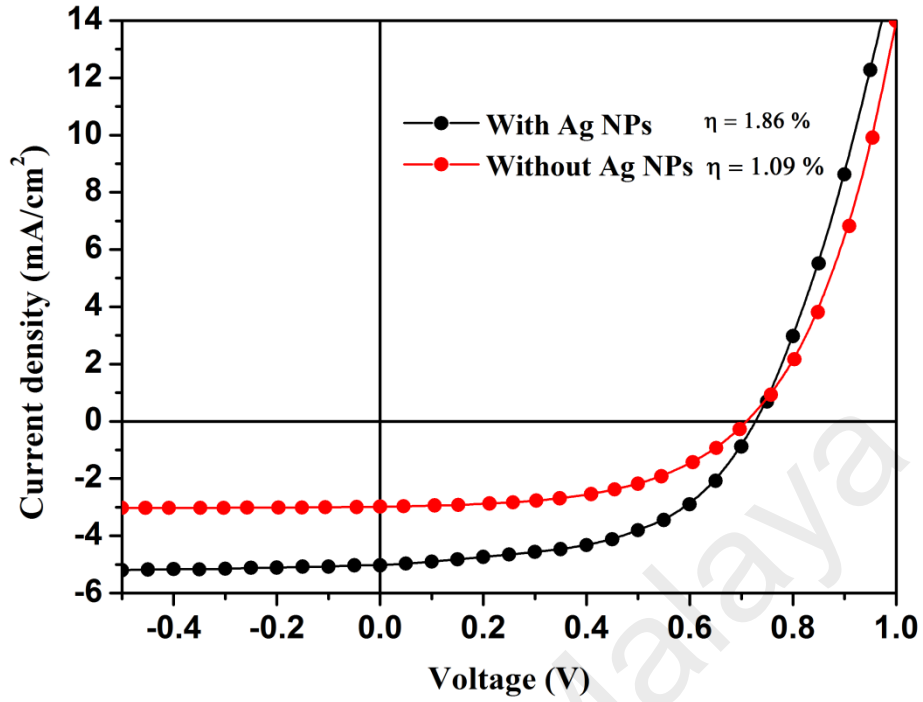
Figure 6.5 J-V characteristic of a pristine device and device with Ag NPs.

Table 6.1 OSCs parameters value with and without Ag NPs increase in efficiency with the presence of Ag

	J_{sc} (mA/cm^2)	V_{oc} (V)	Fill factor	Efficiency (%)
Without Ag NPs	2.98	0.71	0.51	1.09
With Ag NPs	5.03	0.72	0.51	1.86

The presence of Ag NPs has contributed a significant increase in short circuit current density value. However, the fill factor (FF) value remains the same and only a small change can be observed in the open circuit voltage, V_{oc} value. It can be seen that much improvement of efficiency was achieved mainly from the increase of photocurrent. It is thought that the addition of Ag nanoparticles causes the confining of light within the organic active material. The comparison in Table 6.1 shows that efficiency increased up

to 41% with the presence of silver nanoparticles in the device. It is worth mentioning that the enhancement of light trapping of the device was assisted by the plasmonic properties of silver nanoparticles, therefore improving the efficiency of organic solar cell device. This result is in agreement to the finding reported by other researchers using common P3HT:PCBM organic blend as active material (Kim et al., 2012; Li et al., 2013).

Such improvement in current density cannot be explained merely by correlating to the increase in light absorption alone. With the presence of plasmonic-assisted spherical silver nanoparticles within the active material layer, the device efficiency has improved from 1.09% to 1.86%. A conduction mechanism for this plasmonic solar cell has been explained by studying the space-charge-limited current region where the value of mobility can be obtained from the following expression (Rand & Richter, 2014):

$$J = \frac{9}{8}\varepsilon\varepsilon_\circ\theta\mu\frac{V^2}{d^3} \tag{6.2}$$

Where ε is the relative permittivity of organic material with value 3, $\varepsilon_\circ$ is the permittivity of free space, θ is the trap factor that can be obtained from the experiment ($\theta=J_1/J_2$), μ is the value charge carrier mobility across the junction device, and d is the thickness of effective material between two electrodes.
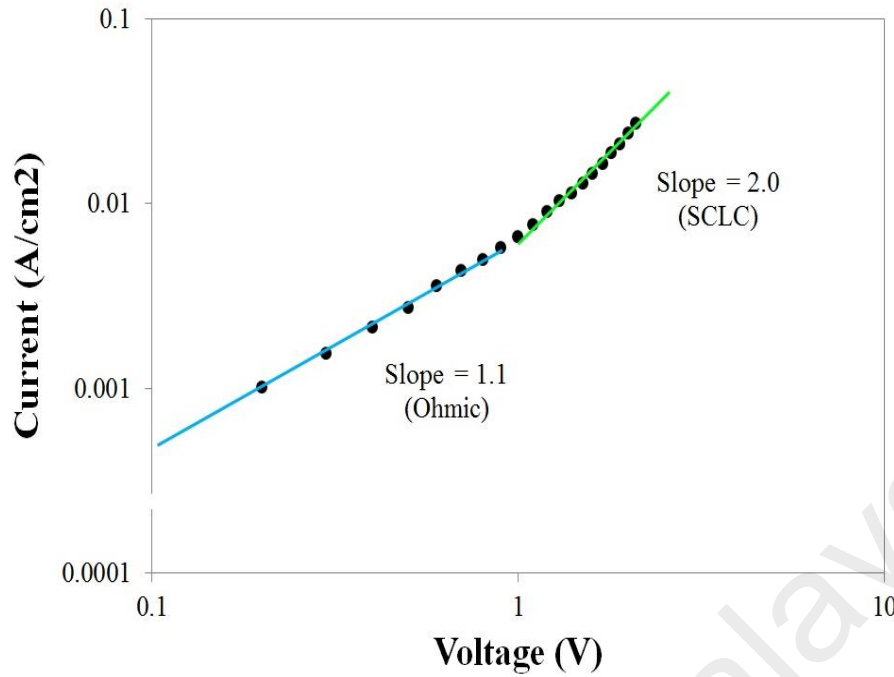
Figure 6.6 The physical conduction mechanism from double log scale of J vs. V

The electrical properties of the prepared OSC device, consisted of silver nanoparticle were measured in the dark, for the purpose of space-charge-limited current study. From Figure 6.6, a double log of current density (J) vs. voltage (V) has shown two main conduction regions where the first regime with slope ~1 is in Ohmic conduction and the second region with slope 2 is the SCLC conduction regime (Montero et al., 2009; Nešpůrek et al., 2008). The SCLC started to appear between 1-2 V where the mobility value is calculated from this region and found to be 0.39×10^{-5} cm^2/Vs. The SCLC mobility measurement was performed using the same plasmonic cell device after a few weeks of the device fabrication. It is believed that this mobility value has been reduced for the aged device, but the value is considerably sufficient (10^{-5}–10^{-4} cm^2/Vs) for solar cells application.

6.3.4   Stability Study

The influence of silver nanoparticles on the ageing process was performed to investigate the device's stability. The time scale was taken between 1 to 28 days (weekly basis), after the device fabrication. The efficiency of the OSC were calculated based on the results obtained from the photovoltaic characteristics of the aged devices. A stability study has been conducted to investigate enhancement in the stability aspect of the device with Ag NPs. The efficiency of both devices (with and without Ag NPs) was measured on certain days for four weeks. The measured efficiency data of each day was recorded by normalizing with the efficiency of fresh device (efficiency measured right after device fabrication was done).

The recorded result of normalized efficiency is tabulated in Table 6.2, and can be clearly visualised in Figure 6.7. The fresh device indicates I-V measurement was taken just after completing fabrication process. As observed in Figure 6.7, the pristine device (without Ag NPs) has experienced a significant drop in efficiency to almost half of the initial value, whereas the device with Ag NPs has an efficiency to only drop to 65% of its initial value on the second day of measurement. After a week, the efficiency of devices with Ag NPs continued to drop to 52% and became stable upon reaching ~40% drop on the following weeks. The pristine device showed fluctuated stability decay and reached the minimum drop to 27% at the end of the measurement. This trend line of stability degrading of pristine device was expected, as organic solar cells degraded rapidly under both environmental and light exposure, as reported by Dalal *et. al* (Dalal et al., 2012). Normally, the high humidity environment exposure was attributed to critically affecting the condition of organic materials itself. They also reported that even in the absence or oxygen, the buffer layer is potentially changing under photon exposure and affecting the overall mobility of holes in the active layer. Thus, it is believed that the presence of Ag NPs before the buffer layer has improved the low durability of the

layer caused by the photon exposure when the measurement was taken under illumination.

Table 6.2 Normalized efficiency value of pristine and Ag NPs solar cells device from day 1 until day 28

Time (Days)	Normalize Efficiency (η/η_o)	
	Pristine	with Ag NPs
1	1.00	1.00
2	0.49	0.65
7	0.56	0.52
14	0.30	0.39
21	0.38	0.42
28	0.27	0.38
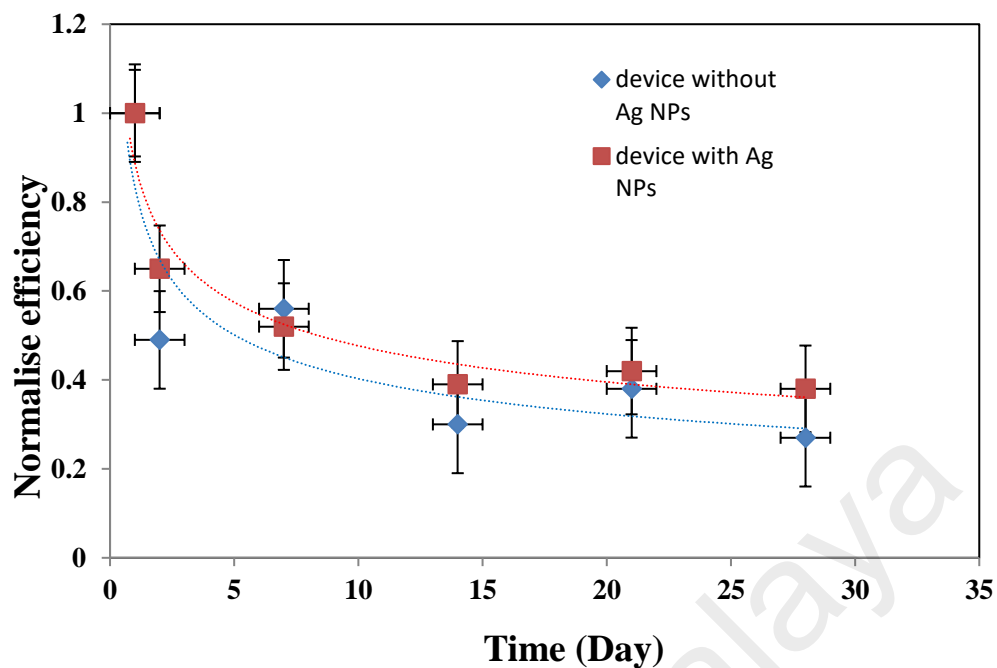
Figure 6.7 Normalized efficiency of both pristine and Ag NPs solar cells device versus time in day

6.4 Summary

In this research, although the dendritic and flower-like silver particles have interesting characters of surface plasmon, the fabrication process restricts the samples to be used for the device fabrication. Therefore, only silver nanoparticles prepared by e-beam evaporation process were available to be utilized in OSC fabrication as well as electrical characterisation study. Other than easing the fabrication process, the result for surface plasmon behaviour of this type of silver particle was considerably good. Besides, Ag NPs prepared by e-beam annealed at 250°C proposed a good trend of plasmonic behaviour that is promising to increase light absorption in organic solar cells.

Ag NPs have been successfully integrated into the OSC device. The OSC device consisted of VOPcPhO:P3HT, which is a new blend system for bulk heterojunction solar cell that acts as an active layer. It is concluded that the addition of silver nanoparticles prior to PEDOT:PSS buffer layer has assisted light transmission through

the buffer layer, hence increasing the absorbed light at the active layer. It also increases the light absorption in OSC, which led to the increasing performance up to 41% of device efficiency. It is suggested that the ability of Ag NPs to harvest and confine light inside the OSC has improved the stability of the device.

CHAPTER 7: CONCLUSIONS

In this thesis, a few attempts in producing different silver nanoparticles structures to study their optical performance and their significance in increasing the performance of organic solar cells, are presented. The study includes numerical simulation and experimental approach. The numerical approach has been conducted by using FDTD simulations. The experimentally fabricated nanoparticles were successfully integrated in organic solar cells blend system and a significant increase in efficiency was reported.

The simulation of 3-D simulation set up using FDTD software has been successfully utilized to study and observe the optical behaviour of perfectly spherical silver nanoparticles. The varied size of silver particles shows red-shifted resonance peak with the increment of particle size. The results obtained showed a very significant pattern of tunable light scattering through size-dependant silver sphere particles. The addition of silver particles on top of silicon substrate has increased the absorption inside the silicon by forward light scattering by the particles.

Furthermore, a numerical investigation has been performed on the feasibility of fabricating plasmonic absorption enhancement structures for silicon thin film solar cells using optical lithography techniques. Simulation results indicated reliable mass production capability of optical lithography techniques can be utilized for fabricating nanowires with plasmon resonance tunability from λ=750 nm to λ =2400 nm covering the entire long wavelength range of solar radiation. These nanowires may lead to improved absorption enhancement to Ohmic loss ratio by serving the dual purpose of plasmonic enhancement of impurity photovoltaic effect and effective extraction of photo-generated carriers.

The effect of optical properties towards size distribution and particle separation dependant has been studied experimentally and is assembled into 2-D arrays in close proximity to each other so that the local electromagnetic field of each particle overlaps with the neighbouring particles, and the system undergoes coherent plasmon coupling that is manifested as an intense and spectrally narrow plasmon mode in the blue spectral range. The result showed that the silver nanopartilces prepared by e-beam evaporation with size of particles ~15 nm with inter-particles distance of ~20 nm measured from centre to centre yield the most intense and sharpest plasmon resonance.

Silver micro-flowers have been physically deposited by using a template. The results displayed a considerable enhancement effect in both absorption and photoluminescence analysis comparable to spherical structures. This finding showed that such metal micro-flowers exhibit strong absorption spectra with a main SPR red-shifted in comparison with spherical structures. This is due to the morphology of the flower-like structures occurring at the interstices in between petals occupying larger areas and yielding larger field enhancement factors. However, the surface plasmon is not as intense as the spherical shape. Furthermore, this fabrication method still needs to be optimised to be experimentally able for integrating silver micro-flowers in organic solar cells device.

Apart from that, analysis of the effects of chemically deposited silver nano-dendrites in the active layer of solar cells has been conducted. The examination of UV-Vis absorption spectra confirmed that the presence of silver nano-dendrites increased the absorption of light in organic photovoltaic layers, and photoluminescence analysis indicated the existence of an electronic transition effect. Hence integrating silver nano-dendrites in organic solar cells device was considerable but still it must be further optimised in the fabrication process for further device fabrication. Nevertheless, this

thesis has contributed to an elaborate evidence that surface plasmon is very sensitive and highly tunable towards favourable applications.

Finally, the spherical shape of silver nanoparticles has been introduced into organic solar blend system of VOPcPhO:P3HT. The presence of silver nanoparticles in the blend system has shown a very significant impact towards its optical and electrical properties. The size distribution and homogeneity of silver nanoparticles deposited by e-beam evaporation technique produced a good trend of surface plasmon behaviour, in which this behaviour leads towards the performance of the charge-carrying activity of the VOPcPhO:P3HT blend system. These results can be further used for photovoltaic application where more theoretical studies to be carried out for better understanding.

For future work may be focus on optimizing the experimental method of fabricating various plasmonic structure such as dendritic and flower-like structure, so that it can be include in organic solar cells as well. Hence, the change in performance of OSCs due to the incorporation of those structure can be investigate as they also proposed unique behaviour of SPR. The effect of plasmonic towards OSCs device also can be further study by applying the silver structure in other layers of OSC instead of on top of the device. By this way, the enhancement of OSC by the inclusion of plasmonic structure may be due to local field enhancement of LSPR.

REFERENCES

Abdullah, S. M., Ahmad, Z., Aziz, F., & Sulaiman, K. (2012). Investigation of VOPcPhO as an acceptor material for bulk heterojunction solar cells. *Organic Electronics, 13*(11), 2532-2537.

Aden, A. L., & Kerker, M. (1951). Scattering of Electromagnetic Waves from Two Concentric Spheres. *Journal of Applied Physics, 22*(10), 1242-1246.

Ahmad Makinudin, A. H., Fakir, M. S., & Supangat, A. (2015). Metal phthalocyanine: fullerene composite nanotubes via templating method for enhanced properties. *Nanoscale Research Letters, 10*, 53.

Atwater, H. A., & Polman, A. (2010). Plasmonics for improved photovoltaic devices. *Nat Mater, 9*(3), 205-213.

Berenger, J.-P. (1996). Three-Dimensional Perfectly Matched Layer for the Absorption of Electromagnetic Waves. *Journal of Computational Physics, 127*(2), 363-379.

Bläsi, B., Hauser, H., Höhn, O., Kübler, V., Peters, M., & Wolf, A. J. (2011). Photon Management Structures Originated by Interference Lithography. *Energy Procedia, 8*, 712-718.

Bogaerts, W., Wiaux, V., Taillaert, D., Beckx, S., Luyssaert, B., Bienstman, P., & Baets, R. (2002). Fabrication of photonic crystals in silicon-on-insulator using 248-nm deep UV lithography. *IEEE Journal of Selected Topics in Quantum Electronics, 8*(4), 928-934.

Bohren, C., & Huffman, D. (1998). *Absorption and Scattering of Light by Small Particles*: Wiley-VCH.

Bohren, C. F., & Huffman, D. R. (1983). *Absorption and scattering of light by small particles*: Wiley.

Bond, A. M. (2002). *Broadening Electrochemical Horizons: Principles and Illustration of Voltammetric and Related Techniques*: Oxford University Press.

Catchpole, K. R., Mokkapati, S., Beck, F., Wang, E.-C., McKinley, A., Basch, A., & Lee, J. (2011). Plasmonics and nanophotonics for photovoltaics. *MRS Bulletin, 36*(06), 461-467.

Catchpole, K. R., & Polman, A. (2008). Plasmonic solar cells. *Optics Express, 16*(26), 21793-21800.

Chan, K. W., Rahman, S. A., & Aspanut, Z. (2013). Effect of rapid thermal annealing time on Au/SiOx film prepared by hot wire assisted plasma enhanced chemical vapour deposition technique. *Materials Chemistry and Physics, 140*(1), 37-41.

Dalal, V. L., Mayer, R., Bhattacharya, J., & Samiee, M. (2012, 15-19 April 2012). *Stability of organic solar cells.* Paper presented at the Reliability Physics Symposium (IRPS), 2012 IEEE International.

Das, A. K., & Raj, C. R. (2010). Facile growth of flower-like Au nanocrystals and electroanalysis of biomolecules. *Journal of Electroanalytical Chemistry, 638*(2), 189-194.

Derkacs, D., Lim, S. H., Matheu, P., Mar, W., & Yu, E. T. (2006). Improved performance of amorphous silicon solar cells via scattering from surface plasmon polaritons in nearby metallic nanoparticles. *Applied Physics Letters, 89*(9), 093103.

Drude, P. (1900a). Zur Elektronentheorie der Metalle. *Annalen der Physik, 306*(3), 566-613.

Drude, P. (1900b). Zur Elektronentheorie der Metalle; II. Teil. Galvanomagnetische und thermomagnetische Effecte. *Annalen der Physik, 308*(11), 369-402.

Duche, D., Torchio, P., Escoubas, L., Monestier, F., Simon, J.-J., Flory, F., & Mathian, G. (2009). Improving light absorption in organic solar cells by plasmonic contribution. *Solar Energy Materials and Solar Cells, 93*(8), 1377-1382.

Ebadi, M., Basirun, W., Alias, Y., & Mahmoudian, M. (2011). Normal and Anomalous Codeposition of Ni-Co-Fe-Zn Alloys from EMIC/EG in the Presence of an External Magnetic Field. *Metallurgical and Materials Transactions A, 42*(8), 2402-2410.

El-Nahass, M., Abd-El-Rahman, K., & Darwish, A. (2005). Fourier-transform infrared and UV–vis spectroscopes of nickel phthalocyanine thin films. *Materials Chemistry and Physics, 92*(1), 185-189.

Elumalai, N. K., & Uddin, A. (2016). Open circuit voltage of organic solar cells: an in-depth review. *Energy & Environmental Science, 9*(2), 391-410.

Fedlheim, D. L., & Foss, C. A. (2001). *Metal Nanoparticles: Synthesis, Characterization, and Applications*: Taylor & Francis.

Fleetham, T., Choi, J.-Y., Choi, H. W., Alford, T., Jeong, D. S., Lee, T. S., . . . Kim, I. (2015). Photocurrent enhancements of organic solar cells by altering dewetting of plasmonic Ag nanoparticles. *Scientific Reports, 5*, 14250.

Freise, A. (2012). Optical Metamaterials: Fundamentals and Applications, by W. Cai and V. Shalaev. *Contemporary Physics, 53*(3), 278-279.

Frondelius, P., Häkkinen, H., & Honkala, K. (2010). Formation of Gold(I) Edge Oxide at Flat Gold Nanoclusters on an Ultrathin MgO Film under Ambient Conditions. *Angewandte Chemie International Edition, 49*(43), 7913-7916.

Gfroerer, T. H. (2006). Photoluminescence in Analysis of Surfaces and Interfaces *Encyclopedia of Analytical Chemistry*: John Wiley & Sons, Ltd.

Hamdan, K. S., Abdullah, S. M., Sulaiman, K., & Zakaria, R. (2014). Effects of silver nanoparticles towards the efficiency of organic solar cells. *Applied Physics A, 115*(1), 63-68.

Hoppe, H., & Sariciftci, N. (2004). Organic solar cells: An overview. *Journal of Materials Research, 19*(07), 1924-1945.

Hostetler, M. J., Wingate, J. E., Zhong, C.-J., Harris, J. E., Vachet, R. W., Clark, M. R., . . . Murray, R. W. (1998). Alkanethiolate Gold Cluster Molecules with Core Diameters from 1.5 to 5.2 nm: Core and Monolayer Properties as a Function of Core Size. *Langmuir, 14*(1), 17-30.

Hung, W.-C., Liu, T.-K., Jiang, I. M., Tsai, M.-S., Yeh, P., & Cheng, W.-H. (2010). *Dynamically optical response of silver nanoparticle film under an annealing treatment.*

International Commission on Illumination, & Committee, E.-L. M. (1970). *Principles of light measurements*: Bureau central.

Ishii, H., Kudo, K., Nakayama, T., & Ueno, N. (2015). *Electronic Processes in Organic Electronics: Bridging Nanostructure, Electronic States and Device Properties*: Springer Japan.

Izzat Azmer, M., Ahmad, Z., Sulaiman, K., & Touati, F. (2016). Morphological and structural properties of VoPcPhO:P3HT composite thin films. *Materials Letters, 164*, 605-608.

Jones, H. (1957). Introduction to Solid State Physics by C. Kittel. *Acta Crystallographica, 10*(5), 390.

Jørgensen, M., Norrman, K., & Krebs, F. C. (2008). Stability/degradation of polymer solar cells. *Solar Energy Materials and Solar Cells, 92*(7), 686-714.

Kalfagiannis, N., Karagiannidis, P. G., Pitsalidis, C., Panagiotopoulos, N. T., Gravalidis, C., Kassavetis, S., . . . Logothetidis, S. (2012). Plasmonic silver nanoparticles for improved organic solar cells. *Solar Energy Materials and Solar Cells, 104*, 165-174.

Kalowekamo, J., & Baker, E. (2009). Estimating the manufacturing cost of purely organic solar cells. *Solar Energy, 83*(8), 1224-1231.

Kamarundzaman, A., Fakir, M. S., Supangat, A., Sulaiman, K., & Zulfiqar, H. (2013). Morphological and optical properties of hierarchical tubular VOPcPhO nanoflowers. *Materials Letters, 111*, 13-16.

Kim, K.-D., Seo, B. Y., Lee, J. Y., Song, Y., Hong, E. M., Kim, Y. D., . . . Cho, S. (2015). Effect of size and morphology of Au nanostructures on boosting performance of organic photovoltaic devices: Plasmonic and non-plasmonic effects. *Current Applied Physics, 15*(9), 1090-1094.

Kim, R. S., Zhu, J. F., Park, J. H., Li, L., Yu, Z. B., Shen, H. J., . . . Pei, Q. B. (2012). E-beam deposited Ag-nanoparticles plasmonic organic solar cell and its absorption enhancement analysis using FDTD-based cylindrical nano-particle optical model. *Optics Express, 20*(12), 12649-12657.

Kim, S.-S., Na, S.-I., Jo, J., Kim, D.-Y., & Nah, Y.-C. (2008). Plasmon enhanced performance of organic solar cells using electrodeposited Ag nanoparticles. *Applied Physics Letters, 93*(7), 073307.

Kinnan, M. K., & Chumanov, G. (2010). Plasmon Coupling in Two-Dimensional Arrays of Silver Nanoparticles: II. Effect of the Particle Size and Interparticle Distance. *The Journal of Physical Chemistry C, 114*(16), 7496-7501.

Kiomarsipour, N., Shoja Razavi, R., Ghani, K., & Kioumarsipour, M. (2013). Evaluation of shape and size effects on optical properties of ZnO pigment. *Applied Surface Science, 270*(0), 33-38.

Kippelen, B., & Bredas, J.-L. (2009). Organic photovoltaics. *Energy & Environmental Science, 2*(3), 251-261.

Kraus, M., Richler, S., Opitz, A., Brütting, W., Haas, S., Hasegawa, T., . . . Schreiber, F. (2010). High-mobility copper-phthalocyanine field-effect transistors with tetratetracontane passivation layer and organic metal contacts. *Journal of Applied Physics, 107*(9), 094503.

Kreibig, U., & Genzel, L. (1985). Optical absorption of small metallic particles. *Surface Science, 156, Part 2*(0), 678-700.

Kreibig, U., & Vollmer, M. (1995). *Optical properties of metal clusters*: Springer.

Kreibig, U., & Volmer, M. (1995). *Optical properties of metal clusters*: Springer.

Kretschmann, E., & Raether, H. (1968). Radiative decay of nonradiative surface plasmons excited by light. *Z. Naturforsch. A, 23*, 2135.

Krishnan, A., Das, S., Krishna, S. R., & Khan, M. Z. A. (2014). Multilayer nanoparticle arrays for broad spectrum absorption enhancement in thin film solar cells. *Optics Express, 22*(S3), A800-A811.

Kumar, C. S. S. R. (2013). *UV-VIS and Photoluminescence Spectroscopy for Nanomaterials Characterization*: Springer Berlin Heidelberg.

Kunz, K. S., & Luebbers, R. J. (1993). *The Finite Difference Time Domain Method for Electromagnetics*: Taylor & Francis.

Kunz, O., Ouyang, Z., Varlamov, S., & Aberle, A. G. (2009). 5% Efficient evaporated solid-phase crystallised polycrystalline silicon thin-film solar cells. *Progress in Photovoltaics: Research and Applications, 17*(8), 567-573.

Kuzma, A., Weis, M., Flickyngerova, S., Jakabovic, J., Satka, A., Dobrocka, E., . . . Donoval, D. (2012). Influence of surface oxidation on plasmon resonance in monolayer of gold and silver nanoparticles. *Journal of Applied Physics, 112*(10), 103531.

Langmuir, I. (1928). Oscillations in Ionized Gases. *Proceedings of the National Academy of Sciences, 14*(8), 627-637.

Lee, J. W., Bae, U., Lee, D. C., Lee, H. R., Shim, J. Y., & Linton, J. A. (2008). Renal Manifestations and Visceral Adiposity in Apparently Healthy Korean Women. *Kidney and Blood Pressure Research, 31*(6), 416-420.

Li, X., Choy, W. C. H., Lu, H., Sha, W. E. I., & Ho, A. H. P. (2013). Efficiency Enhancement of Organic Solar Cells by Using Shape-Dependent Broadband Plasmonic Absorption in Metallic Nanoparticles. *Advanced Functional Materials, 23*(21), 2728-2735.

Lin, S.-J., Lee, K.-C., Wu, J.-L., & Wu, J.-Y. (2012). Plasmon-enhanced photocurrent in dye-sensitized solar cells. *Solar Energy, 86*(9), 2600-2605.

Lindquist, N. C., Luhman, W. A., Oh, S.-H., & Holmes, R. J. (2008). Plasmonic nanocavity arrays for enhanced efficiency in organic photovoltaic cells. *Applied Physics Letters, 93*(12), 123308.

Link, S., & El-Sayed, M. A. (1999). Spectral Properties and Relaxation Dynamics of Surface Plasmon Electronic Oscillations in Gold and Silver Nanodots and Nanorods. *The Journal of Physical Chemistry B, 103*(40), 8410-8426.

Liu, X., Li, D., Sun, X., Li, Z., Song, H., Jiang, H., & Chen, Y. (2015). Tunable Dipole Surface Plasmon Resonances of Silver Nanoparticles by Cladding Dielectric Layers. *Scientific Reports, 5*, 12555.

Lu, L., Luo, Z., Xu, T., & Yu, L. (2013). Cooperative Plasmonic Effect of Ag and Au Nanoparticles on Enhancing Performance of Polymer Solar Cells. *Nano Letters, 13*(1), 59-64.

Lu, N., Li, L., Sun, P., & Liu, M. (2014). Short-circuit current model of organic solar cells. *Chemical Physics Letters, 614*, 27-30.

Lükermann, F., Heinzmann, U., & Stiebig, H. (2012). Plasmon enhanced resonant defect absorption in thin a-Si:H n-i-p devices. *Applied Physics Letters, 100*(25), 253907.

Lv, J., Lai, F., Huang, Z., Qu, Y., & Gai, R. (2007). Effects of substrate temperature and annealing in air on optical properties of Ag films prepared by thermal evaporation, *6722*, 67222K-67222K-67226.

Machui, F., Langner, S., Zhu, X., Abbott, S., & Brabec, C. J. (2012). Determination of the P3HT:PCBM solubility parameters via a binary solvent gradient method: Impact of solubility on the photovoltaic performance. *Solar Energy Materials and Solar Cells, 100*, 138-146.

Maier, S. (2007). Plasmonics fundamentals and applications. *Plasmonics: Fundamentals and Applications.* Retrieved from http://dx.doi.org/10.1007/0-387-37825-1

Malynych, S., & Chumanov, G. (2003). Light-Induced Coherent Interactions between Silver Nanoparticles in Two-Dimensional Arrays. *Journal of the American Chemical Society, 125*(10), 2896-2898.

Mandal, A., & Chaudhuri, P. (2013). Contribution of higher order plasmonic modes on optical absorption enhancement in amorphous silicon thin films. *Optics Communications, 300*, 77-84.

Mertz, J. (2000). Radiative absorption, fluorescence, and scattering of a classical dipole near a lossless interface: a unified description. *Journal of the Optical Society of America B, 17*(11), 1906-1913.

Mohamed, M. B., Volkov, V., Link, S., & El-Sayed, M. A. (2000). The `lightning' gold nanorods: fluorescence enhancement of over a million compared to the gold metal. *Chemical Physics Letters, 317*(6), 517-523.

Mokkapati, S., & Catchpole, K. R. (2012). Nanophotonic light trapping in solar cells. *Journal of Applied Physics, 112*(10), 101101.

Montero, J. M., Bisquert, J., Garcia-Belmonte, G., Barea, E. M., & Bolink, H. J. (2009). Trap-limited mobility in space-charge limited current in organic layers. *Organic Electronics, 10*(2), 305-312.

Motaung, D. E., Malgas, G. F., Arendse, C. J., Mavundla, S. E., & Knoesen, D. (2009). Structural and photo-physical properties of spin-coated poly(3-hexylthiophene) thin films. *Materials Chemistry and Physics, 116*(1), 279-283.

Muduli, S., Game, O., Dhas, V., Vijayamohanan, K., Bogle, K. A., Valanoor, N., & Ogale, S. B. (2012). TiO2–Au plasmonic nanocomposite for enhanced dye-sensitized solar cell (DSSC) performance. *Solar Energy, 86*(5), 1428-1434.

Mulvaney, P. (1996). Surface Plasmon Spectroscopy of Nanosized Metal Particles. *Langmuir, 12*(3), 788-800.

Murray, W. A., & Barnes, W. L. (2007). Plasmonic Materials. *Advanced Materials, 19*(22), 3771-3782.

Nešpůrek, S., Zmeškal, O., & Sworakowski, J. (2008). Space-charge-limited currents in organic films: Some open problems. *Thin Solid Films, 516*(24), 8949-8962.

Notarianni, M., Vernon, K., Chou, A., Aljada, M., Liu, J., & Motta, N. (2014). Plasmonic effect of gold nanoparticles in organic solar cells. *Solar Energy, 106*, 23-37.

Ohkita, H., Cook, S., Astuti, Y., Duffy, W., Tierney, S., Zhang, W., . . . Durrant, J. R. (2008). Charge Carrier Formation in Polythiophene/Fullerene Blend Films Studied by Transient Absorption Spectroscopy. *Journal of the American Chemical Society, 130*, 10.

Oldenburg, S. J., Jackson, J. B., Westcott, S. L., & Halas, N. J. (1999). Infrared extinction properties of gold nanoshells. *Applied Physics Letters, 75*(19), 2897-2899.

Oskooi, A., Roundy, D., Ibanescu, M., Bermel, P., Joannopoulos, J. D., & Johnson, S. (2010). Meep: A flexible free-software package for electromagnetic simulations by the FDTD method. *Computer Physics Communications, 181*(3), 687-702.

Otto, A. (1968). Excitation of nonradiative surface plasma waves in silver by the method of frustrated total reflection. *Z. Physik, 216*, 398.

Ozbay, E. (2006). Plasmonics: Merging Photonics and Electronics at Nanoscale Dimensions. *Science, 311*(5758), 189-193.

Palik, E. D. (2012). *Handbook of Optical Constants of Solids*: Elsevier Science.

Pillai, S., Catchpole, K. R., Trupke, T., & Green, M. A. (2007). Surface plasmon enhanced silicon solar cells. *Journal of Applied Physics, 101*(9), 093105.

Pillai, S., & Green, M. A. (2010). Plasmonics for photovoltaic applications. *Solar Energy Materials and Solar Cells, 94*(9), 1481-1486.

Qadir, R. W., Ahmad, Z., & Sulaiman, K. (2014). Effect of the shapes of nanostructures on the light absorption in organic thin films. *Journal of Modern Optics, 61*(8), 636-640.

Quidant, R., Zelenina, A. S., & Nieto-Vesperinas, M. (2007). Optical manipulation of plasmonic nanoparticles. *Applied Physics A, 89*(2), 233-239.

Rand, B. P., Peumans, P., & Forrest, S. R. (2004). Long-range absorption enhancement in organic tandem thin-film solar cells containing silver nanoclusters. *Journal of Applied Physics, 96*(12), 7519-7526.

Rand, B. P., & Richter, H. (2014). *Organic Solar Cells: Fundamentals, Devices, and Upscaling*: Pan Stanford.

Ritchie, R. H. (1957). Plasma Losses by Fast Electrons in Thin Films. *Physical Review, 106*(5), 874-881.

Rukshan, F., Semendy, F., & Wijewarnasuriya, P. (2012). Altering Plasmonic Nanoparticle Size Through Thermal Annealing for Improved Photovoltaic Devices. (ARL-TR-5895). Adelphi, MD: Army Research Laboratory.

Sabuktagin, M. S., Hamdan, K. S., Sulaiman, K., Zakaria, R., & Ahmad, H. (2014). Long Wavelength Plasmonic Absorption Enhancement in Silicon Using Optical Lithography Compatible Core-Shell-Type Nanowires. *International Journal of Photoenergy, 2014*, 6.

Saito, G. (2007). *Multifunctional conducting molecular materials* (Vol. 100): Royal Society of Chemistry.

Şener, M. K., Gül, A., & Koçak, M. B. (2008). Novel phthalocyanines with naphthalenic substituents. *Transition Metal Chemistry, 33*(7), 867-872.

Shen, L., Zhu, G., Guo, W., Tao, C., Zhang, X., Liu, C., . . . Zhong, Z. (2008). Performance improvement of TiO2/P3HT solar cells using CuPc as a sensitizer. *Applied Physics Letters, 92*(7), 073307-073301-073307-073303.

Sherry, L. J., Chang, S.-H., Schatz, G. C., Van Duyne, R. P., Wiley, B. J., & Xia, Y. (2005). Localized Surface Plasmon Resonance Spectroscopy of Single Silver Nanocubes. *Nano Letters, 5*(10), 2034-2038.

Sommerfeld, A. (1952). PART I - FUNDAMENTALS AND BASIC PRINCIPLES OF MAXWELL'S ELECTRODYNAMICS *Electrodynamics* (pp. 1-54): Academic Press.

Spinelli, P., & Polman, A. (2012). Prospects of near-field plasmonic absorption enhancement in semiconductor materials using embedded Ag nanoparticles. *Optics Express, 20*(S5), A641-A654.

Stratakis, E., & Kymakis, E. (2013). Nanoparticle-based plasmonic organic photovoltaic devices. *Materials Today, 16*(4), 133-146.

Sullivan, D. M. (2013). *Electromagnetic Simulation Using the FDTD Method*: Wiley.

Supangat, A., Kamarundzaman, A., Asmaliza Bakar, N., Sulaiman, K., & Zulfiqar, H. (2014). P3HT:VOPcPhO composite nanorods arrays fabricated via template–assisted method: Enhancement on the structural and optical properties. *Materials Letters, 118*, 103-106.

Taflove, A., & Hagness, S. (2005). *Computational Electrodynamics: The Finite-Difference Time-Domain Method, Third Edition*: Artech House.

Varotto, A., Nam, C.-Y., Radivojevic, I., Tomé, J., Cavaleiro, J. A. S., Black, C. T., & Drain, C. M. (2010). Phthalocyanine Blends Improve Bulk Heterojunction Solar Cells. *Journal of the American Chemical Society, 132*(8), 2552-2554.

Wu, J.-L., Chen, F.-C., Hsiao, Y.-S., Chien, F.-C., Chen, P., Kuo, C.-H., . . . Hsu, C.-S. (2011). Surface Plasmonic Effects of Metallic Nanoparticles on the Performance of Polymer Bulk Heterojunction Solar Cells. *ACS Nano, 5*(2), 959-967.

Yang, F., & Forrest, S. R. (2008). Photocurrent Generation in Nanostructured Organic Solar Cells. *ACS Nano, 2*(5), 1022-1032.

Ye, S., Hou, Y., Zhu, R., Gu, S., Wang, J., Zhang, Z., . . . Du, J. (2011). Synthesis and Photoluminescence Enhancement of Silver Nanoparticles Decorated Porous Anodic Alumina. *Journal of Materials Science & Technology, 27*(2), 165-169.

Zhang, F., Gadisa, A., Inganas, O., Svensson, M., & Andersson, M. (2004). Influence of buffer layers on the performance of polymer solar cells. *Applied Physics Letters, 84*(19), 3906-3908.

LIST OF PUBLICATIONS AND CONFERENCES

Research Articles

Hamdan, K. S., Abdullah, S. M., Sulaiman, K., & Zakaria, R. (2014). Effects of silver nanoparticles towards the efficiency of organic solar cells. *Applied Physics A, 115*(1), 63-68

Sabuktagin, M. S., Hamdan, K. S., Sulaiman, K., Zakaria, R., & Ahmad, H. (2014). Long Wavelength Plasmonic Absorption Enhancement in Silicon Using Optical Lithography Compatible Core-Shell-Type Nanowires. *International Journal of Photoenergy, 2014*, 6,249476

Zakaria, R., Hamdan, K. S., Che Noh, S. M., Supangat, A. & Sookhakian, M. (2015). Surface plasmon resonance and photoluminescence studies of Au and Ag micro-flowers. *Optical Material Express, 5*(5), 943-950.

Conferences Attended

The 8th Mathematics and Physical Sciences Graduate Congress (**8th MPSGC**), 8th – 10th ecember 2012, Chulalongkorn University, Bangkok, Thailand.

The 4th International Conference on Functional Materials & Devices 2013 (**ICFMD - 2013**), 8th – 11th April 2013, Rainbow Paradise Hotel, Penang, Malaysia

The 9th Mathematics and Physical Sciences Graduate Congress (**9th MPSGC**), 8th – 10th January 2014, University of Malaya, Kuala Lumpur, Malaysia.

Seoul International Conference on Engineering and Applied Science (**SICEAS**), 5th – 7th January 2016, Courtyard by Marriot Seoul Times Square, Seoul, South Korea.